IDŐJÁRÁS

QUARTERLY JOURNAL
OF THE HUNGARIAN METEOROLOGICAL SERVICE

CONTENTS

VOL. 127 * NO. 1 * JANUARY – MARCH 2023

* * * * *

IDŐJÁRÁS

Quarterly Journal of the Hungarian Meteorological Service

Editorial Office: Kitaibel P.u. 1, H-1024 Budapest, Hungary
P.O. Box 38, H-1525 Budapest, Hungary
E-mail: journal.idojaras@met.hu

Indexed and abstracted in Science Citation Index Expanded™ and Journal Citation Reports/Science Edition
Covered in the abstract and citation database SCOPUS®
Included in EBSCO's database

Subscription by mail:
IDŐJÁRÁS, P.O. Box 38, H-1525 Budapest, Hungary
E-mail: journal.idojaras@met.hu

DOI:10.28974/idojaras.2023.1.1

IDŐJÁRÁS

Quarterly Journal of the Hungarian Meteorological Service
Vol. 127, No. 1, January – March, 2023, pp. 1–22

Assessment of WRF planetary boundary layer schemes in the simulation of fog events over Hungary

Jeevan Kumar B * and **Gabriella Schmeller**

University of Pécs, Faculty of Science
Ifjúság str 6, H-7624 Pécs, Hungary.

**Corresponding author E–mail: jeevan@gamma.ttk.pte.hu*

(Manuscript received in final form April 19, 2022)

Abstract—Accurate depiction of meteorological conditions, especially within the planetary boundary layer (PBL), is essential for fog forecasting. This study examines the sensitivity of the performance of the Weather Research and Forecast (WRF) model to the use of four different PBL schemes [Yonsei University (YSU), asymmetric convective model version 2 (ACM2), quasinormal scale elimination (QNSE), and Mellor-Yamada-Nakanishi-Niino version 3.0 (MYNN3)]. For this case study we have taken the fog event occurred in November 23-24, 2020. Surface observed temperature and relative humidity, furthermore, sounding data are compared with the output of the 36 hours, high-resolution weather forecast. The horizontal extension of the simulated fog is compared with satellite observations. The visibility is calculated from the prognostic variables of drop number concentration and mixing ratio. The simulated visibility and fog duration are validated by the visibility and fog duration evaluated by ceilometer observations. Validation of thermodynamical values such as 2-m temperature and relative humidity reveals, that during most of the simulation time, the bias is significant between the simulated and observed data. Results show that the PBL parameterization scheme significantly impacts fog microphysics also. The QNSE scheme results in unrealistic early formation of the fog, and too large liquid water content. YSU and ACM2 simulated the duration of fog to be rather short comparing with the other two PBL schemes. The best fitting with observed data is found in the case of MYNN3 PBL schemes.

Key-words: fog, WRF, planetary boundary layer, Goddard Chemistry Aerosol Radiation and Transport (GOCART)

1. Introduction

Fog is a boundary layer weather phenomenon with tiny droplets of water or ice crystals formed near-surface in a diameter range of ~2–30 μm reducing the horizontal visibility in the atmosphere near the surface less than 1 km (*Gultepe et al*., 2007). Fog is one of the significant weather hazards that affects aviation, road transportation, economy, and public health worldwide. However, very few studies were carried out to understand the fog characteristics over Hungary. *Cséplő et al*., 2019 investigated fog climatology and long-term trends in Hungary.

Forecasting of fog remains a challenge because of diversity of processes including the drop formation on submicron size aerosol particles, turbulence, radiation, and soil effects. Although researchers carried out multiple field experiments and contributed progress in understanding fog processes, uncertainties remain in the physical mechanisms driving the fog variability. Noteworthy studies include campaigns in the Po Valley in Italy (*Fuzzi et al.,* 1998), Paris fog in France (*Haeffelin et al*., 2010), and winter fog experiments over New Delhi (*Ghude et al*., 2017).

However, numerical models were also used to study fog to fill the inconsistencies between observational challenges. Conventional empirical models/techniques are not uncommonly accurate in the case of fog forecasting, and mesoscale weather prediction models could not yet adequately be developed for predicting fog and visibility conditions near the surface. There are many models available to simulate the weather, such as the U.S. Rapid Update Cycle (RUC) model (*Benjamin et al*., 2004), the Weather Research and Forecasting (WRF) model (*Skamarock et al*., 2008), the Consortium for Small Scale Modeling (COSMO) (*Rockel et al*., 2008), the Japan Meteorological Agency Non-Hydrostatic Model (JMA-NHM) (*Saito et al.,* 2006), and the Canadian Mesoscale Compressible Community (MC2) model (*Benoit et al*., 1997). Among all models, WRF is widely used to forecast the weather and also for research purposes (e.g., *Geresdi et al*., 2020; *Horváth et al*., 2007; *Sarkadi et al*., 2016).

The WEF model has a broad spectrum of physical parameterizations representing the sub-scale cumulus formation, cloud microphysics, planetary boundary layer (PBL), atmospheric radiation, and land surface processes that account for the interaction between the atmosphere and the Earth's surface. The proposed parameterization options in WRF range from basic to more subtle and computationally costly systems that are revised permanently with newly updated/developed model versions. Depending on the model domain, spatial resolution, location, and application, researchers are published different simulation performances using various combinations of physical schemes to simulate atmospheric processes (e.g., *Lábó* and *Geresdi*, 2016; *Thériault et al*., 2015). A wide range of WRF communities from all over the world made several sensitivity tests to perform weather simulations according to their requirements

and areas of interest (*Chaouch et al.,* 2017; *Horváth et al*., 2009; *Pithani et al.,* 2019a, 2018a).

Microphysical processes play a controlling role in the evolution of fog. Cloud microphysics is affected by aerosol particles through initiation of the liquid drop and ice formation. Increase of water-soluble aerosol concentration generally leads to increase of droplet concentration impacting both the lifetime and the efficiency of the precipitation formation (*Twomey,* 1984). *Thompson* and *Eidhammer* (2014a) introduced a new updated WRF microphysics scheme which allowed us to consider the temporal and spatial variability of aerosol particles evaluated by the Goddard Chemistry Aerosol Radiation and Transport (GOCART) model (*Chin et al*., 2002; *Ginoux et al.,* 2001). The output of GOCART model includes mass mixing ratio of sulfates, sea salts, organic carbon, dust, and black carbon data.

The processes occur in the planetary boundary layer (hereafter PBL) significantly impacting the characteristics of the fog (e.g., duration, visibility). Our understanding about the PBL processes and their effect on the fog are still incomplete. In this study, sensitivity test has been performed to compare the results of using different PBL parameterization schemes.

2. Data and methods

2.1. Observations

For this modeling experiment we have taken the fog event occurred in the morning of November 24, 2020 as a case study. *Fig. 1* shows the EUMETSAT satellite image of fog covered large part of Hungary at 07:10 on November 24, 2020 local time. At this time, fog covered the eastern and northwestern parts of Hungary.

The time evolution of back scatter profiles observed by ceilometer over Pécs and Szeged are depicted in *Fig.* 2. *Fig.* 2 shows that while at Szeged fog existed during morning, and before noon fog lifted up due to solar radiation, at Pécs fog did not formed, only low level cloud was detected at late afternoon. The vertical extension of the fog changed between 80 and 100 m. Satellite image also shows the presence and absence of fog at the observational sites of Pécs and Szeged (*Fig. 1*).

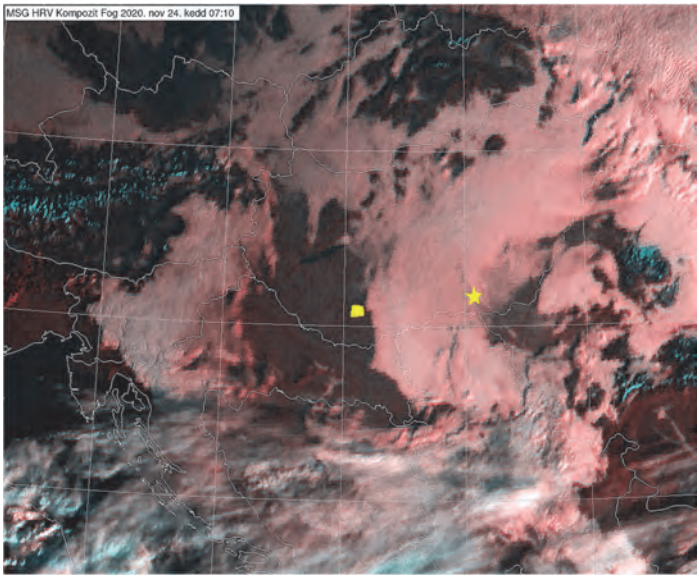

Fig. 1. Satellite image of fog at 07:10 CET (06:10 UTC) on Nov 24,2020. [Square and star symbols shows Pécs and Szeged meteorological stations, respectively.]

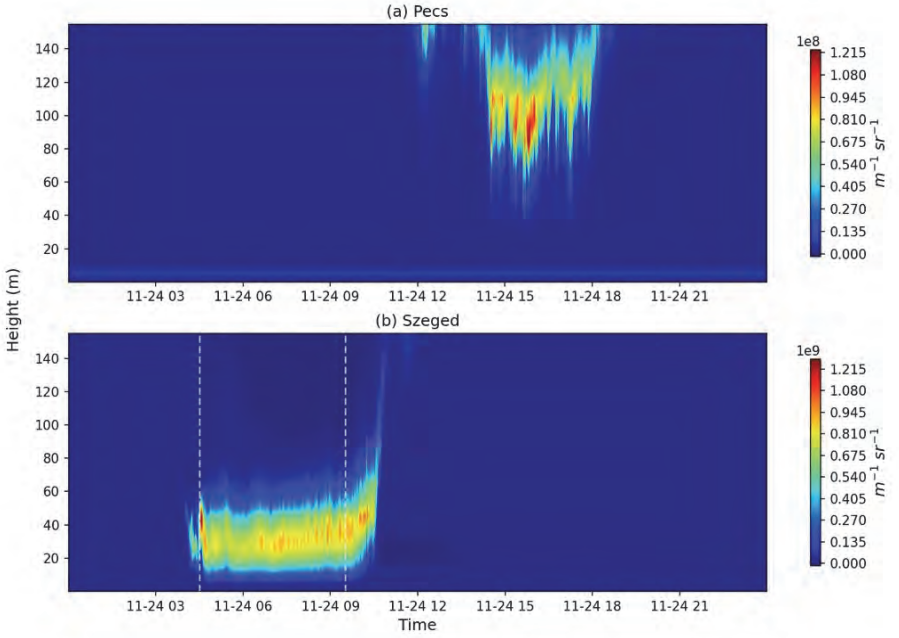

Fig. 2. Back scatter data from Pécs (a) and Szeged (b) on Nov 24, 2020. Time is depicted as month-day hour (in CET).

Black solid lines in *Fig. 3* denotes the visibility calculated from ceilometer backscattered data over Szeged. Colored lines depict the time evolution of simulated visibility (at the first model level) using different PBL schemes.

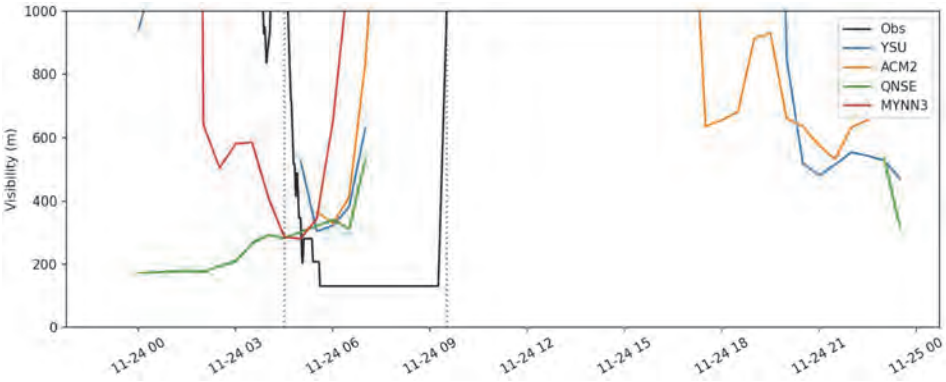

Fig. 3. Calculated visibility data from ceilometer backscattered data and model simulated visibility over Szeged. Note: data are plotted only at Szeged, because fog was not detected at Pécs. Time is depicted as month-day hour (in CET).

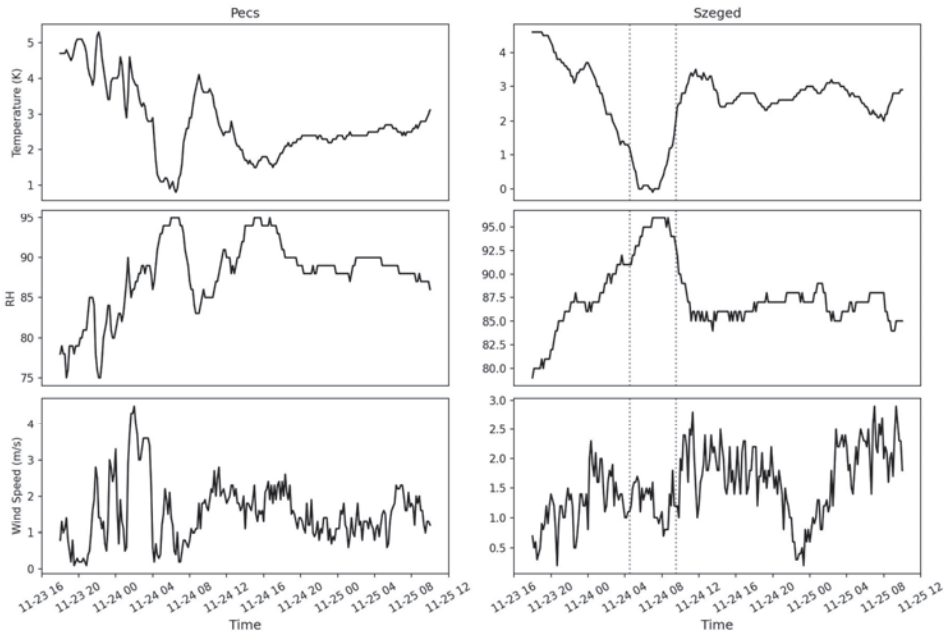

Fig. 4. Time evolution of the surface meteorological parameters (temperature and relative humidity 2 m above the surface, and wind speed at the first model level) over Pécs and Szeged. Vertical, dotted lines for Szeged column indicate the detected fog period. Time is depicted as month-day hour (in CET).

Fig. 4 shows the diurnal cycle of temperature, relative humidity and wind speed at Pécs and Szeged. Calm winds, decreasing temperature, and increasing relative humidity are showing favorable conditions for fog formation both at Pécs and Szeged. Due to measurement errors in the instruments, the relative humidity sensors measure up to 95%, and they usually do not reach 100% (*Gultepe*, 2019, 2007). However, fog was detected only over Szeged, where visibility decreased sharply early morning and became as low as 200 m at 04:30 UTC, indicating the formation of fog. The visibility increased sharply shortly at about 09:30 UTC in response to increasing temperature (*Fig. 3*).

2.2. Model description

Several sensitivity experiments have been accomplished to study how the accuracy of fog forecast depends on planetary boundary layer (PBL) schemes implemented in the WRF Advanced Research Core (ARW, V4.3). The horizontal extension of the model domain is 800 km × 740 km with horizontal spatial resolution of 2 km. The domain covers the whole territory of Hungary and some part of Hungary's neighbor countries Austria, Croatia, Bosnia, Serbia, Romania, Ukraine, and Slovakia. We use Lambert coordinate configuration with center at 47°N and 19°W to define the domain, and 61 vertical levels (18 levels below 1000 m and 8 levels below 100 m). The large vertical spatial resolution under 100 m allows to properly simulate the vertical structure of the fog and to resolve the inversion layer formed at the top of the fog.

Meteorological initial and boundary conditions are provided by reanalysis products of the European Centre for Medium-Range Weather Forecasting (ECMWF). ERA5 data are operational global analyses available on 0.25°×0.25° grids with 1 h temporal resolution. For the mesoscale simulations, the geographical data for the land-use and topography are obtained from the standard U.S. Geological Survey dataset (

Fig. 5). Initial conditions at 18:00 UTC on November 23, 2020 are selected for simulation of the fog.

The following parameterization schemes are set to simulate the different physical processes: (i) the rapid radiative transfer model (RRMTG) for both longwave radiation and shortwave radiation (*Iacono et al.*, 2008); (ii) the Thompson aerosol aware two-moment bulk scheme for microphysics (*Thompson* and *Eidhammer*, 2014b), (iii) Noah land surface scheme to simulate the impact of the soil and land use (*Chen* and *Dudhia*, 2001). The advantage of the Thompson scheme (*Thompson* and *Eidhammer* (2014b), compared with other bulk microphysics schemes, is that it able to take into consideration the spatial and temporal variability of the concentration of aerosol particles impacting both the drop and ice formation. This microphysics scheme allows us to evaluate not only the liquid water content (hereafter LWC), but the number concentration of liquid drops explicitly as well. The calculation of prognostic variable of number

concentration of liquid drops not only results in more reliable forecast for the fog formation, but also improve the accuracy of the evaluation of the visibility.

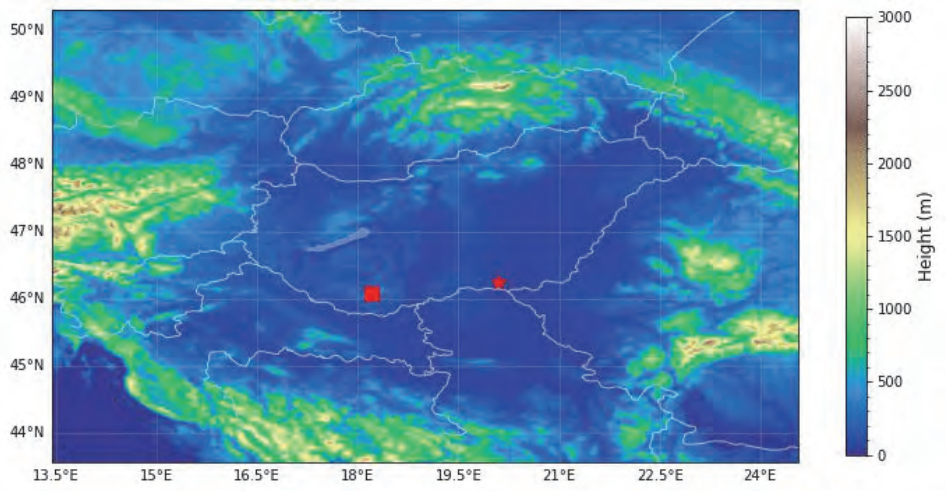

Fig. 5. Topography of WRF model domain with observational sites (square indicates Pécs and star indicates Szeged).

The PBL schemes and surface layer (SFC) formulations are set to be different in each experiment. PBL schemes parameterize turbulent vertical fluxes of heat, momentum, and components like moisture in the PBL. Because some of PBL schemes are suggested tightly coupled to particular surface layer schemes in WRF, it is not possible to have a common surface layer scheme for all experiments. In this case study, we utilized four PBL schemes, MYNN3.0 (*Nakanishi* and *Niino*, 2006), YSU (*Hong et al*., 2006), QNSE (*Sukoriansky et al*., 2005), and ACM2 (*Pleim*, 2007). The considered four PBL schemes and the coupled surface schemes are given in *Table 1*. *Cohen et al*., 2015 asserted that MYNN3.0 was reasonably good at the simulation of radiation fog development. The YSU scheme enhances mixing in the stable boundary layer by increasing the critical bulk Richardson number from 0 to 0.25 over land (*Chen et al*., 2020). The ACM2 scheme (*Pleim*, 2007) was elaborated to improve the shape of vertical profiles of temperature and dew point temperature near the surface. Both nonlocal schemes (YSU & ACM2) may result in strong vertical mixing, sometimes drier and warmer daytime PBLs. In the local scheme, the eddy diffusivity is determined independently at each point grid point, based on local vertical gradients of wind and potential temperature. The nonlocal scheme determines an eddy diffusivity profile based on a diagnosed boundary layer height and a turbulent vertical scale (*Mihailovic*, 2006).

Table 1. WRF model configuration and initial conditions

Test	Model specification
Initial boundary conditions	WRF-ECMWF
Model domain and resolution	400 × 370 grid points (2 km)
Land use and land category	USGS
Vertical resolution	61 vertical levels (18 levels below 1000 m and 8 levels below 100 m)
Radiation scheme (LW & SW)	RRTMG
Microphysics scheme	Aerosol-aware Thompson scheme
Land surface physics	Noah-mp land surface model
PBL & Surface layer physics	1. YSU and MM5 (Monin-Obukhov scheme) 2. Eddy-diffusivity mass flux (QNSE) and QNSE. 3. MYNN3 and MYNN 4. ACM2 and Pleim-Xiu
Spin up	4 hours (model initialized at 18:00 hour UTC)

Detailed descriptions of PBL schemes are given in the following sections.

2.2.1. YSU

The YSU scheme is a first-order nonlocal closure scheme (*Hong et al*., 2006). It utilizes a turbulence diffusion equation to derive prognostic flux variables within the mixed layer based on an eddy diffusivity coefficient and a counter gradient correction term. The counter gradient correction term accounts for the contribution of the large-scale eddies to the total flux. In the YSU scheme, entrainment is explicitly parameterized through an additional term in the turbulence diffusion equation. The scheme calculates the PBL height by considering bulk Richardson number (Ri_B) values calculated from the surface. Also, the YSU scheme is more effective at representing deep vertical mixing in buoyancy-driven PBLs with shallower mixing in strong-wind regimes (*Hong et al*., 2006). Also, it has been found that the depth of the PBL is overestimated for springtime deep convective environments, resulting in too much dry air near the surface and underestimation of convective available potential energy in the mixed layer.

2.2.2. ACM2

The asymmetrical convective model version 2 (ACM2) scheme is a first-order closure scheme (*Pleim*, 2007). It is a hybrid local - nonlocal closure scheme. In the ACM2 scheme, the upward fluxes from the surface interact with each layer to account for convective plumes emanating from the surface. On the other hand, the downward fluxes only interact between the adjacent layers. Eddy diffusion is treated locally for both upward and downward fluxes. The scheme utilizes only the local mixing for upward, and downward mixing for stable/neutral flow regimes. In ACM2, the calculation of the PBL height is based on the bulk Richardson number (Ri_B). It is determined as the height where the Ri_B calculated above the neutral buoyancy level is greater than a critical Ri_B value of 0.25. *Pleim* (2007a) indicated that the profile of potential temperature and velocity through the PBL are depicted with greater accuracy when both local and nonlocal viewpoints are considered regarding vertical mixing (ACM2); *Pleim* (2007) further validated the use of the ACM2 scheme owing to its support of PBL heights similar to those based on afternoon wind profiler data from radar. However, *Coniglio* (2012) reported that the scheme produces PBLs were too deep in the evening compared to sounding data.

2.2.3. QNSE

The quasi-normal scale elimination (QNSE) scheme is a 1.5-order local closure scheme (*Sukoriansky et al*., 2005). It is a spectral model designed for turbulent flows characterized by stable stratification. The scheme involves a quasi-Gaussian mapping of the velocity and temperature fields to account for wave phenomena in stable boundary layers. A stratification scale-dependent elimination algorithm explicitly accounts for the combined effect of turbulence and internal waves. As stratification increases, energy is accumulated in the horizontal flow components at the expense of the energy for the vertical flow components. The scheme calculates the PBL height as the height at which the TKE profile decreases to a value of 0.01 m^2 s^{-2}. The scheme provides realistic depiction of potential temperature profiles, PBL height, and kinematic profiles based on observational data and corresponding large eddy simulations (*Cohen et al*., 2015) for its designed environment (stable conditions). However, in the case of the less-stable PBL, QNSE depicts too cool, moist, and shallow PBL in the case of springtime convective environments.

2.2.4. MYNN

The Mellor-Yamada-Nakanishi-Niino Level 3 (MYNN) scheme is a second-order local closure scheme (*Nakanishi* and *Niino*, 2006). In the MYNN3 scheme, equations for stability and mixing length are based on the results of large eddy simulations rather than on observations. Compared with older versions (MJY,

MYNN2.5), MYNN3 more accurately portrays deeper mixed layers and reasonably depicts statically stable boundary layer simulations supporting radiation fog development (*Nakanishi* and *Niino*, 2006). However, just like the other local closure schemes, it still may not fully account for deeper vertical mixing associated with larger eddies and associated counter gradient flux correction terms (*Cohen et al*., 2015).

The above sections reveal the major advantages and disadvantages of four different PBL schemes. Further detailed information about all applied PBL schemes can be found in the following papers: *Chaouch et al.*, 2017; *Cohen et al.*, 2015; *García-Díez et al*., 2013; *Hu et al.*, 2010; *Pithani et al*., 2019a.

3. Results

3.1. Analysis of the model data

Model (1st level) corresponding grid point 2 m temperature (hereafter T2) is evaluated for comparison with observation data measured at Pécs and Szeged locations (*Fig. 6*).

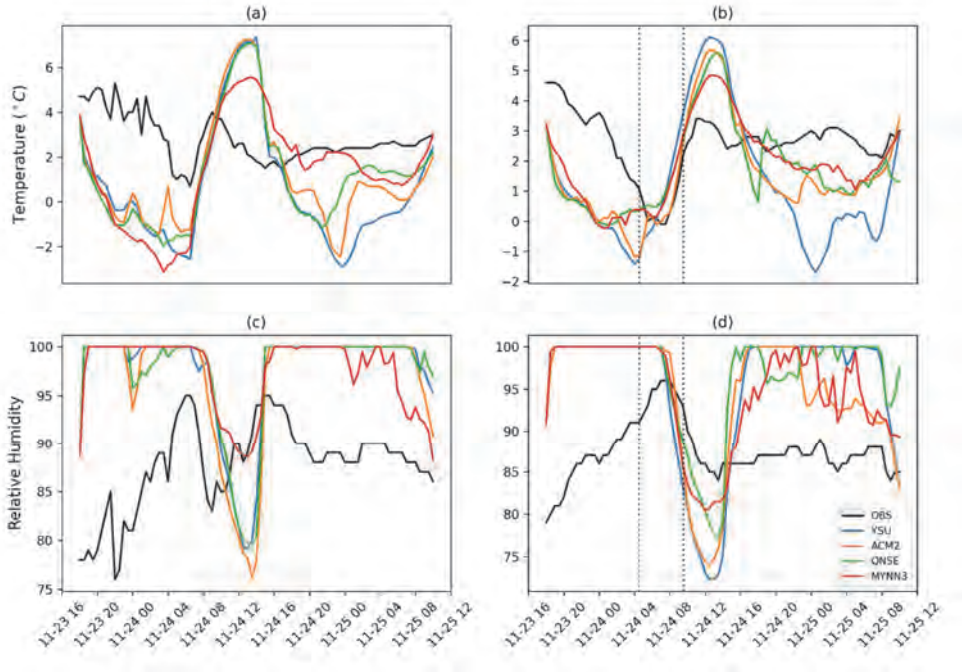

Fig. 6. Time evolution of observed and simulated 2 m temperature and relative humidity weather stations of Pécs and Szeged. Black lines denote the observed values, colored lines correspond to the different PBL schemes (see the legend in (d)). Time is depicted as month-day hour (in CET).

It was found, that the simulated T2 suffers from substantial warm and cold bias during most of the simulated time period (approximately 3–5 ºC; *Fig. 6*) independently of the applied PBL scheme. However, fog event was noticed in Szeged on November 24, 2020 between 04:30 – 09:30 UTC, and no fog event was noticed at the Pécs weather station (*Fig.* 2). Comparison of the observed and simulated time profiles of temperature (*Figs. 6a* and 6*c*) shows that the temperature was underestimated during middle nights by numerical simulation (independently of the applied PBL schemes), and it was overestimated during afternoon time at both Pécs and Szeged locations. However, all PBL schemes simulated well the change of the temperature during morning time, and the MYNN3 scheme was slightly better than others throughout the simulation period. While the calculated relative humidity was near to 100% during almost the whole simulated time period, the observed RH never reached this maximum value (note the observation error about RH). However, the decrease of simulated RH starts earlier, and it is steeper than the observed one.

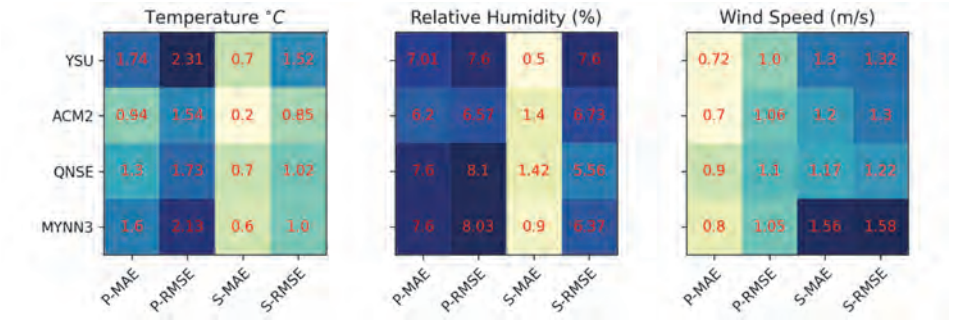

Fig. 7. Heat map of error statistics for the PBL sensitivity simulations over Pécs and Szeged for the observed fog period (see the vertical dashed line in *Fig. 6*). P-MAE indicates the mean absolute error over Pécs and P-RMSE indicates root mean square error over Pécs. S-MAE indicates the mean absolute error over Szeged and P-RMSE indicates root mean square error over Szeged.

Fig. 7 shows the heatmap of calculated error statistics for the PBL sensitivities for the simulation of the fog period at Szeged and Pécs to reveal the performance of the model with each PBL and to identify the better performing schemes. *Fig. 7* gives the mean absolute error (MAE) and root mean square error (RMSE) statistics for temperature, wind speed, and relative humidity at Pécs and Szeged. ACM2 PBL scheme produced comparatively better MAE and RMSE values for the temperature at both locations (Pécs: 0.94 and 1.54 °C, Szeged: 0.2 and 0.85 °C) during the fog period. YSU scheme shows the largest of temperature

bias, and it results in the largest mean absolute error and root mean square error. In the case of relative humidity, ACM2 gave better result only with MAE and RMSE over Pécs, but YSU scheme has low MAE and QNSE has low RMSE value over Szeged. For wind speed, ACM2 has low MAE, and MYNN3 has low RMSE values over Pécs, and QNSE has low MAE and RMSE values in Szeged. The best fitting between the observed and simulated temperature and relative humidity occurs in the case of MYNN3 scheme.

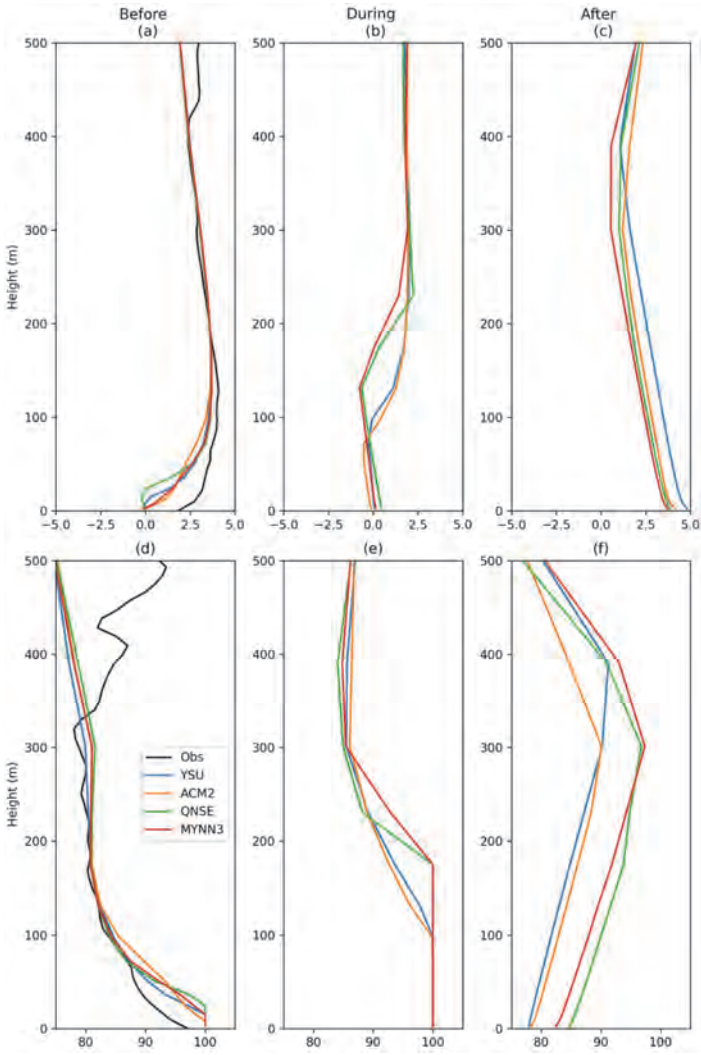

Fig. 8. Vertical profile of temperature and relative humidity before (a, d), during (b, e), and after (c, f) the over Szeged.

Fig. 8 shows the vertical profile of temperature and RH in three phases of the fog evolution such as before fog onset (November 24, 2020, 00:00 UTC), during the fog (November 24, 2020 06:00 UTC) and after the fog (November 24, 2020, 10:30 UTC) at a grid point near Szeged. In *Fig. 8a, 8d,* the calculated vertical profiles of temperature and RH are compared with sounding profiles. (The observed profiles are plotted only in *Fig. 8a*, and *8d*, because sounding data are available only at 00:00 UTC). The numerical simulation underestimates the temperature in the layer of 0 – ~200 m. While YSU and MYNN3 PBL schemes, similarly to the observed profile, result in strong inversion below 100 m from surface, ACM2 and QNSE PBL schemes perform inversion layer started above the surface. The RH is overestimated in each case in a very shallow layer of about 50 m. The observation error can be significant when the atmosphere is near the saturation.

The applied PBL parameterization technique significantly impacts the vertical profiles during and after the fog. The nonlocal schemes (YSU and ACM2) result in shallower fog layer than the local schemes (QNSE and MYNN3). The layer characterized by 100% RH and altitude of the inversion layer is deeper in the case of the local PBL schemes than in the case of the nonlocal schemes (*Fig. 8b* and *8e*). The altitude of the inversion layer should coincide approximately with the top of the fog. The plots about RH also support the above statements. During the fog event, the atmosphere is saturated near the surface, and the depth of the saturated layer correspond, to the altitude of inversion layer (*Fig. 8e* and *8b*). The difference between the local and nonlocal schemes are more conspicuous if the RH profiles are compared in *Fig. 8f.*

3.2. Liquid water content (LWC)

The processes occur in PBL affect not only the dynamics and thermodynamics of the atmosphere, but also impact the fog microphysics. The most important characteristic of the fog is the amount of the condensed vapor that is the liquid water content (hereafter LWC). In this section the results about the sensitivity of the amount of LWC on the applied PBL schemes are presented. The objective is to determine which PBL scheme is able to simulate more accurately the characteristics (e.g., duration, visibility) of the fog.

Fig. 9 and *Fig*. 10 show the PBL sensitivity results of simulated time series of the vertical profile of LWC at the grid points near the location of the observation at Pécs and Szeged. These plots clearly correspond to the back scatter data (*Fig.* 2). Over Pécs, both the observation and the numerical simulation exclude the fog formation during morning on November 24. At the location of Szeged, the WRF simulations with each PBL scheme produce fog during the early morning on November 24. The simulated onset time of the fog is not accurate comparing with the ceilometer data, and all the PBL schemes produced early fog onset at the first level of the model (*Fig. 3* and *Fig*. 10). YSU and ACM2 schemes

produced less amount of LWC at fog onset (04:30 UTC). QNSE and MYNN3 schemes produced significantly high amount of LWC at fog onset (04:30 UTC), and it is corresponding to low visibility (*Fig. 3*). However, numerical models forecast significantly earlier dissipation of the fog. The different PBL schemes result in fog with different lifetimes, LWCs, and thicknesses. YSU and ACM2 schemes simulate significantly smaller LWC compared to QNSE and MYNN3 schemes. The faster dissipation of the fog in the case of YSU and ACM2 schemes can be explained by the fact, that these schemes are characterized by producing warmer and drier daytime in the PBL (*Cohen et al.,* 2015). QNSE scheme seems to overestimate both the LWC and the duration of the fog, as it depicts too cool, moist shallow PBL for simulations *(Cohen et al.*, 2015; *Sukoriansky et al*., 2005). Our results support the results published by *Nakanishi* and *Niino* (2006), that MYNN3 PBL scheme reasonably depicts the formation of the statically stable boundary layer, which contributes to the reliable simulations of radiation fog. The LWC are integrated for the entire model domain (below 1000 m height) to analyze the impact of the different PBL schemes on the drop formation. *Fig. 11* shows the histograms about the frequency of the LWC for different ranges of mixing ratios at the simulation time of November 24, 2020, 06:00 UTC. The height of the columns means the integrated LWC over the domain at each range of the mixing ratio. The most evident characteristics of the histograms that the QNSE scheme produces significantly larger amount of LWC in the last three ranges than the three other PBL schemes, and the MYNN3 scheme results in more liquid drops at the smaller ranges and less liquid in the larger ranges.

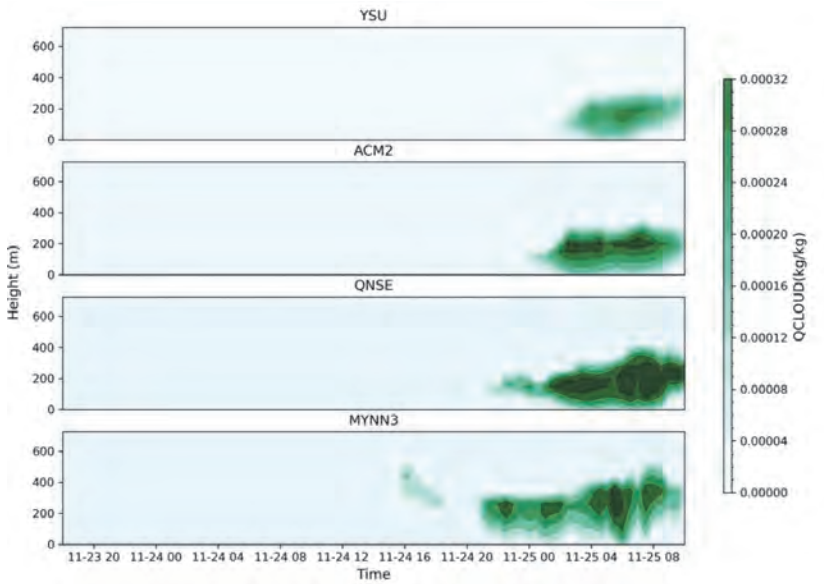

Fig. 9. Time series of the vertical profile of LWC over Pécs in case of the four different PBL schemes. Time is depicted as month-day hour (in CET).

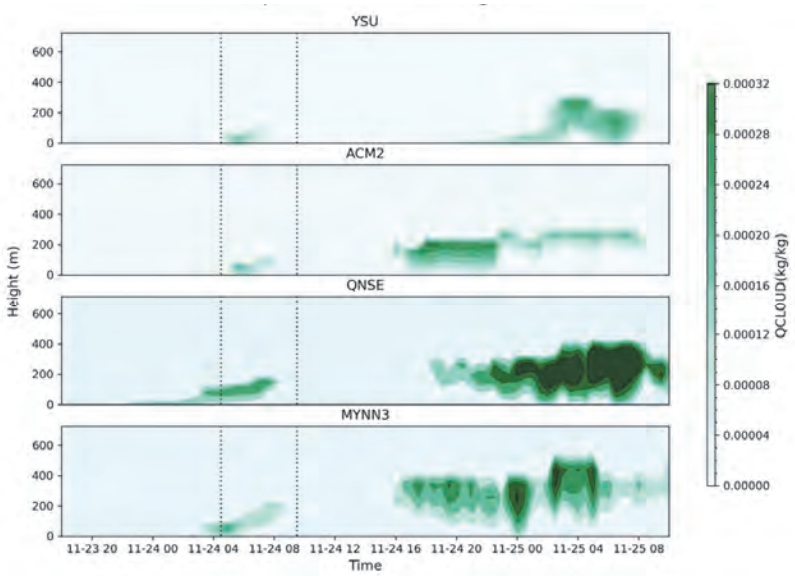

Fig. 10. Time series of the vertical profile of LWC over Szeged in the case of the four different PBL schemes. Time is depicted as month-day hour (in CET).

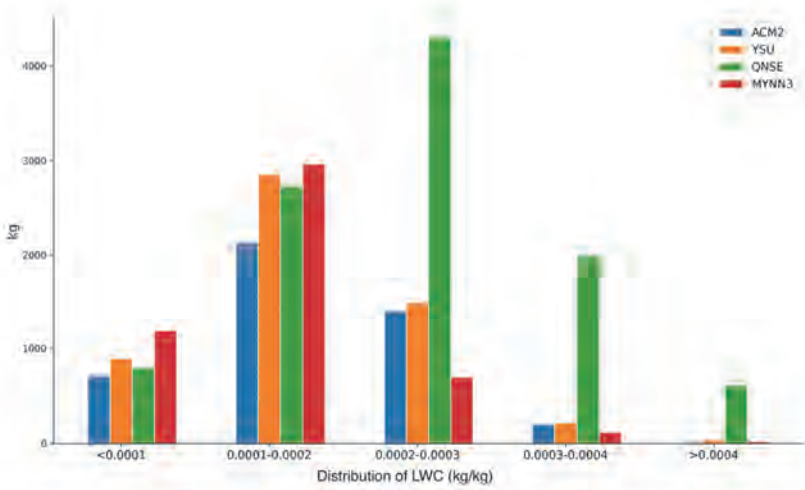

Fig. 11. Histograms of the domain integrated LWC at different ranges at the simulation time of November 24, 2020, 06:00 UTC (approximately at the middle of the fog period).

Fig12 shows the spatial distribution of LWC at the first level of the model in the case of the different PBL schemes at November 24, 2020, 06:00 UTC. All the schemes produced LWC over a relatively large area in the eastern and northwestern parts of Hungary. The numerical simulation using MYNN3 PBL scheme gives the best agreement with the satellite observation (*Fig. 1*). While QNSE scheme produces large values of LWC and overestimate the horizontal extension of the fog, the YSU and ACM2 schemes underestimate the horizontal extension of the fog near the southern border of Hungary.

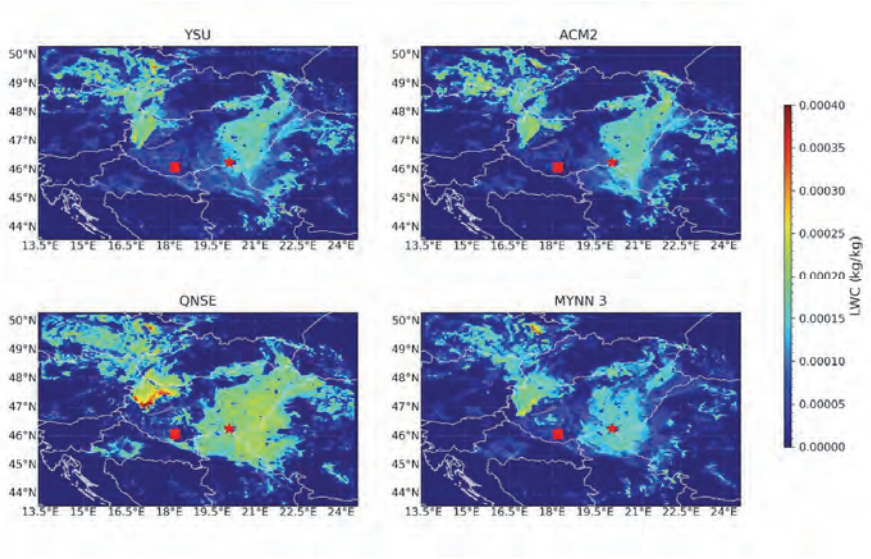

Fig. 12. Spatial distribution of LWC at November 24, 2020 06:00 UTC at the altitude of 6 m.

3.3. Visibility calculation

The forecast of the visibility is one of the largest challenges for meteorologists. As it was presented above, the LWC is impacted not only by the cloud microphysics, but the accurate simulation of PBL processes is also required. Even more, although the impact of the soil or that of the radiation has not been studied in this research, they also play important role in the fog evolution. Another issue is that the visibility can be evaluated accurately if the size distribution of the drops in the fog is available. Unfortunately, the implementation of a bin microphysical scheme in the operational weather forecast numerical model is not an option. So, a parameterized formula should be applied to estimate the visibility. Two-moment bulk microphysical schemes, which predict both the number concentration of liquid drops and LWC, allow a more sophisticated evaluation of

the visibility than the one-moment schemes (they forecast only the LWC). *Gultepe et al*. (2006) asserted that the evaluation of visibility without taking into consideration of the variability in drop concentration could cause 50% uncertainty in the estimation of the visibility. In this study we calculate visibility by substituting the forecasted LWC and drop concentration in the equation as follows (*Song et al*., 2019):

$$Vis = \frac{0.511}{\left(LWC \times N_d\right)^{0.52}}, \tag{1}$$

where N_d is the drop concentration. *Fig. 13* shows the calculated ground (first model) level spatial visibility at November 24, 2020, 06:00 UTC. It has to be noticed, that the spatial distribution is corresponded with the satellite image.

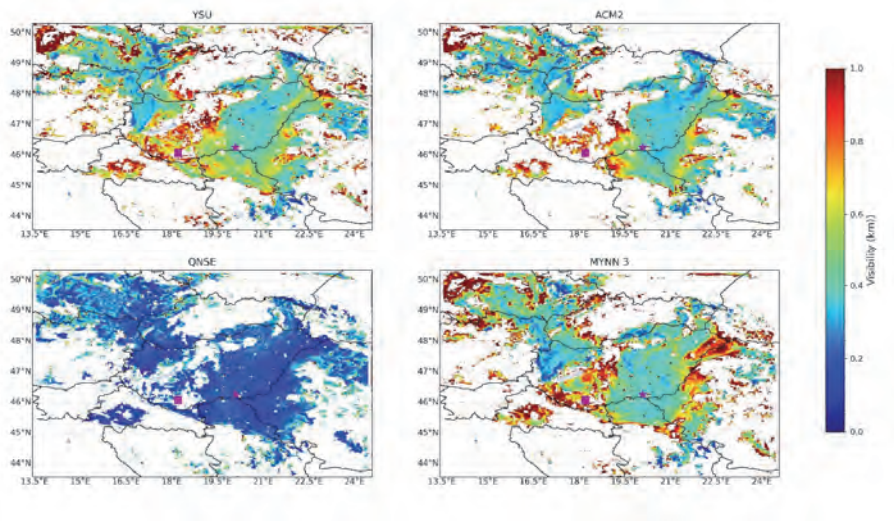

Fig. 13. Spatial distribution of visibility over 6 m height (first model level) at November 24, 2020. 06:00 UTC.

Fig. 3 shows the time evolution of the observed and simulated visibility. All PBL schemes results in early onset of fog (*Fig. 3*), even more, QNSE scheme produced visibility less than 200 m at model fog onset and started to increase the visibility at fog onset observed. Both nonlocal schemes (YSU and ACM2) produced visibility greater than 500 m at model fog onset which started to decrease significantly after fog onset observed. Among all PBL schemes MYNN3 results in significant decrease of visibility slightly before the observed fog onset

(04:30 UTC) and maintained low visibility until the hours of the fog, resulting in earlier dissipation comparing with other observations (*Fig. 3*).

4. Discussion and conclusion

The main aim of this study was to better understand the capability of the WRF model to simulate the fog lifecycle for an extremely fog event that occurred in the time period of 04:30 UTC - 09:30 UTC on November 24, 2020. Detailed PBL sensitivity experiments have been accomplished by using numerical mesoscale model (WRF) to understand the model ability for fog prediction. A novel microphysical module, the GOCART–Thompson scheme, was implemented into WRF-ARW to couple the GOCART aerosol model to the aerosol-aware Thompson–Eidhammer microphysics scheme (*Thompson* and *Eidhammer,* 2014). The results of four different PBL schemes have been compared. These schemes involve different parameterizations for the turbulence which contributes to the mixing of heat and moisture. The model data are compared with observational data such as surface temperature, backscatter data from ceilometer measured at two locations, Pécs and Szeged, furthermore, with radio sounding data at Szeged. In agreement with the observations the numerical models, independently off the applied PBL schemes, provide fog at Szeged, do not provide fog at Pécs. Strong impact of the boundary layer processes on fog microphysics is proved by comparing the LWC calculated by using different PBL schemes. Unfortunately, observation data on the LWC is not available for this fog event. So, comparison of the satellite observations and the visibility data (it depends on both the drop concentration and LWC) with the model results, allows us to validate the simulated values. The QNSE results in unrealistic such as early fog formation, high amount of LWC and underestimated visibility at fog onset. The numerical models are not able to forecast the duration (too early onset and early dissipation) of the fog, independently which PBL schemes are used (*Fig. 4g*). *Fig. 4g* shows that all the PBL schemes are simulated early onset fog over Szeged, and indicates that no particular scheme is suitable fog forecasting. Based on our simulations, previous publications (*Pithani et al*., 2019b, 2018b; *Smith et al.,* 2021) and the calculated characteristics, the MYNN3 scheme is suggested to use for the numerical forecast of the fog.

Thermodynamics and dynamics occur in PBL play fundamental role in fog formation. In this research, a sensitivity test was accomplished to study how the parameterization of PBL processes impact the accuracy of fog forecast.

The conclusions of the PBL sensitivity experiment are as follows:

- The parameterization of the PBL schemes significantly impacts the fog microphysics, especially the amount of LWC. While the QNSE scheme results in unrealistic early formation of the fog (and too large LWC), the

duration of the fog is rather short if the nonlocal schemes (YSU and ACM2) are applied. Although even the MYNN3 scheme results in too early dissipation of the fog, the results suggest that the MYNN3 scheme is well suitable for fog prediction over Hungary.

- Unfortunately, all the simulation results (independently of the applied PBL scheme) show, that the dissipation of the fog starts too early (*Pithani et al*., 2019c, 2018b). The reason of this is not known. Because not only PBL processes, but the interaction between the atmosphere and the soil, and the effect of the radiation can be also decisive, further research is required to solve this problem.

References

Benjamin, S.G., Dévényi, D., Weygandt, S.S., Brundage, K.J., Brown, J.M., Grell, J.A., Kim, D., Schwartz, B.E., Smirnova, T.G., Smith, T.L., and *Manikin, G.S.,* 2004: An hourly assimilation/forecast cycle: the RUC model. *Mon. Weather Rev. 132*, 495–518. https://doi.org/10.1175/1520-0493(2004)132<0495:AHACTR>2.0.CO;2

Benoit, R., Desgagné, M., Pellerin, P., Pellerin, S., Chartier, Y., and *Desjardins, S.,* 1997: The Canadian MC2: A semi-Lagrangian, semi-implicit wideband atmospheric model suited for finescale process studies and simulation. *Mon. Weather Rev. 125*, 2382–2415. https://doi.org/10.1175/1520-0493(1997)125<2382:TCMASL>2.0.CO;2

Chaouch, N., Temimi, M., Weston, M., and *Ghedira, H.,* 2017: Sensitivity of the meteorological model WRF-ARW to planetary boundary layer schemes during fog conditions in a coastal arid region. *Atmos. Res. 187*, 106–127. https://doi.org/10.1016/j.atmosres.2016.12.009

Chen, C., Zhang, M., Perrie, W., Chang, R., Chen, X., Duplessis, P., and *Wheeler, M.,* 2020: Boundary Layer Parameterizations to Simulate Fog Over Atlantic Canada Waters. *Earth Space Sci. 7*. e2019EA000703. https://doi.org/10.1029/2019EA000703

Chen, F. and *Dudhia, J.,* 2001: Coupling an advanced land surface–hydrology model with the Penn State–NCAR MM5 modeling system. Part I: Model implementation and sensitivity. *Mon. Weather Rev. 129*, 569–585. https://doi.org/10.1175/1520-0493(2001)129<0569:CAALSH>2.0.CO;2

Chin, M., Ginoux, P., Kinne, S., Torres, O., Holben, B.N., Duncan, B.N., Martin, R. v., Logan, J.A., Higurashi, A., and *Nakajima, T.,* 2002: Tropospheric aerosol optical thickness from the GOCART model and comparisons with satellite and sun photometer measurements. *J. Atmos. Sci. 59*, 461–483. https://doi.org/10.1175/1520-0469(2002)059<0461:TAOTFT>2.0.CO;2

Cohen, A.E., Cavallo, S.M., Coniglio, M.C., and *Brooks, H.E.,* 2015: A review of planetary boundary layer parameterization schemes and their sensitivity in simulating southeastern U.S. cold season severe weather environments. *Weather Forecast. 30*, 591–612. https://doi.org/10.1175/WAF-D-14-00105.1

Coniglio, M.C., 2012: Verification of RUC 0-1-h forecasts and SPC mesoscale analyses using VORTEX2 soundings. *Weather Forecast. 27*, 667–683. https://doi.org/10.1175/WAF-D-11-00096.1

Cséplő, A., Sarkadi, N., Horváth, Á., Schmeller, G., and *Lemler, T.*, 2019. Fog climatology in Hungary. *Idájárás 123*, 241–264. https://doi.org/10.28974/idojaras.2019.2.7

Fuzzi, S., Laj, P., Ricci, L., Orsi, G., Heintzenberg, J., Wendisch, M., Yuskiewicz, B., Mertes, S., Orsini, D., Schwanz, M., Wiedensohler, A., Stratmann, F., Berg, O.H., Swietlicki, E., Frank, G., Martinsson, B.G., Günther, A., Dierssen, J.P., Schell, D., Jaeschke, W., Berner, A., Dusek, U., Galambos, Z., Kruisz, C., Mesfin, N.S., Wobrock, W., Arends, B., Brink, and *H. ten,* 1998: Overview of the Po valley fog experiment 1994 (CHEMDROP). *Contr. Atmos. Phys. 71,* 3–19.

García-Díez, M., Fernández, J., Fita, L., and *Yagüe, C.*, 2013: Seasonal dependence of WRF model biases and sensitivity to PBL schemes over Europe. *Quart. J. Roy. Meteorol. Soc. 139*, 501–514. https://doi.org/10.1002/qj.1976

Geresd, I., Xue, L., Sarkadi, N., and Rasmussen, R., 2020: Evaluation of orographic cloud seeding using a bin microphysics scheme: Three-dimensional simulation of real cases. *J. Appl. Meteorol. Climatol. 59*, 1537–1555. https://doi.org/10.1175/JAMC-D-19-0278.1

Ghude, S.D., Bhat, G.S., Prabhakaran, T., Jenamani, R.K., Chate, D.M., Safai, P.D., Karipot, A.K., Konwar, M., Pithani, P., Sinha, V., Rao, P.S.P., Dixit, S.A., Tiwari, S., Todekar, K., Varpe, S., Srivastava, A.K., Bisht, D.S., Murugavel, P., Ali, K., Mina, U., Dharua, M., Jaya Rao, Y., Padmakumari, B., Hazra, A., Nigam, N., Shende, U., Lal, D.M., Chandra, B.P., Mishra, A.K., Kumar, A., Hakkim, H., Pawar, H., Acharja, P., Kulkarni, R., Subharthi, C., Balaji, B., Varghese, M., Bera, S., and *Rajeevan, M.,* 2017: Winter fog experiment over the Indo-Gangetic plains of India. *Curr. Sci. 112*, 767–784. https://doi.org/10.18520/cs/v112/i04/767-784

Ginoux, P., Chin, M., Tegen, I., Goddard, T., In-, G., 2001. model Brent Holben •' Oleg Dubovik •,•' and Shian-Jiann Lin e CART) model . In this model all topographic from the Goddard Earth Observing System Data Assimilation System (GEOS emission is estimated to be between. 2-Journal of Geophysical Research 106, 20255–20273.

Gultepe, I., 2019: Low-Level Ice Clouds-Ice Fog. Encylopedia of Water: Science, Technology, and Society 1–19. https://doi.org/10.1002/9781119300762.wsts0140

Gultepe, I., 2007: Fog and Boundary Layer Clouds: Fog Visibility and Forecasting, Fog and Boundary Layer Clouds: Fog Visibil. Forecast. https://doi.org/10.1007/978-3-7643-8419-7

Gultepe, I., Müller, M.D., and *Boybeyi, Z.*, 2006: A new visibility parameterization for warm-fog applications in numerical weather prediction models. *J. Appl. Meteorol. Climatol. 45*, 1469–1480. https://doi.org/10.1175/JAM2423.1

Gultepe, I., Tardif, R., Michaelides, S.C., Cermak, J., Bott, A., Bendix, J., Müller, M.D., Pagowski, M., Hansen, B., Ellrod, G., Jacobs, W., Toth, G., and *Cober, S.G.*, 2007: Fog research: A review of past achievements and future perspectives. *Pure Appl. Geophys. 164*, 1121–1159. https://doi.org/10.1007/s00024-007-0211-x

Haeffelin, M., Bergot, T., Elias, T., Tardif, R., Carrer, D., Chazette, P., Colomb, M., Drobinski, P., Dupont, E., Dupont, J.C., Gomes, L., Musson-Genon, L., Pietras, C., Plana-Fattori, A., Protat, A., Rangognio, J., Raut, J.C., Rémy, S., Richard, D., Sciare, J., and *Zhang, X.*, 2010: PARISFOG: Shedding new light on fog physical processes. *Bull. Amer. Meteorol. Soc. 91*, 767–783. https://doi.org/10.1175/2009BAMS2671.1

Hong, S.Y., Noh, Y., and *Dudhia, J.,* 2006: A new vertical diffusion package with an explicit treatment of entrainment processes. *Mon. Weather Rev. 134*, 2318–2341. https://doi.org/10.1175/MWR3199.1

Horváth, Á., Geresdi, I., Németh, P., Csirmaz, K., and *Dombai, F.*, 2009: Numerical modeling of severe convective storms occurring in the Carpathian Basin. *Atmos. Res. 93*, 221–237. https://doi.org/10.1016/j.atmosres.2008.10.019

Horváth Á., Geresdi I., Németh P., and *Dombai F.*, 2007: The Constitution Day storm in Budapest: Case study of the August 20, 2006 severe storm. *Időjárás 111*, 41–63.

Hu, X.M., Nielsen-Gammon, J.W., and *Zhang, F.*, 2010. Evaluation of three planetary boundary layer schemes in the WRF model. *J. Appl. Meteorol. Climatol. 49*, 1831–1844. https://doi.org/10.1175/2010JAMC2432.1

Iacono, M.J., Delamere, J.S., Mlawer, E.J., Shephard, M.W., Clough, S.A., and *Collins, W.D.*, 2008: Radiative forcing by long-lived greenhouse gases: Calculations with the AER radiative transfer models. *J. Geophys Res: Atmos 113*. D13103. https://doi.org/10.1029/2008JD009944

Lábó, E. and *Geresdi, I.,* 2016: Study of longwave radiative transfer in stratocumulus clouds by using bin optical properties and bin microphysics scheme. *Atmos. Res. 167*, 61–76. https://doi.org/10.1016/j.atmosres.2015.07.016

Mihailovic, D.T., 2006: Impact of local and non-local eddy-diffusivity schemes on calculating the concentration of pollutants in environmental models. Proceedings of the iEMSs 3rd Biennial Meeting, "Summit on Environmental Modelling and Software".

Nakanishi, M. and *Niino, H.*, 2006: An improved Mellor-Yamada Level-3 model: Its numerical stability and application to a regional prediction of advection fog. *Bound.-Lay. Meteorol. 119*, 397–407. https://doi.org/10.1007/s10546-005-9030-8

Pithani, P., Ghude, S.D., Chennu, V.N., Kulkarni, R.G., Steeneveld, G.J., Sharma, A., Prabhakaran, T., Chate, D.M., Gultepe, I., Jenamani, R.K., and *Madhavan, R.*, 2019a: WRF Model Prediction of a Dense Fog Event Occurred During the Winter Fog Experiment (WIFEX). *Pure Appl. Geophys. 176*, 1827–1846. https://doi.org/10.1007/s00024-018-2053-0

Pithani, P., Ghude, S.D., Chennu, V.N., Kulkarni, R.G., Steeneveld, G.J., Sharma, A., Prabhakaran, T., Chate, D.M., Gultepe, I., Jenamani, R.K., and *Madhavan, R.*, 2019b: WRF Model Prediction of a Dense Fog Event Occurred During the Winter Fog Experiment (WIFEX). *Pure Appl. Geophys. 176*, 1827–1846. https://doi.org/10.1007/s00024-018-2053-0

Pithani, P., Ghude, S.D., Chennu, V.N., Kulkarni, R.G., Steeneveld, G.J., Sharma, A., Prabhakaran, T., Chate, D.M., Gultepe, I., Jenamani, R.K., and *Madhavan, R.*, 2019c: WRF Model Prediction of a Dense Fog Event Occurred During the Winter Fog Experiment (WIFEX). *Pure Appl. Geophys. 176*, 1827–1846. https://doi.org/10.1007/s00024-018-2053-0

Pithani, P., Ghude, S.D., Prabhakaran, T., Karipot, A., Hazra, A., Kulkarni, R., Chowdhuri, S., Resmi, E.A., Konwar, M., Murugavel, P., Safai, P.D., Chate, D.M., Tiwari, Y., Jenamani, R.K., and *Rajeevan, M.*, 2018a. WRF model sensitivity to choice of PBL and microphysics parameterization for an advection fog event at Barkachha, rural site in the Indo-Gangetic basin, India. *Theor. Appl Climatol. 136*, 1199–1113. https://doi.org/10.1007/s00704-018-2530-5

Pithani, P., Ghude, S.D., Prabhakaran, T., Karipot, A., Hazra, A., Kulkarni, R., Chowdhuri, S., Resmi, E.A., Konwar, M., Murugavel, P., Safai, P.D., Chate, D.M., Tiwari, Y., Jenamani, R.K., and *Rajeevan, M.*, 2018b. WRF model sensitivity to choice of PBL and microphysics parameterization for an advection fog event at Barkachha, rural site in the Indo-Gangetic basin, India. Theoretical and Applied Climatology 1–15. https://doi.org/10.1007/s00704-018-2530-5

Pleim, J.E., 2007: A combined local and nonlocal closure model for the atmospheric boundary layer. Part I: Model description and testing. *J. Appl. Meteorol. Climatol. 46*, 1383–1395. https://doi.org/10.1175/JAM2539.1

Pleim, J.E, 2007: A combined local and nonlocal closure model for the atmospheric boundary layer. Part II: Application and evaluation in a mesoscale meteorological model. *J. Appl. Meteorol. Climatol. 46*, 1396–1409. https://doi.org/10.1175/JAM2534.1

Rockel, B., Will, A., and *Hense, A.*, 2008: The regional climate model COSMO-CLM (CCLM). *Meteorol. Zeit. 17*, 347–348. https://doi.org/10.1127/0941-2948/2008/0309

Saito, K., Fujita, T., Yamada, Y., Ishida, J.I., Kumagai, Y., Aranami, K., Ohmori, S., Nagasawa, R., Kumagai, S., Muroi, C., Kato, T., Eito, H., and *Yamazaki, Y.*, 2006. The operational JMA nonhydrostatic mesoscale model. *Mon. Weather Rev. 134*, 1266–1298. https://doi.org/10.1175/MWR3120.1

Sarkadi, N., Geresdi, I., and *Thompson, G.*, 2016. Numerical simulation of precipitation formation in the case orographically induced convective cloud: Comparison of the results of bin and bulk microphysical schemes. *Atmos. Res. 180*, 241–261. https://doi.org/10.1016/j.atmosres.2016.04.010

Skamarock, W.C., Klemp, J.B., Dudhia, J.B., Gill, D.O., Barker, D.M., Duda, M.G., Huang, X.-Y., Wang, W., and *Powers, J.G.*, 2008: A description of the Advanced Research WRF Version 3, NCAR Technical Note TN-475+STR. Technical Report 113.

Smith, D.K.E., Renfrew, I.A., Dorling, S.R., Price, J.D., and *Boutle, I.A.*, 2021: Sub-km scale numerical weather prediction model simulations of radiation fog. *Quart. J. Roy. Meteorol. Soc. 147*, 746–763. https://doi.org/10.1002/qj.3943

Song, J.I., Yum, S.S., Gultepe, I., Chang, K.H., and *Kim, B.G.*, 2019: Development of a new visibility parameterization based on the measurement of fog microphysics at a mountain site in Korea. *Atmos. Res. 229*, 115–126. https://doi.org/10.1016/j.atmosres.2019.06.011

Sukoriansky, S., Galperin, B., and *Perov, V.*, 2005: Application of a new spectral theory of stably stratified turbulence to the atmospheric boundary layer over sea ice. *Bound.-Lay. Meteorol. 117*, 231–257. https://doi.org/10.1007/s10546-004-6848-4

Thériault, J.M., Milbrandt, J.A., Doyle, J., Minder, J.R., Thompson, G., Sarkadi, N., and *Geresdi, I.,* 2015. Impact of melting snow on the valley flow field and precipitation phase transition. *Atmos. Res. 156*, 111–124. https://doi.org/10.1016/j.atmosres.2014.12.006

Thompson, G. and *Eidhammer, T.*, 2014a: A Study of Aerosol Impacts on Clouds and Precipitation Development in a Large Winter Cyclone. *J. Atmos. Sci. 71*, 3636–3658. https://doi.org/10.1175/JAS-D-13-0305.1

Thompson, G. and *Eidhammer, T.*, 2014b: A study of aerosol impacts on clouds and precipitation development in a large winter cyclone. *J. Atmos. Sci. 71*, 3636–3658. https://doi.org/10.1175/JAS-D-13-0305.1

Twomey, S., 1984: Pollution and the Planetary Albedo. *Atmos. Environ. 41*, 120–125. https://doi.org/10.1016/j.atmosenv.2007.10.062

DOI:10.28974/idojaras.2023.1.2

IDŐJÁRÁS

Quarterly Journal of the Hungarian Meteorological Service
Vol. 127, No. 1, January – March, 2023, pp. 23 –42

Southern Hemisphere temperature trend in association with greenhouse gases, El Niño Southern Oscillation, and Antarctic Oscillation

Dragan Burić[1,*] and **Ivana Penjišević** [2]

[1]*Department of Geography, Faculty of Philosophy*
University of Montenegro
Danila Bojovica bb, 81400 Niksic, Montenegro

[2]*Department of Geography*
Faculty of Sciences and Mathematics
University of Priština in Kosovska Mitrovica
Lole Ribara 29, 38220 Kosovska Mitrovica, Serbia

**Corresponding author E–mail: dragan.buric@meteo.co.me*

(Manuscript received in final form March 31, 2022)

Abstract— In this study, the trend of mean seasonal and annual temperatures of the Southern Hemisphere was calculated based on the HadCRUT5 and NASA-GISS data networks, for the period 1901–2021 and 1951–2021. In order to determine the possible effects on temperature, man, or nature, the relationship with CO_2 concentration, GHG (greenhouse gases) radiation exposure, and teleconnections ENSO (El Niño Southern Oscillation) and AAO (Antarctic Oscillation) was examined. The obtained results indicate that there is a significant increasing trend of seasonal and annual temperatures in the Southern Hemisphere, which intensified in the period between 1951 and 2021 (from 0.11 to 0.12 °C per decade). According to climate models, one of the indicators of the dominance of the anthropogenic greenhouse effect is the polar amplification (more intense temperature rise going from the equator to the poles). However, polar amplification was not recorded in the Southern Hemisphere, due to the fact that there was the smallest increase in temperature in the belt between 44°S–64°S. Moreover, in the mentioned zone, the positive trend was smaller in the period between 1951 and 2021 than in the period between 1901 and 2021, which was not to be expected. Nevertheless, the Southern Hemisphere temperature showed a statistically significantly strong correlation with the concentration of CO_2 observed at the Mauna Loa station. It was also found that there is a significant relationship between the energy impact of greenhouse gases and the Southern Hemisphere temperature, which is logical, because with the growth of GHG, positive radiative forcing increases. When it comes to the impact of telecommunications, both considered teleconnections (ENSO and AAO) have an impact on changes in the temperature of the Southern Hemisphere.

Key-words: temperature trend, Southern Hemisphere, GHG, radiative forcing, ENSO, AAO

1. Introduction

Compared to previous announcements of the Intergovernmental Panel on Climate Change (IPCC), the Sixth Assessment Report with a high degree of certainty confirms the dominance of the anthropogenic factor on the climate. The report emphasizes that people are certainly causing global warming. In other words, human impact is primarily related to the excessive combustion of fossil fuels, which increases the concentration of greenhouse gases, primarily carbon dioxide (CO_2), in the atmosphere. The Paris Agreement, adopted in 2015, aimed to limit global warming to below 2 degrees, i.e., to increase the global average temperature by 1.5 °C by the end of this century compared to the pre–industrial level. If the global temperature rises by 2 degrees or more compared to the pre–industrial period, irreversible and possible large negative changes in natural and human systems can be expected according to the models (IPCC, 2021).

However, the aforementioned IPCC Report says that the increase in global temperature of 1.5 °C will be exceeded in the next 20 years (until 2040), because the growth of atmospheric CO_2 concentration has not stopped. According to official data provided by the NOAA, the average annual value of CO_2, obtained from measurements at the Mauna Loa Observatory (Hawaii), for 2021 was 416.45 ppm. Despite the decline in human activity over the past two years due to the COVID–19 pandemic, global temperature and CO_2 concentrations continued to rise (*Fig. 1*). Since the beginning of the Industrial Revolution (1750s), the concentration of CO_2 (47%) and methane (CH_4, 156%) has been exceeded by far, and the increase in nitrogen suboxide (N_2O, 23%) is similar to the increase which occurred between the glacial and interglacial periods, in the last 800,000 years (very high increase). The IPCC Report further points out that of the total anthropogenic CO_2 emissions, 91% originate from the combustion of fossil fuels, and 9% arise as a result of excessive land use. Of the total amount of CO_2 emitted, about 56% is absorbed by the oceans and land (mainly vegetation), and the rest (about 46%) accumulates in the atmosphere. Individually, vegetation absorbs slightly more CO_2 (30%) than the oceans (26%). Ocean acidification is very likely to lead to the extinction of many marine life. Most of the heat energy from the atmosphere is absorbed by the oceans – it is estimated that 80–90% of the heat of the climate system is absorbed by the oceans. Thus, study shows an increase in the average temperature of the World Sea to a depth of 3000 m, and that up to a depth of 100 m, the water temperature has risen by 0.33 °C since 1969 (IPCC, 2021).

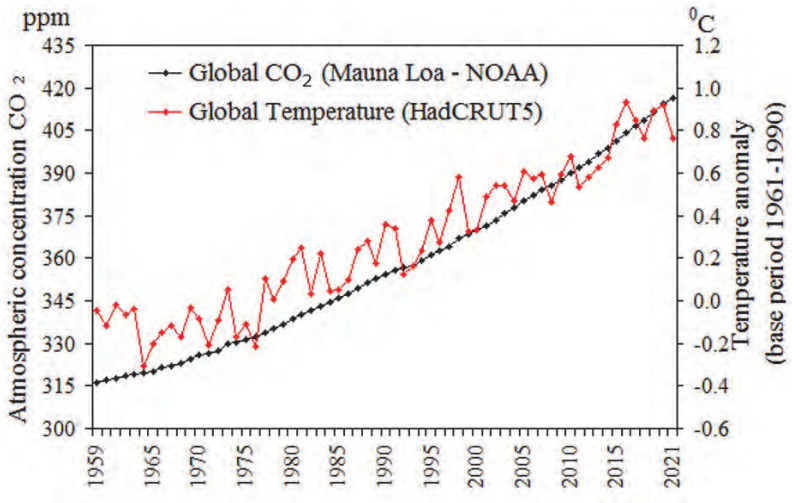

Fig. 1. Average values of global temperature and atmospheric concentration of carbon dioxide in the period from 1959 to 2021.

Recently, *Morice et al.* (2021) and *Osborn et al.* (2021) updated the global data of the HadCRUT network (Hadley Center and the Climatic Research Unit at the University of East Anglia). Based on the mentioned data set, the new version of HadCRUT5, it has been concluded that 2016 was the warmest year on our planet since the beginning of the instrumental period (since 1880), with an average deviation of 0.93 °C. During 2015 and 2016, especially in the winter, the strongest El Niño since 1870 was recorded, and this certainly had an impact on global temperature. The year 2020 (+0.92 °C) was the second warmest, while 2021 was the same as 2018, so they share the 6th and 7th places on the list of the warmest years, with a deviation of 0.76 °C. On the other hand, the *IPCC* (2021) points out that 2020 was the warmest year in the world and in Europe. In 2020, the global temperature was 1.1 °C higher than in the pre–industrial period. When it comes to changes in precipitation, the IPCC points out that the global amount of precipitation has probably increased since the 1950s, and that the increasing trend has been more intense since the 1980s. In any case, the IPCC believes that the human factor "extremely likely" contributed to global warming and changes in rainfall, and that modern climate change has led to more frequent and intense extreme events: heat waves, heavy rains, droughts, storms, fires, tropical hurricanes, etc.

In general, global temperatures have been rising since the mid–20th century, there is no doubt about that. The IPCC and most of the scientific community members believe that global warming is a consequence of the anthropogenic greenhouse effect and that there is a climate crisis. Although taking place at different time intervals, many researches point out that

anthropogenic climate change and COVID-19 are currently the biggest problems of today (*Vinaya Kumar et al.,* 2017; *Klenert et al.,* 2020; *Phillips et al.,* 2020; *Schmidt,* 2021; *IPCC,* 2021; *Feldman* and *Hart,* 2021; *Geiger et al.,* 2021; *Meijers et al.,* 2021). The solution to the climate crisis is to stop the anthropogenic emissions of CO_2 and other gases that pollute the atmosphere, i.e., to decarbonize the global economy, which means stopping the burning of fossil fuels and switching to the use of so-called green energy (*Waldhoff* and *Fawcett,* 2011; *Friman* and *Hjerpe,* 2015; *Yang et al.,* 2019; *Wei et al.,* 2020; *IPCC,* 2021; *Murali et al.,* 2021). It should be noted that higher temperatures also mean excess energy in the atmosphere, and it is very likely that more frequent weather and climate extremes occur as a consequence of the release of that excess energy (*Burić et al.,* 2011). Thus, it is generally known that most of the scientific community and public opinion believe that global warming is a consequence of the anthropogenic greenhouse effect, but there are many authors who point out that changes in temperature, precipitation, clouds, and other climatic elements can be attributed to natural factors, i.e., variations in atmospheric oscillations (e.g., *Burić et al.,* 2018, 2019, 2021; *Tosunoglu et al.,* 2018; *Serykh* and *Sonechkin,* 2020; *Burić* and *Stanojević,* 2020; *Han* and *Sun,* 2020; *Mihajlović et al.,* 2021).

When it comes to the impact of variations in ocean–atmosphere oscillations (common name for teleconnection) on weather and climate, much more work is focused on the Northern Hemisphere. Therefore, the aim of this paper is to investigate the dynamics and possible causes of temperature change in the Southern Hemisphere region. The two oscillations that are, among others, spatially related to the Southern Hemisphere are the El Niño–Southern Oscillation (ENSO) phenomenon and the Antarctic Oscillation (AAO). However, the ENSO phenomenon has an impact on a global scale as well. All oscillations have a positive and negative phase. When a certain phase dominates, in some areas it is warmer, and in others it is colder, i.e., in some places it is wetter, while in other parts there is less precipitation compared to the usual state. One of the most well-known interactive connections between the ocean and the atmosphere is the occurrence of ENSO, which refers to periodic changes in water temperature in the central and eastern areas of the tropical Pacific Ocean. In the time intervals ranging from about three to seven years, surface water temperatures in the tropics of the Pacific Ocean increase (El Niño) or decrease (La Niña) by 1–3 °C, compared to the normal (*Ducić* and *Luković,* 2005; *Zubair et al.,* 2007; *Burić et al.,* 2011).

The Antarctic Oscillation (AAO) is the dominant pattern of non-seasonal variations of tropospheric circulation south of 20°S latitudes, and is characterized by anomalies of surface pressure of opposite sign compared to the usual state between two dipoles – one above Antarctica and the other in the zone between 40–50°S (*Thompson* and *Wallace,* 2000; *Thompson et al.,* 2000). Typical fluctuations in the altitude of AAO are associated with anomalies greater than 30 m above the pole and the opposite sign of 5–10 m magnitude

across the width of New Zealand. The AAO counterpart in the Northern Hemisphere is the Arctic Oscillation (AO). AAO is also called Southern Annular Mode (SAM). Some authors believe that there is a link between ENSO and AAO (e.g., *González–Reyes* and *Muñoz,* 2013), and these two patterns have a link to the Pacific Decadal Oscillation (*Boisier et al.,* 2018). In essence, AAO refers to strong winds orbiting Antarctica. When they are strong, which is characterized as a positive phase of AAO (AAO+), cold air does not descend to lower latitudes, air pressure over Antarctica is lower, so the southwest winds (SWW) and southern subtropical front (STF) are stronger and shifted to the pole. During AAO+, Antarctica is colder than usual, especially the eastern part (the Ross Sea ice and the Marie Byrd Land). Also, AAO+ usually lowers temperatures on the continents of the Southern Hemisphere, especially in the south of Argentina. As for precipitation, during AAO+, the western part is wetter, and the eastern part of Antarctica is drier. During the negative phase (AAO–), the strong Antarctic vortex weakens, while the cold air descends further south and brings a drop in temperature in the middle latitudes. At that time, the temperature and the pressure in Antarctica were higher, and a bigger part of the continent received less rainfall than usual (*Carvalho et al.,* 2005), while SWW and STF shifted to lower latitudes (*Fig. 2*). *Baldwin* and *Dunkerton* (2001) emphasize that the vortex ring around the South Pole (AAO) is wider and stronger than above the North Pole (AO). This is explained by the fact that there are large land masses in the Northern Hemisphere, which do not allow the polar air ring to expand and strengthen as in the Antarctic region.

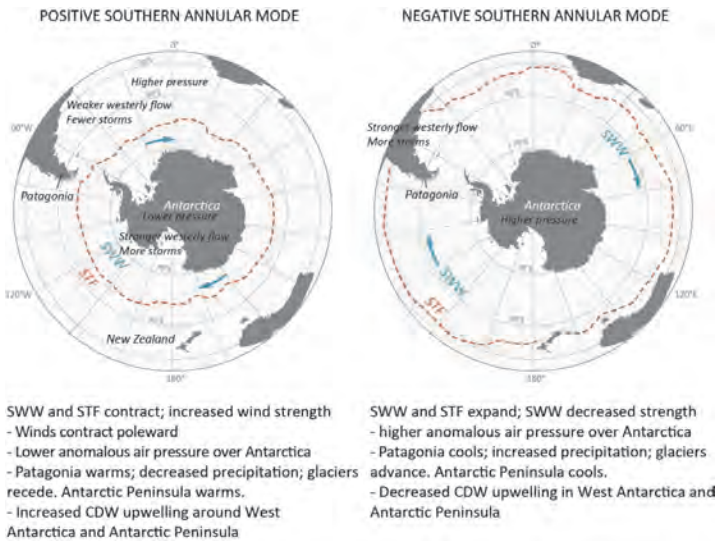

Fig. 2. Positive and negative phase of the Southern Annular Mode (SAM) (https://www.antarcticglaciers.org/glaciers-and-climate/changing-antarctica/southern-annular-mode/).

2. Databases and methodology

Because there is no single index, many researchers use multiple indicators to diagnose ENSO events (*Charles et al.,* 1997; *Hasegawa* and *Hanawa,* 2003; *van Oldenborgh* and *Burgers,* 2005; *Bonham et al.,* 2009; *Alampay* and *dela Torre,* 2019). Data for water surface anomalies in the equatorial Pacific are available for 4 regions (*Fig. 3*), which are designated as: Ninjo 1+2 (0–10°S, 90°W–80°W), Ninjo 3 (5°N–5°S, 150°W–90°W), Ninjo 4 (5°N–5°S, 160°E–150°W), and Ninjo 3.4 (5°N–5°S, 170–120°W). Positive values of the SST–ENSO (sea surface temperature -ENSO) index indicate the occurrence of El Niño (higher water temperature), and negative deviations of this indicator indicate La Niña (lower water temperature in the equatorial part of the Pacific). Differences in water temperature in relation to the usual state cause changes in air oscillation (Southern Oscillation). Thus, this phenomenon is collectively called ENSO.

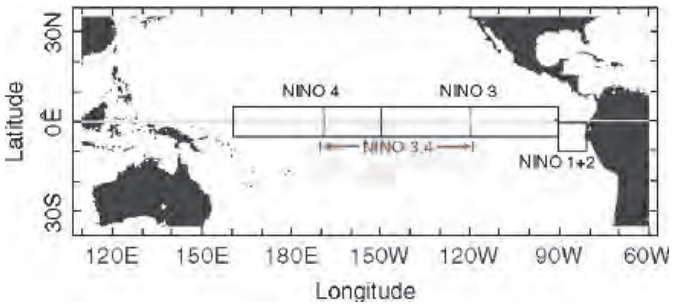

Fig. 3. Regions of the equatorial Pacific for wich SST-ENSO anomalies are monitored (*Zubair et al*., 2007).

There are several indices for AAO as well (*Garreaud et al.,* 2009; *Villalba et al.,* 2012; *Boisier et al.,* 2018). For example, one indicator of AAO variability is the change in ground pressure (*Gong* and *Wang,* 1999; *Marshall,* 2003). Other indices are related to the variations in geopotential heights of 850, 700, and 500 hPa. Based on data on geopotential altitudes, the National Centers for Environmental Prediction (NCEP) and the National Center for Atmospheric Research (NCAR), at NOAA, using a special so–called rotating technology, calculated AAO indices in the range between 20°–90°S.

For the purposes of this paper, a Southern Hemisphere temperature database of the latest versions of HadCRUT5 and NASA–GISS was formed. For ENSO we used data from the Ninjo 3.4 region (otherwise the most frequently used index when it comes to this teleconnection), and for AAO we used the ground pressure variability index and the index of changes in geopotential altitudes of 850 and 700 hPa, as well as the SAM (SAMI) index which

represents a modification of the AAO index. We also used data on atmospheric CO_2 concentration, the energy impact of greenhouse gases (GHG) in W/m^2 (radiation forcing), and the Annual Greenhouse Gas Index (AGGI) on temperature. AGGI was introduced by NOAA, and calculations have been performed since 1979 (*Hofmann et al.,* 2006).

Monthly AAO is defined as the difference in normalized monthly zonal mean sea level pressure (SLP) between 40°S and 70°S (*Nan* and *Li,* 2003), while SAM (Southern Annular Mode) is a modification of the AAO index defined by *Gong* and *Wang* (1999), as a difference in the normalized mean zonal SLP between 40°S i 65°S. Thus, the southern dipole at SAMI is somewhat more to the north compared to AAO. *Table 1* contains lists and sources of data used.

Table 1. Lists and data sources for the variables used

Variable	Source	Unit	Period
HadCRUT5	https://crudata.uea.ac.uk/cru/data/temperature/#datdow	°C	1901–2021
NASA–GISS	https://data.giss.nasa.gov/gistemp/graphs_v4/	°C	1901–2021
CO_2	https://gml.noaa.gov/webdata/ccgg/trends/co2/co2_mm_mlo.txt	ppm	1959–2021
CO_2, CH_4, N_2O, CFCs (AGGI)	https://gml.noaa.gov/aggi/aggi.html	W/m^2	1979–2020
NINO3.4	https://psl.noaa.gov/gcos_wgsp/Timeseries/Nino34/	°C	1901–2021
AAO–slp	https://psl.noaa.gov/data/20thC_Rean/timeseries/monthly/AAO/	hPa	1901–2012
AAO–850	http://research.jisao.washington.edu/data/aao/	gpm (geopotential)	1948–2002
AAO–700	https://www.cpc.ncep.noaa.gov/products/precip/CWlink/daily_ao_index/aao/aao.shtml	gpm	1979–2021
SAM–slp	http://www.nerc-bas.ac.uk/public/icd/gjma/newsam.1957.2007.seas.txt	hPa	1957–2021

According to the recommendation of the World Meteorological Organization (*WMO,* 1966), as well as others (e.g., *Mondal et al.,* 2012), we used the nonparametric Sen method in order to calculate the trend, and its significance was tested by the Mann–Kendall test (*Mann,* 1945; *Kendall,* 1975; *Salmi et al.,* 2002). Significance of the trend was assessed at the risk level of 0.001, 0.01, 0.05, and 0.1 (degree of hypothesis accuracy of 99.9, 99, 95, and 90%). The Pearson's correlation

coefficient was calculated in order for the the relationship between the Southern Hemisphere temperature and ENSO, i.e., AAO (SAM) to be examined, while statistical significance was tested using a student test at the hypothesis level of 95% ($p<0.05$) and 99% ($p<0.01$). Estimates of the considered variables were made on annual and seasonal levels.

3. Results

3.1. Southern Hemisphere temperature trend

According to HadCRUT5 data, the results of trend calculations indicate that in the previous 121 years (1901–2021), the mean temperature in the Southern Hemisphere increased, both annually and seasonally (*Fig. 4*). Trend values are uniform and range from 0.08–0.09 °C/decade. Both annual and seasonal values show a statistically significant trend of increasing temperature at the risk level of $p<0.001$ (the highest degree of accuracy of the hypothesis of 99.9%). The trend is also calculated for the period from 1951 to 2021 and the same qualitative results were obtained, but there is a greater trend of increasing temperature (0.11–0.12 °C/decade). In other words, the temperature in the Southern Hemisphere has been increasing more intensely since the middle of the 20th century, but the increase in temperature of the Northern Hemisphere is still larger (about 0.19 °C/decade).

For the NASA–GISS network, we had only the average annual temperatures for the Southern Hemisphere. This network shows that in the period from 1901 to 2021, the trend of annual temperature in the Southern Hemisphere was 0.09 °C/decade, while for the period 1951–2021, the trend is slightly higher (0.12 °C/decade) compared to the HadCRUT5 database. The NASA–GISS database gives temperature anomalies for certain belts, which we found very interesting for analysis. Namely, according to climate models, one of the most indicative indicators of global warming should be the polar amplification (more intense warming at the poles compared to the rest of the planet). In other words, as many authors point out (e.g., *Budyko,* 1969; *Sellers,* 1969; *Holland* and *Bitz,* 2003; *Taylor et al.,* 2013; *Lee,* 2014; *Cvijanovic* and *Caldeira*, 2015; *Oldfield,* 2016; *Stuecker et al.,* 2018), in the conditions of increasing GHG concentration, the ground temperature should increase more intensively going from the equator to the poles.

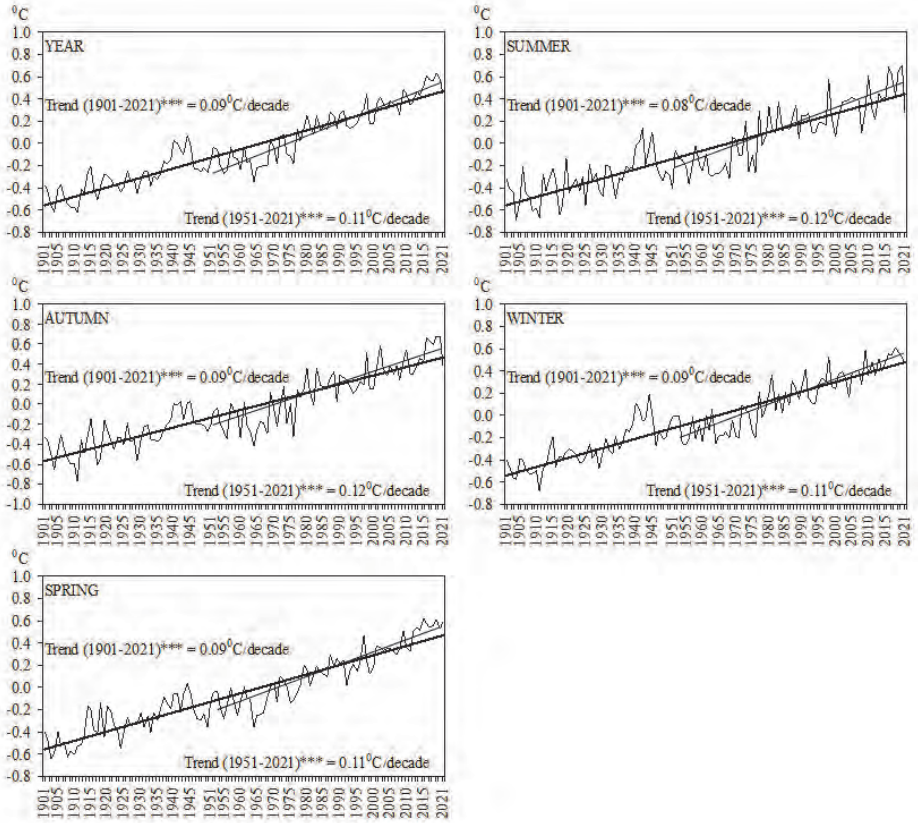

Fig. 4. The trend of seasonal and annual temperatures in the Southern Hemisphere in the periods 1901–2021 and 1951–2021 (***Significant trend: p<0.001).

To test this, a trend was calculated for four belts in the Southern Hemisphere: 0°–24°S, 24°S–44°S, 44°S–64°S, and 64°S–90°S. In all four belts, the temperature trend is positive and statistically significant at the highest level of hypothesis acceptance (p<0.001), both in the period 1901–2021 and 1951–2021. However, in the most temperate latitudes (44°S–64°S) temperatures rise more slowly than in the tropics. Moreover, in the period 1951–2021, there was a slightly more intense trend of temperature increase in the tropical (0.14 °C/decade) than in the polar (0.13 °C/decade) latitudes. This was unexpected taking into consideration the models of dominance of anthropogenic greenhouse effect, i.e., the opposite should be expected. Interestingly, in this belt (44–64°S), the positive trend in the period 1951–2021 (0.06 °C/decade) even decreased compared to the period 1901–2021 (0.07 °C/decade). We conclude that the polar amplification does not work in the Southern Hemisphere. On the

other hand, in the Northern Hemisphere, polar amplification exists, because the trend of increasing annual temperature is more intense going from the equator to the Arctic. The results further showed that in the period between 1951 and 2021, temperate and polar latitudes heat up significantly faster in the Northern Hemisphere than in the Southern Hemisphere (*Fig. 5*).

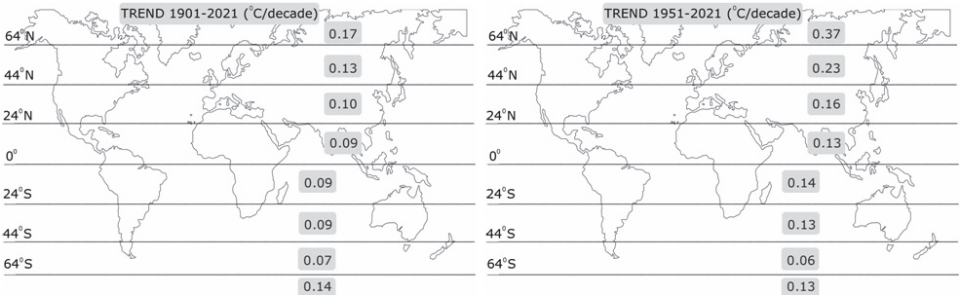

Fig. 5. Trend of average annual temperature on the planet by belts in the periods 1901–2021 and 1951–2021.

3.2. Possible causes of rising temperatures in the Southern Hemisphere

It could be said that there is a scientific consensus that the dominant cause of the rise in temperature is the increased atmospheric concentration of greenhouse gases (GHG). In this regard, the correlation between the Southern Hemisphere temperature and CO_2 concentration was examined. Data from the Mauna Loa station for 1958 are not complete, thus the correlation for the period between 1959 and 2021 was calculated and coefficients from 0.83 (southern summer) to 0.93 (southern spring) were obtained. Annually, the correlation between the mean Southern Hemisphere temperature and CO_2 concentration (in ppm) is 0.92. Both annual and seasonal values of correlation coefficients meet the conditions of statistical significance at the highest level of hypothesis acceptance ($p<0.01$).

It was previously mentioned that higher temperature also means excess energy in the atmosphere, which is a consequence of a very probable increase in the concentration of greenhouse gases. Beginning in 1979, NOAA used several empirical equations to calculate the atmospheric concentrations of greenhouse gases and the energy impact, and thus determined the radiation effect (in W/m^2) on air temperature (*Fig. 6*). Therefore, the available data for the period between 1979 and 2020 (*Table 2*) on the energy impact of CO_2, CH_4, N_2O, and several gases from the group of chlorofluorocarbon compounds (CFCs) was used. Based

on the concentration of all gases, i.e., their energy impact, NOAA has defined an unique Annual Greenhouse Gas Index (AGGI).

For the period between 1979 and 2020, the relationship between the annual values of the Southern Hemisphere temperature and the energy impact of GHG is positive (direct correlations) and statistically significant at the highest level of hypothesis acceptance (on the 99% hypothesis level). The correlation coefficient between the radiation effect of annual CO_2 values (AGGI) and the Southern Hemisphere temperature is 0.87 (0.85). This is a result of the fact that with the growth of GHG, positive radiation forcing increases (*Table 3*).

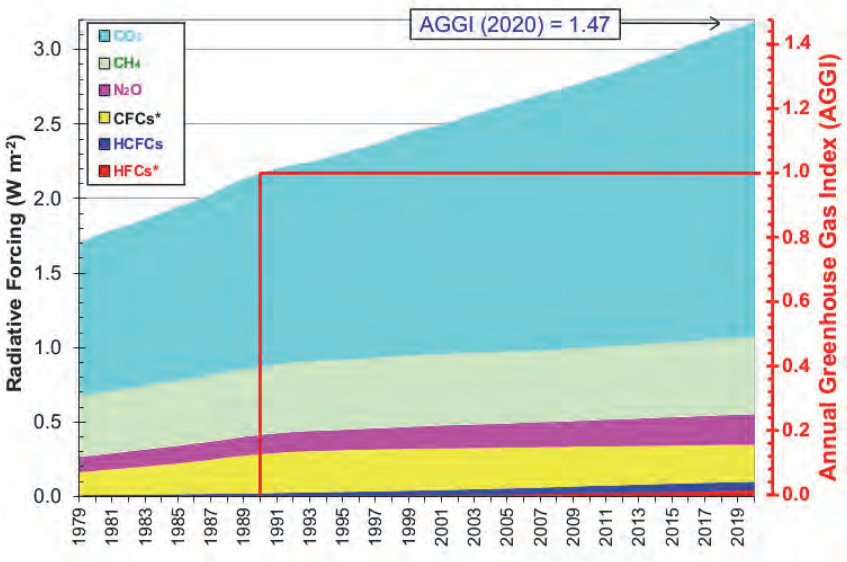

Fig. 6. Radiative forcing, relative to 1750, of virtually all long–lived greenhouse gases. The NOAA Annual Greenhouse Gas Index (AGGI), which is indexed to 1 for the year 1990, is shown on the right axis. The "CFC*" grouping includes some other long–lived gases that are not CFCs (e.g., CCl_4, CH_3CCl_3, and Halons), but the CFCs account for the majority (95% in 2020) of this radiative forcing. The "HCFC" grouping includes the three most abundant of these chemicals (HCFC–22, HCFC–141b, and HCFC–142b). The "HFC" grouping includes the most abundant HFCs (HFC–134a, HFC–23, HFC–125, HFC–143a, HFC–32, HFC–152a, HFC–227ea, and HFC–365mfc) and SF6 for completeness, although SF6 only accounted for a small fraction of the radiative forcing from this group in 2020 (13%). (Source: https://gml.noaa.gov/aggi/aggi.html)

Table 2. Annual global energy impact of GHG (W/m^2) and GHG index (AGGI) for the period 1979–2020

Year	CO_2	Others (CH_4, N_2O, CFC+ other)	Total (CO_2+ other)	AGGI (1990=1)	Year	CO_2	Others (CH_4, N_2O, CFC+ other)	Total (CO_2+ other)	AGGI (1990=1)
1979	1.03	0.67	1.70	0.79	2000	1.52	0.95	2.47	1.14
1980	1.06	0.69	1.75	0.81	2001	1.54	0.96	2.49	1.15
1981	1.08	0.71	1.79	0.83	2002	1.57	0.96	2.53	1.17
1982	1.09	0.73	1.82	0.84	2003	1.60	0.97	2.57	1.19
1983	1.12	0.74	1.86	0.86	2004	1.63	0.97	2.60	1.20
1984	1.14	0.76	1.90	0.88	2005	1.66	0.97	2.63	1.21
1985	1.16	0.78	1.94	0.90	2006	1.69	0.98	2.67	1.23
1986	1.19	0.80	1.98	0.92	2007	1.71	0.98	2.70	1.24
1987	1.21	0.81	2.03	0.94	2008	1.74	0.99	2.73	1.26
1988	1.25	0.84	2.09	0.96	2009	1.76	1.00	2.76	1.27
1989	1.28	0.86	2.13	0.98	2010	1.79	1.00	2.80	1.29
1990	1.29	0.87	2.17	1.00	2011	1.82	1.01	2.83	1.31
1991	1.31	0.89	2.20	1.02	2012	1.85	1.01	2.86	1.32
1992	1.33	0.90	2.23	1.03	2013	1.88	1.02	2.90	1.34
1993	1.34	0.91	2.24	1.04	2014	1.91	1.03	2.94	1.36
1994	1.36	0.91	2.27	1.05	2015	1.94	1.04	2.98	1.38
1995	1.39	0.92	2.30	1.06	2016	1.99	1.04	3.03	1.40
1996	1.41	0.93	2.34	1.08	2017	2.02	1.05	3.07	1.42
1997	1.43	0.93	2.36	1.09	2018	2.05	1.06	3.11	1.43
1998	1.47	0.94	2.41	1.11	2019	2.08	1.06	3.14	1.45
1999	1.50	0.95	2.45	1.13	2020	2.11	1.07	3.18	1.47

Table 3. Values of correlation coefficients between Southern Hemisphere temperature and greenhouse gases (GHG)

Period	GHG	Correlation coefficient				
		Year	Summer	Autumn	Winter	Spring
1959–2021	CO_2 (ppm)	0.92**	0.83**	0.85**	0.89**	0.93**
1979–2020	CO_2 (W/m^2)	0.87**	/	/	/	/
1979–2020	Others (CH_4, N_2O, CFC+other) inW/m^2	0.77**	/	/	/	/
1979–2020	Total (CO_2+others) inW/m^2	0.84**	/	/	/	/
1979–2020	AGGI	0.85**	/	/	/	/

Significant correlation: *$p < 0.05$, **$p < 0.01$

Previous results show that the anthropogenic greenhouse effect (AGE) undoubtedly has an impact on the Southern Hemisphere temperature as well as on a global scale (not shown). But, we believe that it is wrong to exclude the consideration of the influence of natural factors, primarily the variations of atmospheric and oceanic circulations. Therefore, the relationship between the temperature of the Southern Hemisphere and the indicators of variation of ENSO and AAO was examined in the following text.

When it comes to the ENSO phenomenon, the calculation results show that this phenomenon has an impact on the temperature of the Southern Hemisphere, statistically significantly during summer, autumn, and winter in the Southern Hemisphere, as well as annually. During the spring in the Southern Hemisphere, ENSO has no statistically significant impact (correlation is 0.16).

We used several indicators (indexes) for the variability of the Antarctic Oscillation (AAO and SAM). The ground temperature depends on the structure of the atmosphere at sea level and 850 hPa altitude, while events at 700 hPa altitude do not have a dominant impact, in general. Correlation calculations have confirmed this. Namely, the correlation between the AAO–700 hPa index and the Southern Hemisphere temperature is statistically insignificant. On the other hand, the correlation of annual values of SAM–slp, AAO–slp, and AAO–850 with the Southern Hemisphere temperature is 0.46, 0.66, and 0.69, and is statistically significant at 99% of the hypothesis acceptance level ($p < 0.01$). At the seasonal level, it is noticed that the influence of AAO–slp, SAM–slp, and AAO–850 on the temperature is strongest during the winter and spring in the Southern Hemisphere (*Table 4*).

Table 4. Values of correlation coefficients between the Southern Hemisphere temperature and ENSO and AAO

Period	**Teleconnection**	**Corelation coefficient**				
		Year	**Summer**	**Autumn**	**Winter**	**Spring**
1901–2021	ENSO3.4	0.19*	0.27**	0.32**	0.19*	0.16
1957–2021	SAM–slp	0.46**	0.20	0.10	0.47**	0.38**
1901–2012	AAO–slp	0.66**	0.31**	0.40**	0.46**	0.48**
1948–2002	AAO–850	0.69**	0.37**	0.44**	0.47**	0.47**
1979–2021	AAO–700	0.21	–0.19	–0.03	–0.14	0.03

Significant correlation: *$p < 0.05$, **$p < 0.01$

4. Discussion

Analyzing the global annual temperature for the entire observed period (1901–2021) using both datasets (HadCRUT5 and NASA–GISS) shows the dominance of negative deviations until 1976, while since 1977, each year has been warmer than the base period. This is in line with the IPCC and WMO reports. Namely, the IPCC in the Third Report (IPCC, 2001) pointed out that in the 20th century most of the warming took place during two periods: 1910–1945 and 1976–2000, while the period from 1945 to 1975 registers the cessation of global warming. According to the IPCC, natural factors (primarily changes in solar radiation and volcanic activity) can be attributed to the observed warming in the first half of the 20th century, while the rise in temperature in the last five decades is attributed to human activities (primarily to fossil fuel combustion).

In the period of positive anomalies, it is interesting to see the period 1977–2021, during which decade (10-year-long period) the trend was the lowest, and during which it was the highest, because the Sena method and Mann-Kendall test are not recommended for series shorter than 10 parameters. If there is an intensification of warming, then it is to be expected that the value of the positive trend is the lowest in the first, and the highest in the last 10-year-long period. However, according to the HadCRUT5 database, the budget results showed that the positive trend had the greatest value in the decade from 2008 to 2017 and from 2011 to 2020. In both periods the trend is the same (0.42 °C/decade) and statistically significant at the highest level of hypothesis acceptance (at 99.9% significance level). On the other hand, the lowest value of the trend (which was statistically insignificant) was registered in the first decade, which was to be expected. But the trend in the first 10-year-long period (1977–1986) was not positive but negative (–0.01 °C/decade), which was not to be expected. All other 10-year-long periods, with a shift of one year (1978–1987, 1979–1988, ... 2012–2021) register a positive trend.

Thus, in the 1977–1986 subperiod the trend of global temperature is insignificantly negative, and it received a positive sign as early as the following year (1987) maintained until the end of the period (1977–1987, 1977–1988, ..., 1977–2021). The significance of the positive trend was obtained from the time series: 1977–1990 and further (1977–1990, 1977–1991, 1977–1992, ...). According to the above mentioned facts, it could be concluded that in the period from 1977 to 1990 there was a slowdown in global temperature rise. This slowdown or so-called t cessation of global warming is also observed in the 1987–1996 subperiod, when the trend was insignificant: 0.026 °C/decade. Also, in the 1980–1989 subperiod, a slowdown in global warming was recorded as well, and the positive trend was insignificant until 1994 (1980–1994). *Xie* and *Kosaka* (2017) note the cessation of global warming in the 1998–2013 subperiod, although our estimates do not confirm this. It is a known fact that in 1997 and 1998, an extremely strong El Niño event took place, and that this

phenomenon was even stronger in 2015 and 2016. Thus, the mentioned authors explain the slowdown in global warming in the mentioned period using variations in the surface temperature of water in the tropical Pacific. The authors point out that the tropical Pacific effect of slowing global temperature rise has a stronger impact on the decadal than interannual variability.

Our analyses also show that the mentioned "pauses" in the increase in global temperature were registered after stronger ENSO phenomena (after 1977, 1987). 2016 was rated as the warmest on our planet in the period of instrumental measurements, and the strongest ENSO phenomena happened in 2015 and 2016. The slowdown in the rise in mean annual temperature is more pronounced in the Southern Hemisphere. For example, in the period from 1977 and 1996 (20 years) and in the period from 1998 and 2013 (16 years), the positive trend is insignificant (*Fig. 7*). Moreover, during the 10-year-long period of 1987–1996, there was a slight cooling in the Southern Hemisphere (–0.07 °C/decade).

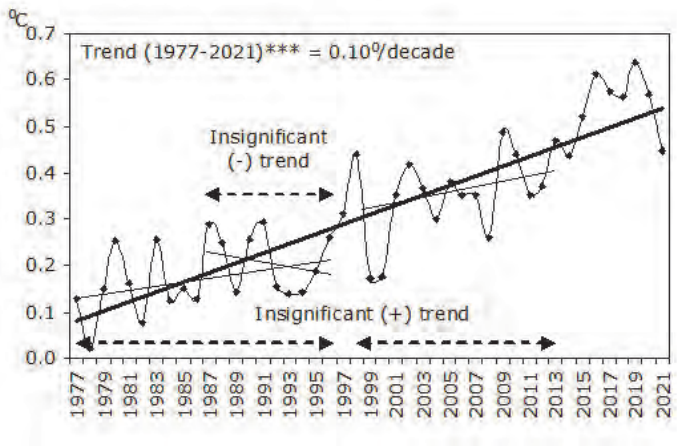

Fig. 7. The trend of the average annual temperature in the Southern Hemisphere in the period of constant positive deviations (1977–2021) (***Significant trend: p<0.001).

When observing the entire period of the 20th and the past years of the 21st century (1901–2021), the trend of rising global temperature, as in the Southern Hemisphere, is statistically significant, and the prevailing opinion is that it is caused by human activities. There were sub–periods of slowing (interruption) of global (hemispheric) warming during this period and this is mentioned in several papers (eg: *Kosaka* and *Xie*, 2013; *Chen* and *Tung*, 2014; *England et al*., 2014; *Amaya et al*., 2015; *Xie* and *Kosaka*, 2017). Our analysis confirms the interruptions in temperature rise (global and in the southern hemisphere) and shows that even in the period with constant positive deviations (1977–2021), there were shorter subperiods with mild cooling. The intention is not to open a debate on the validity

of the theory of the dominance of the anthropogenic greenhouse effect, but to point out that there were shorter and longer subperiods when natural factors had a dominant influence on temperature. This study shows the impact of some of them (ENSO, AAO), with the aim of emphasizing the need to consider variations of natural factors in the era of modern climate change, in addition to anthropogenic impact. Of course, the impact of the so-called feedback effect, i.e., the fact that changes in one factor in the climate system are reflected in variations in other components of the system, should be taken into consideration.

5. Conclusion

The main goal of this paper was to determine the magnitude and significance of the trend of mean seasonal and annual temperatures in the Southern Hemisphere and to examine the relationship with the GHG radiation exposure and ENSO and AAO teleconnections. The period between 1901 and 2021 and the subperiod between 1951 and 2021 are considered. According to the HadCRUT5 database, the calculation results showed that there was a significant increase in seasonal and annual temperatures in the Southern Hemisphere, and that it got intensified in the period between 1951 and 2021 (0.11–0.12 °C/decade) more than in the entire observed period, from 1901 to 2021 (0.08–0.09 °C/decade). In order to check the polar amplification in the Southern Hemisphere, using the NASA–GISS database, the annual temperature trend was calculated separately for four belts: 0°–24°S, 24°S–44°S, 44°S–64°S, and 64°S–90°S. The results showed that polar amplification did not function in the Southern Hemisphere, which was not in line with the models of dominance of the anthropogenic greenhouse effect.

Taking the considered factors into consideration, it was determined that GHG concentration indicators had the strongest interactive connection with the Southern Hemisphere temperature. For example, for the period between 1959 and 2021, the correlation coefficients between CO_2 concentration (in ppm) and Southern Hemisphere temperature range from 0.83 (southern summer) to 0.93 (southern spring). It was further determined that a significant positive radiation forcing (in W/m^2) of GHG (CO_2, CH_4, N_2O, CFCs, and AGGI) was exerted to the Southern Hemisphere temperature. There was a positive correlation between ENSO and the temperature of the Southern Hemisphere, and it was significant during the southern summer, autumn, and winter, as well as on annual basis. Variations in the structure of the atmosphere at the sea level and the altitude of 850 hPa, shown via the AAO and SAM index indicated, that this oscillation had a significant impact on the temperature of the Southern Hemisphere. Thus, it would not be superfluous to repeat that today's civilization should do everything not to contribute further to pollution of the GHG in the atmosphere and warming of our planet, but in order to understand modern climate change, it is necessary to consider natural factors, such as variations in atmospheric oscillations.

References

Alampay, E.A. and *dela Torre, D.*, 2019: Addressing Slow Onset Disasters: Lessons from the 2015–2016 El Niño in the Philippines. In: (eds. *Leal Filho W.*) Handbook of Climate Change Resilience. Springer, Cham. 1–18. https://doi.org/10.1007/978-3-319-71025-9_192-1

Amaya, D.J., Xie, S.P., Miller, A.J., and *McPhaden, M.J.*, 2015: Seasonality of tropical Pacific decadal trends associated with the 21st century global warming hiatus. *JGR: Oceans 120*, 6782–6798. https://doi.org/10.1002/2015JC010906

Baldwin, M.P. and *Dunkerton, T.J.*, 2001: Stratospheric Harbingers of Anomalous Weather Regimes. *Science 294*(5542), 581–584. https://doi.org/10.1126/science.1063315

Bonham, S.G., Haywood, A.M., Lunt, D.J., Collins, M., and *Salzmann, U.*, 2009: El Niño–southern oscillation, Pliocene climate and equifinality. *Phil. Trans. R. Soc. A. 367*,127–156. https://doi.org/10.1098/rsta.2008.0212

Boisier, J.P., Álvarez–Garretón, C., Cordero, R.R., Damiani, A., Gallardo, L., Garreaud, R.D., Lambert, F., Ramallo, C., Rojas, M., and *Rondanelli, R.*, 2018: Anthropogenic drying in central–southern Chile evidenced by long–term observations and climate model simulations. *Elementa–Science of the Anthropocene 6*, 74. https://doi.org/10.1525/elementa.328

Budyko, M.I., 1969: The effect of solar radiation variations on the climate of the Earth. *Tellus 21*, 611–619. https://doi.org/10.3402/tellusa.v21i5.10109

Burić, D., Dragojlović, J., Penjišević–Sočanac, I., Luković, J., and *Doderović, M.*, 2019: Relationship Between Atmospheric Circulation and Temperature Extremes in Montenegro in the Period 1951–2010. Climate Change Adaptation in Eastern Europe, 29–42. Springer. https://doi.org/10.1007/978-3-030-03383-5_3

Burić, D.B., Dragojlović, J.M., Milenković, M.Đ., Popović, Lj.Z., and *Doderović, M.M.*, 2018: Influence of variability of the East Atlantic Oscillation on the air temperature in Montenegro. *Thermal Science 22*(1 Part B): 759–766. https://doi.org/10.2298/TSCI170710211B

Burić, D., Doderović, M., Dragojlović, J., and *Penjišević, I.*, 2021: Extreme weather and climate events in Montenegro – case study, November 2019. *Weather 76*(11), 383–388. https://doi.org/10.1002/wea.3885

Burić, D. and *Stanojević G.*, 2020: Trends and possible causes of cloudiness variability in Montenegro in the period 1961–2017. *Climate Research 81*, 187–205. https://doi.org/10.3354/cr01615

Burić, D., Ducić, V., and *Luković J.*, 2011: *Kolebanje klime u Crnoj Gori u drugoj polovini XX i početkom XXI vijeka.* Crnogorska akademija nauka i umjetnosti, Podgorica. ISBN 978–86–7215–283–8; COBISS.CG–ID 19199760. (In Montenegrin)

Carvalho, L.M.V., Jones, C., and *Ambrizzi, T.*, 2005: Opposite Phases of the Antarctic Oscillation and Relationships with Intraseasonal to Interannual Activity in the Tropics during the Austral Summer. *J Climate 18*, 702–718. https://doi.org/10.1175/JCLI-3284.1

Charles, C.D., Hunter, D.E., and *Fairbanks, R.G.*, 1997: Interaction between the ENSO and the Asian monsoon in a coral record of tropical climate. *Science 2277*, 925–928. https://doi.org/10.1126/science.277.5328.925

Chen, X. and *Tung, K.K.*, 2014: Varying planetary heat sink led to global–warming slowdown and acceleration. *Science 345*, 897–903. https://doi.org/10.1126/science.1254937

Cvijanovic, I. and *Caldeira, K.*, 2015: Atmospheric impacts of sea ice decline in CO_2 induced global warming. *Climat Dyn. 44*, 1173–1186. https://doi.org/10.1007/s00382-015-2489-1

Ducić, V. and *Luković, J.*, 2005: Possible connection between El Nino Southern oscillation (ENSO) and precipitation variability in Serbia. *Proceedings – Faculty of Geography, University of Belgrade 53*, 13–22. https://scindeks.ceon.rs/article.aspx?artid=0351-465X0553013D

England, M.H., McGregor, S., Spence, P., Meehl, G.A., Timmermann, A., Cai, W., Gupta, A.S., and *McPhaden M.J.*, 2014: Recent intensification of wind–driven circulation in the Pacific and the ongoing warming hiatus. *Nat. Climat. Change 4*, 222–227. https://doi.org/10.1038/nclimate2106

Feldman, L. and *Hart, P.S.*, 2021: Upping the ante? The effects of "emergency" and "crisis" framing in climate change news. *Climatic Change 169*, article 10. https://doi.org/10.1007/s10584-021-03219-5

Friman, M. and *Hjerpe, M.,* 2015: Agreement, significance, and understandings of historical responsibility in climate change negotiations. *Climate Policy 15*, 302–320. https://doi.org/10.1080/14693062.2014.916598

Garreaud, R.D., Vuille, M., Compagnucci, R., and *Marengo, J.,* 2009. Present–day South American climate. *Palaeogeography, Palaeoclimatology, Palaeoecology 281*, 180–195. https://doi.org/10.1016/j.palaeo.2007.10.032

Geiger, N., Gore, A., Squire, C.V., and *Attari, S.Z.,* 2021: Investigating similarities and differences in individual reactions to the COVID–19 pandemic and the climate crisis. *Climatic Change 167*, article 1. https://doi.org/10.1007/s10584-021-03143-8

González–Reyes, Á. and *Muñoz, A.A.,* 2013: Precipitation changes of Valdivia city (Chile) during the past 150 years. *Bosque (Valdivia) 34*, 200–213. https://doi.org/10.4067/S0717-92002013000200008

Gong, D. and *Wang, S.,* 1999: Definition of Antarctic oscillation index. *Geophys.Res. Lett. 26*, 459–462. https://doi.org/10.1029/1999GL900003

Han, S. and *Sun, J.,* 2020: Potential contribution of winter dominant atmospheric mode over the mid–latitude Eurasia to the prediction of subsequent spring Arctic Oscillation. *Int. J. Climatol. 40*, 2953–2963. https://doi.org/10.1002/joc.6376

Hasegawa, T. and *Hanawa, K.,* 2003: Heat content variability related to ENSO events in the Pacific. *J. Phys. Oceanograph. 33,* 407–421. https://doi.org/10.1175/1520-0485(2003)033<0407:HCVRTE>2.0.CO;2

Hofmann, D.J., Butler, J.H., Dlugokencky, E.J., Elkins, J.W., Masarie, K., Montzka, S. A., and *Tans, P.,* 2006: The role of carbon dioxide in climate forcing from 1979–2004: Introduction of the Annual Greenhouse Gas Index. *Tellus B: 58*, 614–619. https://doi.org/10.1111/j.1600-0889.2006.00201.x

Holland, M.M. and *Bitz, C.M.,* 2003: Polar amplification of climate change in coupled models. *Climate Dynamics 21*, 221–232. https://doi.org/10.1007/s00382-003-0332-6

IPCC, 2001: Climate Change 2001*:* The Scientific Basis is the most comprehensive and up–to–date scientific assessment of past, present and future climate change. Contribution of Working Group I to the Third Assessment Report of the Intergovernmental Panel on Climate Change (ed.: *J.T. Houghton, et al.*). Cambridge University Press, Cambridge, UK and New York, USA, 2001.

IPCC, 2021: Summary for Policymakers. In: Climate Change 2021: The Physical Science Basis. Contribution of Working Group I to the Sixth Assessment Report of the Intergovernmental Panel on Climate Change [(eds. *Masson–Delmotte, V., P. Zhai, A. Pirani, S. L. Connors, C. Péan, S. Berger, N. Caud, Y. Chen, L. Goldfarb, M. I. Gomis, M. Huang, K. Leitzell, E. Lonnoy, J.B.R. Matthews, T. K. Maycock, T. Waterfield, O. Yelekçi, R. Yu* and *B. Zhou*)]. Cambridge University Press. In Press.

Klenert, D., Funke, F., Mattauch, L., and *O'Callaghan, B.,* 2020: Five Lessons from COVID–19 for Advancing Climate Change Mitigation. *Environ. Resource Econ. 76*, 751–778. https://doi.org/10.1007/s10640-020-00453-w

Kendall, M.G., 1975: Rank Correlation Methods, 4th edition. London: Charles Griffin.

Kosaka, Y. and *Xie, S.P.,* 2013: Recent global–warming hiatus tied to equatorial Pacific surface cooling. *Nature*, 501, 403–407. https://doi.org/10.1038/nature12534

Lee, S., 2014: A theory for polar amplification from a general circulation perspective. *Asia–Pacific J. Atmos. Sci. 50,* 31–43. https://doi.org/10.1007/s13143-014-0024-7

Marshall, GJ., 2003: Trends in the Southern Annular Mode from Observations and Reanalyses. *J. Climate 16*, 4134–4143. https://doi.org/10.1175/1520-0442(2003)016<4134:TITSAM>2.0.CO;2

Mann, H.B., 1945: Nonparametric tests against trend. *Econometrica 13*, 245–259 https://doi.org/10.2307/1907187

Meijers, M.H.C., Scholz, C., Torfadóttir, R., Wonneberger, A., and *Markov, M.,* 2021: Learning from the COVID–19 pandemic to combat climate change: comparing drivers of individual action in global crises. *J. Environ. Stud. Sci.* 11. https://doi.org/10.1007/s13412-021-00727-9

Mihajlović, J., Burić, D., Ducić, V., and *Milenković, M.,* (2021). Synoptic characteristics of an extreme weather event: The tornadic waterspout in Tivat (Montenegro), on June 9, 2018. *Geographia Polonica 94*, 69–90. https://doi.org/10.7163/GPol.0194

Mondal, A., Sananda, K., and *Mukhopadhyay, A.,* 2012: Rainfall trend analysis by Mann–Kendall test: a case study of northeastern part of Cuttack District, Orissa. *Int. J. Geology, Earth Environ. Sci. 2*, 70–78. https://www.researchgate.net/publication/268438767

Morice, C.P., Kennedy, J.J., Rayner, N.A., Winn, J.P., Hogan, E., Killick, R.E., Dunn, R.J.H., Osborn, T.J., Jones, P.D., and *Simpson, I.R.,* 2021: An updated assessment of near–surface temperature change from 1850: the HadCRUT5 dataset. *J. Geophys. Res. 126*, e2019JD032361. https://doi.org/10.1029/2019JD032361

Murali, R., Kuwar, A., and *Nagendra, H.,* 2021: Who's responsible for climate change? Untangling threads of media discussions in India, Nigeria, Australia, and the USA. *Climatic Change 164*, article number 51. https://doi.org/10.1007/s10584-021-03031-1

Nan, S.L. and *Li, J.P.,* 2003: The relationship between summer precipitation in the Yangtze River valley and the previous Southern Hemisphere Annular Mode. *Geophys. Res. Lett. 30*(24), 2266. https://doi.org/10.1029/2003GL018381

Oldfield, J.D., 2016: Mikhail Budyko's (1920–2001) contributions to Global Climate Science: from heat balances to climate change and global ecology. *Adv. Review. 7*(5), 682–692. https://doi.org/10.1002/wcc.412

Osborn, T.J., Jones, P.D., Lister, D.H., Morice, C.P., Simpson, I.R., Winn, J.P., Hogan, E., and *Harris, I.C.,* 2021: Land surface air temperature variations across the globe updated to 2019: the CRUTEM5 dataset. *J. Geophys. Res.: Atmospheres 126*, e2019JD032352. https://doi.org/10.1029/2019JD032352

Phillips, C.A., Caldas, A., Cleetus, R., Dahl, K.A., Declet–Barreto, J., Licker, R., Merner, L.D., Ortiz–Partida, J.P., Phelan, A.L., Spanger–Siegfried, E., Talati, S., Trisos, C.H., and *Carlson, C.J.*, 2020: Compound climate risks in the COVID–19 pandemic. *Nat. Clim. Chang. 10*, 586–588. https://doi.org/10.1038/s41558-020-0804-2

Salmi, T., Määttä, A., Anttila, P., Ruoho–Airola, T., and *Amnell, T.,* 2002: *Detecting Trends of Annual Values of Atmospheric Pollutants by the Mann–Kendall Test and Sen's Slope Estimates–The Excel Template Application MAKESENS.* Finnish Meteorolog. Institute, Helsinki: Publications on Air Quality 31.

Schmidt, R.C., 2021: Are there similarities between the Corona and the climate crisis? *J Environ. Stud. Sci. 11*, 159–163. https://doi.org/10.1007/s13412-021-00666-5

Serykh, I.V. and Sonechkin, D.M., 2020: El Niño forecasting based on the global atmospheric oscillation. *International Journal of Climatology, 41*(7), 3781–3792. https://doi.org/10.1002/joc.6488

Sellers, W.D., 1969: A Global Climatic Model Based on the Energy Balance of the Earth–Atmosphere System. *J. Appl. Meteorol. 8*, 392–400. https://doi.org/10.1175/1520-0450(1969)008<0392:AGCMBO>2.0.CO;2

Stuecker, M.F., Bitz, C.M., Armour, K.C., Proistosescu, C., Kang, S.,M.; Xie, S.P., Kim, D., McGregor, S., Zhang, W., Zhao, S., Cai, W., Dong, Y., and *Jin, F.F.*, 2018: Polar amplification dominated by local forcing and feedbacks. *Nature Climate Change 8*, 1076–1081. https://doi.org/10.1038/s41558-018-0339-y

Taylor, P.C., Ming C., Hu. A., Meehl, J., Washington, W., and *Zhang, G.J.*, 2013: A Decomposition of Feedback Contributions to Polar Warming Amplification. *J. Climate* 23, 7023–7043. https://doi.org/10.1175/JCLI-D-12-00696.1

Tosunoglu, F., Can., I., and *Kahya, E.,* 2018: Evaluation of spatial and temporal relationships between large–scale atmospheric oscillations and meteorological drought indexes in Turkey. *Int. J. Climatol. 38*, 4579–4596. https://doi.org/10.1002/joc.5698

Thompson, D.W.J. and *Wallace, J.M.,* 2000: Annular modes in the extratropical circulation. Part I: Month–to–month variability. *J. Climate, 13*, 1000–1016. https://doi.org/10.1175/1520-0442(2000)013<1000:AMITEC>2.0.CO;2

Thompson, D.W.J., Wallace, J.M., and *Hegerl, G.,* 2000: Annular modes in the extratropical circulation. Part II: Trends. *J. Climate, 13*, 1018–1036. https://doi.org/10.1175/1520-0442(2000)013<1018:AMITEC>2.0.CO;2

van Oldenborgh, G.J. and *Burgers, G.,* 2005: Searching for decadal variations in ENSO precipitation teleconnections. *Geophys. Res. Lett. 32*(15), L15701. https://doi.org/10.1029/2005GL023110

Vinaya Kumar, H.M., Shivamurthy, M., Govinda Gowda, V., and *Biradar, G.S.,* 2017: Assessing decision–making and economic performance of farmers to manage climate–induced crisis in Coastal Karnataka (India). *Climatic Change 142*, 143–153. https://doi.org/10.1007/s10584-017-1928-x

Villalba, R., Lara, A., Masiokas, M.H., Urrutia, R., Luckman, B.H., Marshall, G.J., Mundo, I., Christie, D.A., Cook, E., Neukom, R., Allen, K., Fenwick, P., Boninsegna, J.A., Srur, A.M., Morales, M.S., Araneo, D., Palmer, J.G., Cuq, E., Aravena, J.C., Holz, A., and *LeQuesne, C.,* 2012: Unusual Southern Hemisphere tree growth patterns induced by changes in the Southern Annular Mode. *Nature Geoscie. 5*, 793–798. https://doi.org/10.1038/ngeo1613

Waldhoff, S.T. and *Fawcett, A.A.,* 2011: Can developed economies combat dangerous anthropogenic climate change without near–term reductions from developing economies? *Climatic Change 107*, 635. https://doi.org/10.1007/s10584-011-0132-7

Wei, T., Liu, C., Dong, W., Yu H., Yang, S., Yan, Q., and *Hao, Z.,* 2020: Reduction in extreme climate events and potential impacts by the use of technological advances. *Int. J.f Climatol. 41*, 2495–2508. https://doi.org/10.1002/joc.6971

WMO, 1966: Climatic change. Tech Note No 79, WMO, Geneva.

Xie, S.P. and *Kosaka, Y.,* 2017: What Caused the Global Surface Warming Hiatus of 1998–2013? *Curr. Climate Change Rep. 3*, 128–140. https://doi.org/10.1007/s40641-017-0063-0

Yang, S., Dong, W., Chou, J., Dai, T., Hong, T., Xiao, C., Wei, T., Tian, D., and *Ji, D.,* 2019: Quantifying the developed and developing worlds' carbon reduction contributions to Northern Hemisphere cryosphere change. *Int. J. Climatol. 39*, 3231–3240. https://doi.org/10.1002/joc.6014

Zubair, L., Siriwardhana, M., Siriwardhana, M., Chandimala, J., and *Yahiya, Z.,* 2007: Predictability of Sri Lankan rainfall based on ENSO. *Int. J. Climatol. 28*, 91–101. https://doi.org/10.1002/joc.1514

DOI:10.28974/idojaras.2023.1.3

IDŐJÁRÁS

Quarterly Journal of the Hungarian Meteorological Service
Vol. 127, No. 1, January – March, 2023, pp. 43–53

Possible environmental applications of a recently developed ammonia isotope monitoring photoacoustic system

Emily Awuor Ouma[1], **Helga Huszár**[1,2], **László Horváth**[1,2,*], **Gábor Szabó**[1], and **Zoltán Bozóki**[1,2]

[1]*Department of Optics and Quantum Electronics, University of Szeged, Dóm tér 9., H-6720 Szeged, Hungary*

[2]*ELKH-SZTE Research Group for Photoacoustic Monitoring of Environmental Processes, Dóm tér 9., H-6720 Szeged, Hungary*

**Corresponding author E-mail: horvathl@titan.physx.u-szeged.hu*

(Manuscript received in final form October 13, 2022)

Abstract— Ammonia is one of the most significant environmental pollutants. Concentration measurements, identifying the sources and studying the transformations in the biosphere are essential, and they are the focus of many investigations. The near-infrared (≈1530 nm) photoacoustic method for simultaneous and selective determination of $^{14}NH_3/^{15}NH_3$ isotopologues reported here can be suitable for monitoring these phenomena and processes. So far, the photoacoustic method has not been used for this kind of examination. The application of our measurement method makes it possible to eliminate the disadvantages of the previous measurement methods. The detection limit of the PA system is 0.14 ppm and 0.73 ppm for $^{14}NH_3$ and $^{15}NH_3$, respectively, which can be improved by orders of magnitude with further development of sampling and measurement techniques.

Key-words: atmospheric ammonia, isotopologues of ammonia, isotope abundance of $^{15}NH_3$, ammonia concertation, isotope tracer, isotope labelling, photoacoustic method for ammonia, near-infrared spectroscopy

1. Introduction

Nowadays, one of the most serious environmental risks is the accumulation of reactive nitrogen in different spheres of the Earth. Since the beginning of the last century, the *Haber-Bosch* ammonia synthesis converts a great amount of inert N_2 into NH_3 first of all for fertilizer production. The global NH_3 production is about 175 million tons per year and is expected to increase by 3–5% per year in the future (*Wang et al*., 2021). It is estimated that the efficiency of applied N is less than 50 and 70% under tropical conditions and temperate regions, respectively (*Baligar* and *Bennett*, 1986; *Malhli* and *Nyborg*, 1991; 1992; *Malhi et al*., 2001). Losses of N are mainly due to leaching, runoff, and volatile losses of ammonia. Further losses occur during harvesting, food processing, trading, and consumption. Finally, all the nitrogen content of fertilizers enters the environment, accumulating yearly in various spheres.

Circulation of anthropogenic nitrogen in Earth's atmosphere, hydrosphere, and biosphere has a wide variety of consequences, causing multiple effects in the atmosphere, in terrestrial ecosystems, in freshwater and marine systems, and on human health. This sequence of effects is called nitrogen cascade (*Galloway et al*., 2003). The harmful effects of reactive nitrogen can be traced in the deterioration of water quality (eutrophication), the impact on air quality (visibility, $PM_{2.5}$, smog), the reduction of biodiversity, the acidification of soil and groundwater, the increase of the greenhouse effect, and the decomposition of stratospheric ozone by N_2O.

Since ammonia plays a prominent role in the nitrogen cascade, the investigation of the atmospheric concentration and the exchange of NH_3 gas between the atmosphere and the surface has been among the main research goals of the last decades.

Investigation of the concentration ratio of stable ammonia isotopes ($^{14}NH_3$ and $^{15}NH_3$) is a good tool to monitor the exchange and transformation processes. There are two stable isotopes of nitrogen, ^{14}N and ^{15}N. Their molar ratio in atmospheric N_2 is 0.99636/0.00364, i.e., the volume ratio of ^{15}N is 0.3653%. The isotope abundance in the inert atmospheric N_2 is regarded as the standard in the calculation of isotope abundance of ^{15}N, however, this ratio changes due to the fractionation. All of the physical and chemical processes are accompanied by the change in the isotope abundance of $^{15}NH_3$. With the determination of the abundance of $^{15}NH_3$ ($\delta^{15}N\text{-}NH_3$) we can qualify and quantify the ammonia emission sources (*Bhattarai et al*., 2021; *Elliott et al*., 2019; *Felix et al.,* 2013;2017; *Wang et al*., 2022).

Isotope labelling is another frequently used method in environmental investigations. Since ^{15}N-enriched N compounds became commercially available in the 1970s, the number of applications of the stable isotope to study soil processes rapidly increased, taking advantage of the phenomenon that biological processes prefer the lighter ^{14}N isotope, i.e., the products of the processes contain

less ^{15}N, as before the processes (i.e., $\delta^{15}N$ decreases) (*Nômmik* et al., 1973; *Sánchez*, 2001; *Zhao et al*., 2016). The addition of a ^{15}N tracer to follow the catalytic reduction of nitric oxide to ammonia is also a frequently used method (*Ettireddi et al*., 2012; *Ozkan et al*., 1994).

There are several methods to determine the concentration of atmospheric ammonia. During the concentration measurement selectivity, sensibility, response time, and minimum detectable concentration are the most critical parameters. A general disadvantage of the measurement of ammonia gas is the adsorption on the surface of the sampling device or the walls of the sensor cell resulting in bias during the measurement. Some of the procedures are based on physical methods like spectroscopy (*Bobrutzky et al*., 2010; *Dang et al*., 2019; *Gall et al*., 1991; *Huszár et al*., 2008; *Pushkarsky et al*., 2002; *Schilt et al*., 2004), spectrometry (*Martin et al*., 2016; *Norman et al*., 2007; 2009; *Nowak et al*., 2006; 2007; *Vasileiou et al*., 2015a; 2015b; 2016), or fluorometry (*Amornthammarong et al*., 2011; *Kéruel* and *Aminot*, 1997). The chemical methods are mostly based on the transformation of ammonia gas into ammonium ion in the aquous phase, followed by the determination of ammonium (*Allegrini et al*., 1987; *ASTM*, 2015; *EMEP*, 1996; *Erisman et al*., 2001; *Jeong et al*., 2013; *Koroleff*, 1970; *Thomas et al*., 1973; 2002; *Rice et al*., 2012).

Separated simultaneous measurement of $^{14}NH_3$ and $^{15}NH_3$ isotopologues of ammonia gas can mostly be achieved by physical methods (*Phillips et al*., 2018; *Chang et al*., 2016; 2019; *Griffiths* and *de Haseth*, 2007; *Felix et al*., 2017; *Koletzko et al*., 1995; *Lee et al*., 2011; 2014; *Lehmann*, 2017; *Liu et al*., 2020; *McEnaney et al*., 2017; *Murakami et al*., 2005; *Nielander et al*., 2019; *Nômmik*, 1973; *Simonova* and *Kalashnikova*, 2019; *Taghizadeh-Toosi et al*., 2012; *Tonn et al*., 2019; *Wang et al*., 2017; *Wu et al*., 2019; *Zhao et al*., 2016).

So far, the employed analytical methods, especially in spectroscopy, are either very expensive, need large sensing volumes (NMR: Nuclear magnetic resonance method), have uncertainties at very low NH_3 concentrations (IRMS: isotope ratio mass spectroscopy), or are limited by the availability of the tunable laser light at the appropriate wavelength (CRDS: cavity ring-down spectroscopy), or simply have a problem in the control of its background signal (CIMS: chemical ionization mass spectroscopy).

Most of the analytical methods are not continuous, were done by active or passive sampling, and the evaluation is complicated. One exception is the method of *Phillips et al*. (2018) where the optical path length is of the order of 10 m through a generated plume making its application in the laboratory impossible.

To the best of the authors' knowledge, photoacoustic method has not been used for the simultaneous measurement of ammonia isotopes. The aim of our work has been to develop a simple, reliable, automatic, and robust system for the selective, rapid, and sensitive measurement of ammonia isotopes by using a near-infrared photoacoustic (NIR-PA) system.

Moreover, to achieve the above aim, there was a need for methodological development, construction of the measuring instruments, and finally, development of gas sampling procedures to be used. The following sub-aims were therefore carried out:

- Design and construction of a NIR-PA system capable of selectively measuring and differentiating between ammonia gas isotopes ($^{14}NH_3$ and $^{15}NH_3$).
- Selection and optimization of the measurement and modulation parameters (wavelength, laser operating temperature, etc.).
- Construction, testing, and calibration of the newly developed NIR-PA system.
- Solving the incidental problems and improvement of the system by re-optimization of the selected parameters.
- Evaluation of the developed NIR-PA system.

2. Experimental

2.1. Instrumentation set-up

The measurement system consisted of two main parts. A photoacoustic detection unit for concentration measurement, employing two types of diode lasers (an external cavity diode laser and a telecommunication type fiber coupled Near Infrared DFB diode laser), together with integrated electronics. The electronic's main purpose was to amplify, provide temporal averaging, filter the microphone signal, control the temperatures of the laser and the detection cell, and feed the modulated driving current to the diode laser.

The second part consisted of ammonia isotopes gas generating units which were of two types; NH_3 in N_2 cylinder (1000 ppm ± 1%, with a purity of 5.0) supplied by the Hungarian Messer company) and a chemical reaction-NH_3 generation-based mode. For more details, refer to *Ouma et al*. (2022).

2.2. Spectral measurements and analytical parameters

The $^{14}NH_3$ and $^{15}NH_3$ spectra were recorded using two DFB diode lasers separately, with the same modulation parameters as shown in *Fig. 1*. The wavelength modulation (WM) was used during the measurements due to its improved sensitivity and noise-rejection capabilities over amplitude modulation. The WM spectrum is a derivative form of the absorption spectrum.

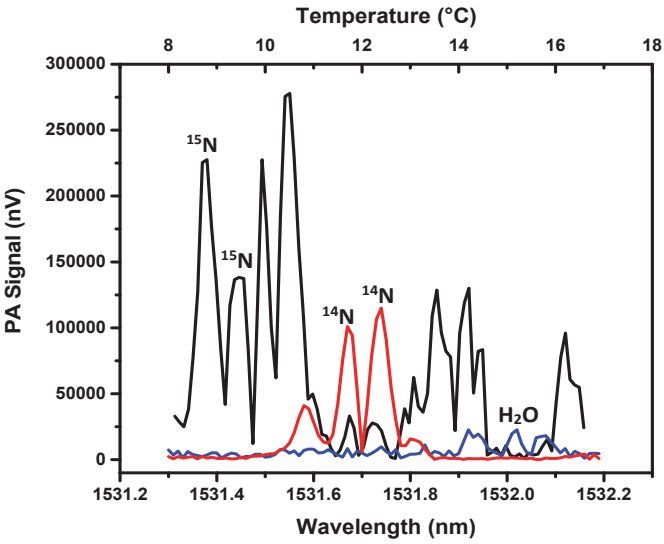

Fig 1. PA spectra of the ammonia isotopes; 600 ppm $^{15}NH_3$ (black line) and 95 ppm $^{14}NH_3$ (red line) as recorded by DFB diode laser. Cross-sensitivity spectrum of 5% water vapor (blue line) is also shown.

To minimize the cross-sensitivity and the disturbing effect of water vapor, four peak wavelengths, two for each isotope as shown in *Fig. 1*, were selected for the calibration measurements. Using two-two wavelengths for each isotope reduces the cross-sensitivity and increases the sensitivity of the method.

Calibration of the ammonia isotopes was then done using both the cylinders and the chemical reaction NH_3 generation methods. Measurement of the photoacoustic signal (PAS) in the function of volume mixing ratio (VMR) was performed in the range of 0–1000 ppm. The cross-sensitivity between the two isotopes measured simultaneously, calculated calibration lines, and the slope of the calibration line in nV/ppm which corresponded to the sensitivity of the NIR-PA system are all given in *Table 1*. For more technical details, refer to *Ouma et al*. (2022).

Table 1. Summary of the analytical parameters of the newly developed NIR-PA system (PAS: photoacoustic signal; VMR: volume mixing ratio)

Parameters	**Values obtained**
Modulation current (mA)	AC/DC: 10 /146
Modulation temperature (°C)	Laser 1: 18.10 °C and 18.69 °C for $^{14}NH_3$ 8.65 °C and 9.45 °C for $^{15}NH_3$ Laser 2: 20.95 °C and 21.56 °C for $^{14}NH_3$ 11.77 °C and 12.36 °C for $^{15}NH_3$
Measurement wavelengths (nm)	$^{14}NH_3$: 1531.66 and 1531.73 $^{15}NH_3$: 1531.37 and 1531.45
Cross-sensitivity (nV/ppm)	$^{14}NH_3$: -1.3×10^{-4} $^{15}NH_3$: 7.4×10^{-3}
Cross-sensitivity bias	$^{14}NH_3$: –0.002% $^{15}NH_3$: 0.57%
Calculated calibration lines	$^{14}NH_3$: *PAS* (μV) = 6.61×*VMR* (ppm) $^{15}NH_3$: *PAS* (μV) = 1.3×*VMR* (ppm)
Detection limit (ppm)	$^{14}NH_3$: 0.14 $^{15}NH_3$: 0.73
System response time (s)	3.5

3. Possible applications for atmospheric measurements

3.1. Application of ^{15}N as tracer during electrochemical ammonia synthesis

There is an alternative way for the high energy-intensive and CO_2 emitter *Haber-Bosch* ammonia synthesis, the electrocatalytic reduction of N_2 into ammonia (see e.g., *Qing et al*., 2020). This method, although still in the research and developmental stage, has shown great potential and is deemed less polluting and environmentally sustainable. While the process has produced promising results, several problems have been identified like its low efficiency (0.1–8%) and inaccuracy in the assessment of NH_3 levels produced. The latter problem is mostly due to the inability of the current NH_3 detecting equipment and analytical methods to reliably measure the low NH_3 gas produced (sub-ppm levels) without interference from common contaminants, such as human breath, laboratory air, contaminants in N_2 gas sources used in the synthesis process, etc.

3.2. Application of ^{15}N tracer in environmental analyses

There are lots of possible applications of the isotope tracer technique accompanied by photoacoustic detection, mostly in the investigation of soil biology and plant physiology processes. The nitrogen loss in form of ammonia can be estimated by the application of ^{15}N labeled fertilizer (e.g., *Nômmik*, 1973; *Zhao et al*., 2016).

The transformation of soil N, like denitrification or the N fixation by plants, can also be traced by this technique (*Sánches*, 2001).

3.3. Application in source apportionment of atmospheric ammonia

As it was mentioned in the introduction, the reference abundance of ^{15}N (0.3653%) is changing in each physical and chemical process of ammonia due to the fractionation. The change in abundance ($\delta^{15}NH_3$, ‰), i.e., the source signature is representative of the given physical and chemical process. Identifying the ammonia source (e.g., agricultural or fossil fuel combustion process, industry, heating, traffic) by nitrogen isotope helps in designing a mitigation strategy for policymakers, but the existing methods have not been well validated (*Pan et al*., 2020). The study of *Bhattarai et al*. (2020) highlights that collecting representative samples remains a challenge in fingerprinting $\delta^{15}N(NH_3)$ values of NH_3 emission sources, i.e., during the sampling, the isotope abundance changes compared to that of the representative for the given process. Since the application of PA systems does not need any sampling procedure the error caused by sampling and subsequent laboratory preparation can be avoided.

Because of the low abundance of $^{15}NH_3$, the source apportionment without the addition of a ^{15}N tracer requires a detection limit lower by orders of magnitude than it is reported in this paper. It can be achieved by the modification of the photoacoustic system described here by replacing the light source with a quantum cascade laser (QCL). Another possibility to improve the detection limit is the use of preconcentration sampling similarly to the method reported by *Pogány et al*. (2009).

4. Conclusion

This work has shown that measurement of ammonia isotopes ($^{14}NH_3$ and $^{15}NH_3$) using a photoacoustic measuring system fitted with a near-infrared diode laser light source around the wavelengths of 1532 nm is possible. Both NH_3 isotopes recorded strong absorption lines at this particular wavelength, while the values of their minimum detectable concentrations were 0.14 ppm for $^{14}NH_3$ and 0.73 ppm for $^{15}NH_3$. Due to the developed NIR-PA systems' robustness, high sensitivity, low cross-sensitivity, and short response time, it is expected to find a practical application in the detection and measurement of isotopically labeled NH_3 gas during the electrochemical synthesis process, as well as in the isotope tracer or source apportionment experiments.

Application of the photoacoustic method in these fields is a novelty and enables the elimination of the disadvantages of the previously used measurement techniques (high cost, complicated sampling, laboratory preparation, the error caused by sampling when measuring fractionalization, etc.). Fast response time is also an advantage in contrast to most of the previous measurement methods.

Acknowledgements: Emily Awuor Ouma wishes to acknowledge the Tempus Public Foundation for the award of the Stipendium Hungaricum Scholarship, which enabled and provided the platform to be able to carry out this research. This work was supported by the Hungarian Research and Technology Innovation Fund (OTKA), project no. K-138176, and the Sustainable Development and Technologies Programme of the Hungarian Academy of Sciences (FFT NP FTA).

References

Allegrini, I., De Santis, F., Di Palo, V., Febo, A., Perrino, C., Possanzini, M., and *Liberti, A.,* 1987: Annular denuder method for sampling reactive gases and aerosols in the atmosphere. *Sci. Tot. Environ. 67*, 1–16. https://doi.org/10.1016/0048-9697(87)90062-3

Amornthammarong, N., Zhang, J.Z., and *Ortner, P.B.*, 2011: An autonomous batch analyzer for the determination of trace ammonium in natural waters using fluorometric detection. *Anal. Methods. 3*, 1501–1506. https://doi.org/10.1039/c1ay05095h

ASTM, 2015: D1426-92 standard: test methods for ammonia nitrogen in water. Manual of water and environmental technology.

Baligar, V.C. and *Bennett, O.L.*, 1986: NPK-fertilizer efficiency. A situation analysis for the tropics. Fert. Res. 10, 147–164. https://doi.org/10.1007/BF01073907

Bhattarai, N., *Wang*, Sh., *Pan*, Y., *Xu*, Q., *Zhang*, Y., *Chang*, Y., and *Fang, Y.* 2021: δ^{15}N-stable isotope analysis of NH_x: An overview on analytical measurements, source sampling and its source apportionment. Frontiers of Environmental Science & Engineering 15, 126. https://doi.org/10.1007/s11783-021-1414-6

Bobrutzki, K., Braban, C F., Famulari, D., Jones, S. K., Blackall, T., Smith, T.E. L., Blom, M., Coe, H., Gallagher, M., Ghalaieny, M., McGillen, M. R., Percival, C.J., Whitehead, J.D., Ellis, R., Murphy, J., Mohácsi, A., Pogány, A., Junninen, H., Rantanen, S., Sutton, M. A., and *Nemitz, E.*, 2010: Field inter-comparison of eleven atmospheric ammonia measurement techniques. *Atmos. Meas. Tech. 3*, 91–112. https://doi.org/10.5194/amt-3-91-2010

Chang, Y., Liu, X., Deng, C., Dore, A.J., and *Zhuang, G.*, 2016: Source apportionment of atmospheric ammonia before, during, and after the 2014 APEC summit in Beijing using stable nitrogen isotope signatures. Atmospheric Chemistry and Physics 16, 11635–11647. https://doi.org/10.5194/acp-16-11635-2016

Chang, Y., Zou, Z., Zhang, Y., Deng, C., Hu, J., Shi, Z., Dore, A.J., and *Collett, J.L. Jr.*, 2019: Assessing contributions of agricultural and non-agricultural emissions to atmospheric ammonia in a Chinese megacity. Environmental Science and Technology *53*, 1822–1833. https://doi.org/10.1021/acs.est.8b05984

Dang, H., Ma, Y., Liu, F., and *Lu, J.*, 2019: Sensitive detection of ammonia based on quartz-enhanced photoacoustic spectroscopy. *J. Russian Leaser Res. 40*, 265–268. https://doi.org/10.1007/s10946-019-09800-9

Elliott, E.M., Yu, Z., Cole, A.S., and *Coughlin, J.G.*, 2019: Isotopic advances in understanding reactive nitrogen deposition and atmospheric processing. *Sci. Total Environ. 662*, 393–403. https://doi.org/10.1016/j.scitotenv.2018.12.177

EMEP/CCC-Report 1/95, 1996: Reference: O-7726 date: March 1996 Revision: November 2001 EMEP, Co-operative Programme for Monitoring and Evaluation of the Long-range Transmission of Air Pollutants in Europe. EMEP manual for sampling and chemical analysis.

Erisman, J.W., Otjes, R., Hensen, A., Jongejan, P., van den Bulk, P., Khlystov, A., Möls, H., and *Slanina, S.*, 2001: Instrument development and application in studies and monitoring of ambient ammonia. *Atmos. Environ. 35*, 1913–1922. https://doi.org/10.1016/S1352-2310(00)00544-6

Ettireddy, P.R., Ettireddy, N., Boningari, T., Pardemann, R., and *Smirniotis, P.G.* 2012: Investigation of the selective catalytic reduction of nitric oxide with ammonia over Mn/TiO_2 catalysts through transient isotopic labelling and in situ FT-IR studies. *J. Catalysis 292*, 53–63. https://doi.org/10.1016/j.jcat.2012.04.019

Felix, J.D., Elliot, E.M., and *Gay, D.*, 2017: Spatial and temporal patterns of nitrogen isotopic composition of ammonia at U.S. ammonia monitoring network sites. Atmos. Environ. 150, 434–442. https://doi.org/10.1016/j.atmosenv.2016.11.039

Felix, J.D., Elliot, E.M., Gish, T.J., McConnell, L.L. and *Shaw, S.L.*, 2013: Characterizing the isotopic composition of atmospheric ammonia emission sources using passive samplers and a combined oxidation-bacterial denitrifier approach. *Rapid Commun. Mass Spectromet. 27,* 2239–2246. https://doi.org/10.1002/rcm.6679

Gall, R., Perner, D., and *Ladstatter-Weissenmayer, A.*, 1991: Simultaneous determination of NH_3, SO_2, NO and NO_2 by direct UV absorption in ambient air. *Fresen, J. Anal. Chem. 340*, 646–649. https://doi.org/10.1007/BF00321528

Galloway, J.N., Aber, J.D., Erisman, J.W., Seitzinger, S.P., Howarth, R.W., Cowling, E.B. and Cosby, B.J., 2003: The nitrogen cascade. BioScience 53, 341356. https://doi.org/10.1641/0006-3568(2003)053[0341:TNC]2.0.CO;2

Griffiths, P.R. and *de Haseth, J.A.*, 2007: Fourier transform infrared spectrometry, John Wiley & Sons, Hoboken, New Jersey. https://doi.org/10.1002/047010631X

Huszár, H., Pogány, A., Bozóki, Z., Mohácsi, Á., Horváth, L., and *Szabó, G.*, 2008: Ammonia monitoring at ppb level using photoacoustic spectroscopy for environmental application. *Sens. Actuators B 134*, 1027–1033. https://doi.org/10.1016/j.snb.2008.05.013

Jeong, H., Park, J., and *Kim, H.*, 2013: Determination of NH_4^+ in environmental water with interfering substances using the modified Nessler method. *J. Chemistry,* Article ID 359217. https://doi.org/10.1155/2013/359217

Kéruel, R. and *Aminot, A.*, 1997: Flourometric determination of ammonia in sea and estuarine waters by direct segmented flow analysis. *Marine Chemistry 57*, 265–275. https://doi.org/10.1016/S0304-4203(97)00040-6

Koletzko, S., Haisch, M., Seeboth, I., Braden, B., Hengels, K., Koletzko, B., and *Hering, P.*, 1995: Isotope-selective non-dispersive infrared spectrometry for detection of Helicobacter pylori infection with ^{13}C-urea breath test ^{13}C-urea. *Lancet 345*, 961–962. https://doi.org/10.1016/S0140-6736(95)90704-1

Koroleff, F., 1970: Direct determination of ammonia in natural waters as indophenol blue. In: Information on Techniques and Methods for Seawater Analysis. Charlottenlund, Int. Counc. Explor. Sea (Interlab. Rept. 3). 19–22.

Lee, C., Feyereisen, G. W., Hristov, A. N., Dell, C. J., Kaye, J., and *Beegle, D*, 2014: Effects of dietary protein concentration on ammonia volatilization, nitrate leaching, and plant nitrogen uptake from dairy manure applied to lysimeters. *J. Environ. Quality 43*, 398–408. https://doi.org/10.2134/jeq2013.03.0083

Lee, C., Hristov, A.N., Cassidy, T., and *Heyler, K.*, 2011: Nitrogen isotope fractionation and origin of ammonia nitrogen volatilized from cattle manure in simulated storage. *Atmosphere 2*, 256–270. https://doi.org/10.3390/atmos2030256

Lehmann, W.D., 2017: A timeline of stable isotopes and mass spectrometry in the life sciences. *Mass Spectrom. Rev. 36,* 58–85. https://doi.org/10.1002/mas.21497

Liu, Y., Asset, T., Chen, Y., Murphy, E., Potma, E.O., Matanovic, I., Fishman, D.A., and *Atanassov, P.*, 2020: Facile all-optical method for in situ detection of low amounts of ammonia. *iScience 23*, 101757. https://doi.org/10.1016/j.isci.2020.101757

Malhi, S.S., Grant, C.A., Johnston, A.M., and *Gill K.S.*, 2001: Nitrogen fertilization management for no-till cereal production in the Canadian Great Plains: a review. *Soil Till. Res. 60*, 101–122. https://doi.org/10.1016/S0167-1987(01)00176-3

Malhi, S.S. and *Nyborg, M.*, 1991: Recovery of ^{15}N-labeled urea: influence of zero tillage, and time and method of application. *Fert. Res. 28*, 263–269. https://doi.org/10.1007/BF01054327

Malhi, S.S. and *Nyborg, M.*, 1992: Placement of urea fertilizer under zero and conventional tillage for barley. *Soil Till. Res. 23*, 193–197. https://doi.org/10.1016/0167-1987(92)90014-3

Martin, N.A., Ferracci, V., Cassidy, N., and *Hoffnagle, J.A.*, 2016: The application of a cavity ring-down spectrometer to measurements of ambient ammonia using traceable primary standard gas mixtures. *Appl. Phys. B 122*, 219. https://doi.org/10.1007/s00340-016-6486-9

McEnaney, J. M., Singh, A.R., Schwalbe, J. A., Kibsgaard, J., Lin, J.C., Cargnello, M., and *Jaramillo, T.F.*, 2017: Ammonia synthesis from N_2 and H_2O using a lithium cycling electrification strategy at atmospheric pressure. *Energy Environ. Sci. 10*, 1621–1630. https://doi.org/10.1039/C7EE01126A

Murakami, T., Nohira, T., Goto, T., Ogata, Y.H., and *Ito, Y.*, 2005: Electrolytic ammonia synthesis from water and nitrogen gas in molten salt under atmospheric pressure. *Electrochim. Acta. 50*, 5423–5426. https://doi.org/10.1016/j.electacta.2005.03.023

Nielander, A.C., Mcenaney, J.M., Schwalbe, J.A., Baker, J.G., Blair, S.J., Wang, L., Pelton, J.G., Andersen, S.Z., Enemark-Rasmussen, K., Čolić, V., Yang, S., Bent, S.F., Cargnello, M., Kibsgaard, J., Vesborg, P.C.K., Chorkendorff, I. and *Jaramillo, T.F.*, 2019: A versatile method for ammonia detection in a range of relevant electrolytes via direct nuclear magnetic resonance techniques. *ACS Catalysis 7*, 5797–5802. https://doi.org/10.1021/acscatal.9b00358

Nômmik, H. 1973: Assessment of volatilization loss of ammonia from surface-applied urea on forest soil by N^{15} recovery. *Plant Soil 38*, 589–603. https://doi.org/10.1007/BF00010699

Norman, M., Hansel, A., and *Wisthaler, A.*, 2007: O_2^+ as reagent ion in the PTR-MS instrument: detection of gas-phase ammonia. *Int. J. Mass. Spectrom. 265*, 382–287. https://doi.org/10.1016/j.ijms.2007.06.010

Norman, M., Spirig, C., Wolff, V., Trebs, I., Flechard, C., Wisthaler, A., Schnitzhofer, R., Hansel, A., and *Neftel, A.*, 2009: Inter-comparison of ammonia measurement techniques at an intensively managed grassland site (Oensingen, Switzerland). *Atmos. Chem. Phys. 9*, 2635–2645. https://doi.org/10.5194/acp-9-2635-2009

Nowak, J.B., Huey, L.G., Russell, A.G., Tian, D., Neuman, J.A., Orsini, D., Sjostedt, S.J., Sullivan, A.P., Tanner, D.J,. Weber, R.J., Nenes, A., Edgerton, E., and *Fehsenfeld, F.C.*, 2006. Analysis of urban gas phase ammonia measurements from the 2002 Atlanta Aerosol Nucleation and Real-Time Characterization Experiment (ANARChE). *J. Geophys. Res. 111*, D17308. https://doi.org/10.1029/2006JD007113

Nowak, J.B., Neuman, J. A., Kozai, K., Huey, L. G., Tanner, D. J., Holloway, J. S, Ryerson, T.B., Frost, G.J., McKeen, S.A., and *Fehsenfeld, F.C.*, 2007: A chemical ionization mass spectrometry technique for airborne measurements of ammonia. *J. Geophys. Res. Atmos. 112*, 1–12. https://doi.org/10.1029/2006JD007589

Ouma, E.A., Huszár, H., Horváth, L., Szabó, G., Janáky, C., and *Bozóki, Z.*, 2022: Development of a near-infrared photoacoustic system for selective, fast, and fully automatized detection of isotopically labelled ammonia. Anal. Chem. 94, 41, 14118–14125. https://doi.org/10.1021/acs.analchem.2c01191

Ozkan, U.S., Cai, Y. and *Kumthekar, M.W.*, 1994: Investigation of the reaction pathways in selective catalytic reduction of NO with NH_3 over V_2O_5 catalysts: isotopic labelling studies using $^{18}O^2$, $^{15}NH^3$, ^{15}NO, and $^{15}N^{18}O$. *J. Catalysis 149*, 390–403. https://doi.org/10.1006/jcat.1994.1306

Pan, Y., Gu, M., He, Y., Wu, D., Liu, Ch., Song, L., Tian, Sh., Lü, X., Sun, Y., Song, T., Walters, W.W., Liu, X., Martin, N.A., Zhang, Q., Fang, Y., Ferracci, V., and *Wang, Y.*, 2020: Revisiting the concentration observations and source apportionment of atmospheric ammonia. *Adv. Atmos. Sci., 37*, 933−938. https://doi.org/10.1007/s00376-020-2111-2

Phillips, M.C., Brumfield, B.E., and *Harilal, S.S.*, 2018: Real-time standoff detection of nitrogen isotopes in ammonia plumes using a swept external cavity quantum cascade laser. *Opt. Lett. 43*, 4065–4068. https://doi.org/10.1364/OL.43.004065

Pogány, A., Mohácsi, Á., Varga, A., Bozóki, Z., Galbács, Z., Horváth, L., and *Szabó, G.*, 2009: A compact ammonia detector with sub-ppb accuracy using near-infrared photoacoustic spectroscopy and preconcentration sampling. *Environ. Sci. Technol. 43*, 826−830. https://doi.org/10.1021/es802638z

Pushkarsky, M.B., Webber, M.E., Baghdassarian, O., Narasimhan, L.R., and *Patel, C.K.N*, 2002: Laser-based photoacoustic ammonia sensors for industrial applications. *Appl. Phys. B 75*, 391–396. https://doi.org/10.1007/s00340-002-0967-8

Qing, G., Ghazfar, R., Jackowski, S. T., Habibzadeh, F., Ashtiani, M. M., Chen, C.-P., Smith, M.R. III, and *Hamann, T.W.*, 2020: Recent advances and challenges of electrocatalytic N_2 reduction to ammonia. *Chem. Rev. 120*, 5437−5516. https://doi.org/10.1021/acs.chemrev.9b00659

Rice, E., Baird, R., Eaton, A., and *Clesceri, L.*, 2012: Standard methods for the examination of water and wastewater. American Public Health Association, American Water Works Association, Water Environment Federation.

Sánchez, C.C., 2001: Stable nitrogen isotopes. Study about its use in the assessment of denitrification and N fixation. Plant Research International B.V., Wageningen, Note 145. Wageningen UR.

Schilt, S., Thévenaz, L., Niklès, M., Emmenegger, L., and *Hüglin, Ch*., 2004: Ammonia monitoring at trace level using photoacoustic spectroscopy in industrial and environmental applications. *Spectrochimica Acta Part A 60*, 3259–3268. https://doi.org/10.1016/j.saa.2003.11.032

Simonova, G. and *Kalashnikova, D*., 2019: Isotope ratio mass spectrometry application for environmental investigations. E3S Web Conferences 98, 12020. https://doi.org/10.1051/e3sconf/20199812020

Taghizadeh-Toosi, Gough, T.J., Sherlock, R.R., and *Condron, L.M*., 2012: Biochar adsorbed ammonia is bioavailable. *Plant and Soil 350*, 57–69. https://doi.org/10.1007/s11104-011-0870-3

Thomas, R.F. and *Booth, R.L.*, 1973: Selective electrode measurement of ammonia in water and wastes. *Environ. Sci. Technol. 7*, 523–526. https://doi.org/10.1021/es60078a006

Thomas, D.H., Rey, M., and *Jackson, P.E.*, 2002: Determination of inorganic cations and ammonium in environmental waters by ion chromatography with a high-capacity cation-exchange column. *J. Chromatogr. A. 956*, 181–186. https://doi.org/10.1016/S0021-9673(02)00141-3

Tonn, B., Porath, I., Lattanzi, F.A, and *Isselstein, J*., 2019: Urine effects on grass and legume nitrogen isotopic composition: Pronounced short-term dynamics of $\delta^{15}N$. PLoS ONE 14, e0210623. https://doi.org/10.1371/journal.pone.0210623

Vasileiou, E., Kyriakou, V., Garagounis, I., Vourros, A., and *Stoukides, M*., 2015a: Ammonia synthesis at atmospheric pressure in a $BaCe_{0.2}Zr_{0.7}Y_{0.1}O_{2.9}$ solid electrolyte cell. *Solid State Ionics. 275*, 110–116. https://doi.org/10.1016/j.ssi.2015.01.002

Vasileiou, E., Kyriakou, V., Garagounis, I., Vourros, A., Manerbino, A., Coors, W.G., and *Stoukides, M., 2015b*: Reaction rate enhancement during the electrocatalytic synthesis of ammonia in a BaZr0.7Ce0.2Y0.1O2.9 solid electrolyte cell. *Top. Catal. 58*, 1193–1201. https://doi.org/10.1007/s11244-015-0491-9

Vasileiou, E., Kyriakou, V., Garagounis, I., Vourros, A., Manerbino, A., Coors, W. G., and *Stoukides, M.*, 2016: Electrochemical enhancement of ammonia synthesis in a $BaZr_{0.7}Ce_{0.2}Y_{0.1}O_{2.9}$ solid electrolyte cell. *Solid State Ionics. 288*, 357–362. https://doi.org/10.1016/j.ssi.2015.12.022

Wang C., Li X., Zhang T., Tang A., Cui M., Liu X., Ma X., Zhang Y., Liu X. and *Zheng M*., 2022: Developing Nitrogen Isotopic Source Profiles of Atmospheric Ammonia for Source Apportionment of Ammonia in Urban Beijing. *Front. Environ. Sci. 10*, 903013. https://doi.org/10.3389/fenvs.2022.903013

Wang, M., Khan, M.A., Mohsin, I., Wicks, J., Ip, A.H., Sumon, K.Z., Dinh, C.-T., Sargent, E.H., Gates, I.D., and *Kibria, M.G*., 2021: Can sustainable ammonia synthesis pathways compete with fossil-fuel based Haber–Bosch processes? *Energy Environ. Sci. 14*, 2535. https://doi.org/10.1039/D0EE03808C

Wang, Z., Wang, Q., Ching, J.Y., Wu, J.C., Zhang, G., and *Ren, W*., 2017: A portable low-power QEPAS-based CO_2 isotope sensor using a fiber-coupled interband cascade laser. *Sensors Actuators B. Chem. 246*, 710–715. https://doi.org/10.1016/j.snb.2017.02.133

Wu, S-P., Zhu, H., Liu, Z., Dai, L-H., Zhang, N., Schwab, J.J., Yuan, C-S., and *Yan, J-P*., 2019: Nitrogen isotope composition of ammonium in $PM_{2.5}$ in the Xiamen, China: impact of non-agricultural ammonia. Environmental *Sci. Pollut. Res. 26*, 25596–25608. https://doi.org/10.1007/s11356-019-05813-8

Zhao, X., Yan, X., Xie, Y., Wang, S., Xing, G., and *Zhu, Z*., 2016: Use of nitrogen isotope to determine fertilizer- and soil-derived ammonia volatilization in a rice/wheat rotation system. *Agric. Food Chem. 64*, 3017–3024. https://doi.org/10.1021/acs.jafc.5b05898

DOI:10.28974/idojaras.2023.1.4

IDŐJÁRÁS

Quarterly Journal of the Hungarian Meteorological Service
Vol. 127, No. 1, January – March, 2023, pp. 55–76

A novel ensemble wind speed forecasting method using the differential weighting scheme and principal component analysis

Laleh Parviz

Faculty of Agriculture
Azarbaijan Shahid Madani University
35 Km Tabriz- Maragheh Road,
Tabriz, Iran P.O.B: 53714-161

Corresponding author E-mail: laleh_parviz@yahoo.com

(Manuscript received in final form April 6, 2022)

Abstract— Wind speed forecasting has found economic significance as it can increase operational efficiency. In this regard, an accurate forecast of wind speed is crucial in the application of wind resources. This study is intended to incorporate independent and output variables as the input of support vector regression (SVR) to forecast wind speed of Zanjan and Ahvaz stations in Iran. The independent variables were minimum, maximum, and mean temperatures, relative humidity, precipitation, average visibility, and dew point temperature. The incorporation of independent and output variables were conducted with principal component analysis (PCA) and differential weighting scheme (DWS), respectively. DWS combined the forecasts of linear regression, SVR, and group method of data handling (GMDH) in which the SVR showed the best The forecast of DWS outperformed the other three mentioned models. The incorporation of DWS and PCA (DWS-PCA) improved the forecasts and the capability of DWS-PCA as a novel method was significant in terms of forecast stability. The novel method can be a robust approach for wind speed forecasting in some subjects such as renewable energy, and meteorological decisions.

Key-words: wind speed forecasting, incorporation, differential weighting scheme, principal component analysis

1. Introduction

Weather forecasting plays an essential role in our daily life as increasing losses are reported every day due to extreme weather events. Timely weather warnings such as high wind warning can protect many lives (*Pan et al*., 2021). Wind forecasting is an important issue in hydrological and meteorological decisions. Accurate wind speed forecasting is necessary for the stable function of wind turbines to generate wind power. Wind power can be effectively managed through wind speed monitoring. Furthermore, renewable and non-polluting energy sources have recently found increasing popularity due to global warming effects. Wind energy can be one of the fundamental components of green energy sources. The appropriate operation of wind turbines and the optimal power generation can be achieved considering wind speed as an essential element. The difficulty in wind forecasting can be assigned to the periodic nature of wind speed (*Jaseena* and *Kovoor*, 2021) making the development of an accurate wind forecasting method a challenging task. Physical, statistical, and hybrid approaches can be exploited in wind speed forecasting. Physical models use mathematical concepts with historical data to forecast wind speed. The historical time series can help to forecast future data by statistical models. Hybrid models are composed of two or more forecasting models with their performance which can outperform single models (*Jaseena* and *Kovoor,* 2021).

Wind speed was predicted with generalized regression neural network (GRNN) and multi-layer precipitation (MLP) in some regions of India, considering longitude, latitude, daily horizontal solar irradiance, relative humidity, air temperature, elevation, earth temperature, cooling degree-days, heating degree-days, and atmospheric pressure as the input variables. The accuracy of GRNN was higher than that of MLP (*Kumar* and *Malik,* 2016). Four artificial intelligence methods including artificial neural networks (ANN) with radial basis function, adaptive neuro-fuzzy inference system, ANN with a genetic algorithm, and ANN with particle swarm optimization (PSO) were used for wind speed forecasting. The minimum root mean square error (RMSE) was related to ANN-PSO for Tehran, Iran (*Fazelpour et al.,* 2016). The multilayer feed-forward neural network (MLFFNN), support vector regression (SVR) with radial basis function, and adaptive neuro-fuzzy inference system (ANFIS) were employed to predict wind speed and direction in Bushehr. The input variables were temperature, pressure, local time, and relative humidity. ANFIS was optimized with the PSO method (ANFIS-PSO). The evaluation indices showed that the SVR model outperformed the MLFFNN and ANFIS-PSO models (*Khosravi et al*., 2018). Another study in association with wind speed prediction is a comparative analysis of ANN and chaotic time series forecasting. The results indicated that the neural network approaches outperformed the chaotic model (*Jamil* and *Zeeshan,* 2019). A multi-variate

long short-term memory (MV-LSTM) network was also proposed for short-term forecasting of wind speed considering meteorological variables of temperature, humidity, and air pressure. The superiority of MV-LSTM to ARMA was proved for short-term forecasting of wind speed (*Xie et al.,* 2021). In addition, hybrid models were also proposed to forecast wind speed. Two hybrid models consisting of neural network and neuro-fuzzy models combined with wavelet were introduced for monthly wind forecasting in Yazd (Iran) considering variables such as wind speed, maximum temperature, mean temperature, evaporation, and relative humidity. The results showed the high performance of the wavelet neural-fuzzy method (*Afkhami et al.,* 2015).

The decomposition-based hybrid deep BiDLSTM (Bidirectional Long Short Term Memory) models with skip connection were proposed by *Jaseena* and *Kovoor* (2021) which showed superior performance in terms of wind speed forecasting. The hybrid machine intelligence using variants of SVR (ε-SVR, LS-SVR, ε-twin support vector regression (ε-TSVR), twin support vector regression (TSVR)) was employed for wind forecasting in four wind farm sites. The ε-TSVR outperformed the other models (*Dhiman et al*., 2019). Another hybrid model was based on data division and a deep learning network for efficient short-term wind speed prediction. This system could improve the accuracy of forecasts relative to the other conventional methods (*Liu et al*., 2021). Generally, the combined forecasting approaches outperform the single models and can be a good choice for wind speed forecasting. In the combination approaches, the information can be derived from the single models through a precise method with high forecasting performance in various fields. For instance, a multi-granularity heterogeneous combination method was employed for forecasting crude oil (*Wang et al*., 2020). Moreover, different combination methods such as mean, linear regression, nonlinear regression with machine learning algorithm were adopted to forecast day-ahead solar power (*Dewangan et al.,* 2020), or different weight combination methods such as inverse variance method and simple weight average method were used for air quality forecasting (*Song* and *Fu*, 2020). Along with the combination of dependent variables (named as forecast combination), there is another method with emphasis on the combination of independent variables. The method with increased forecasting accuracy uses principal component analysis (PCA) as model inputs rather than original variables (*UI-Saufie et al*., 2011).

The present study is thus aimed at the development of a novel approach for monthly wind speed forecasting. In this regard, an ensemble of independent and output variables was carried out with the PCA and the forecast combination method (DWS), respectively. The forecast combination method combined the results of linear regression, SVR, and group method of data handling (GMDH) models. The input of single models was meteorological variables such as temperature.

2. Material and Methods

2.1. Case study

Data observed at Ahvaz and Zanjan meteorological stations in Iran were used in this study. The studied provinces are Khuzestan and Zanjan (*Fig 1.a)* and the location of stations is shown in *Figs. 1d* and *e*. The studied period was from 2008 to 2020 during which the selected calibration period was from 2008 to 2016. The monthly times series of wind speed are presented in *Figs. 1b* and *f*. The average wind speeds for the study period in Ahvaz and Zanjan stations are 8.12 and 11.8 km/h, respectively. The climate of Ahvaz and Zanjan stations can be classified as arid and semi-arid based on the De Martonne's climate classification (*De Martonne*, 1925). To investigate the monthly temperature and precipitation variations, the embrothermic diagram of each station was drawn in *Figs. 1c* and *g* as reported by *Emberger et al*. (1963). In the embrothermic diagram of Ahvaz station, except for two months (November and December), the temperature was higher than the precipitation, suggesting the arid climate of Ahvaz. In Zanjan station, the points with higher precipitation compared to temperature were equal to those whose temperature was higher than the precipitation.

The forecast combination approach is focused on the integration of competing forecasts considering the superiority of individual forecasts of the models (*Wang et al*., 2020). Regarding the strong effect of forecast combination methods on forecasting issues, in this study, the incorporation of input or independent variables and output or dependent variables were conducted. PCA was used for input variables combination. To combine output variables or forecasted data from some models, DWS was also utilized using wind speed forecasting models such as linear regression (LR), GMDH, and SVR. The incorporation of PCA and DWS was finally conducted by SVR (PCA-DWS). *Fig. 2* shows the steps related to the performance of the novel method.

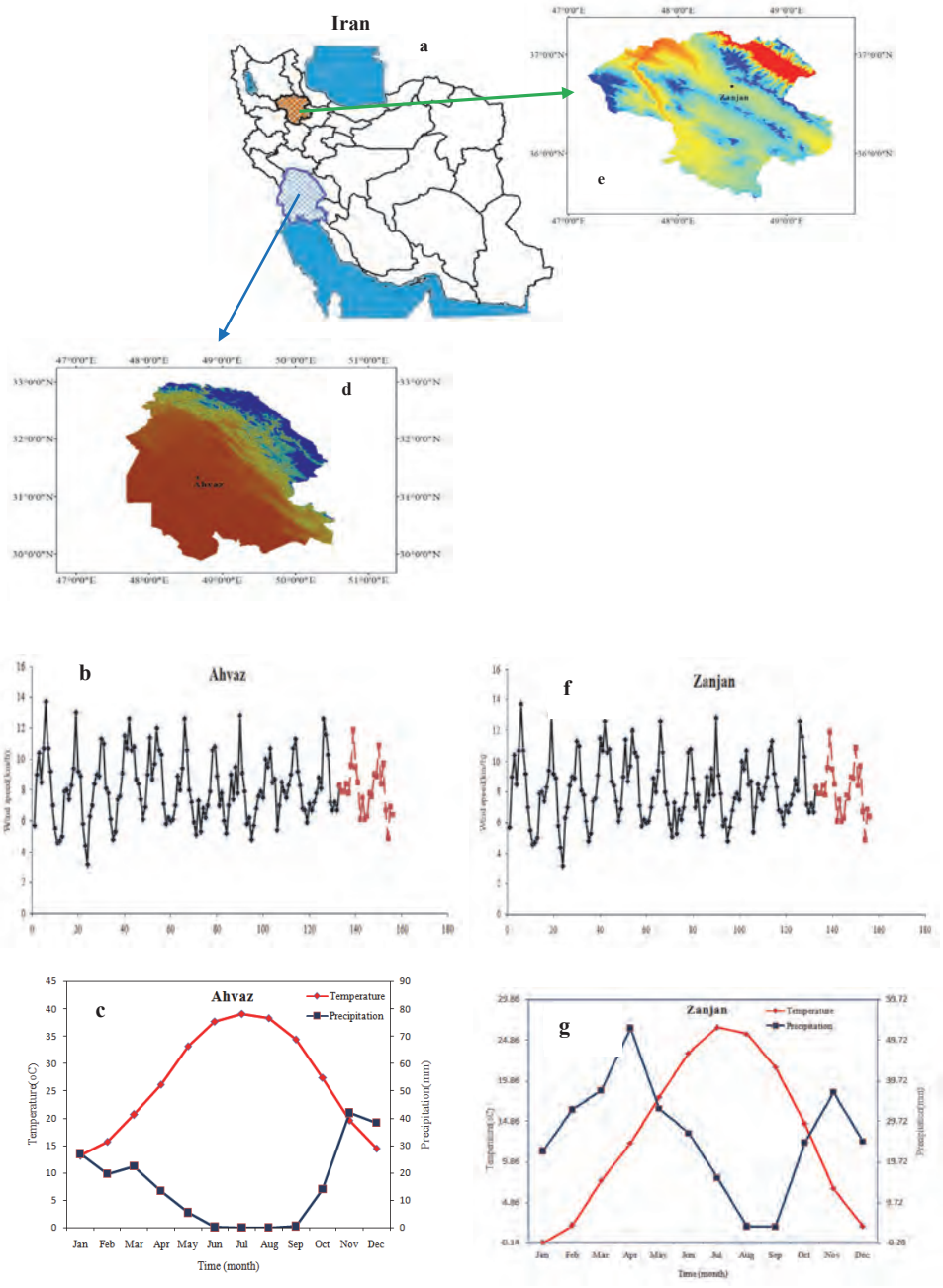

Fig. 1. Map of Iran (a), monthly time series of wind speed for Ahvaz (b) and Zanjan (f) stations during 2008–2020, embrothermic diagram of Ahvaz (c) and Zanjan (g) stations, location of Ahvaz (d) and Zanjan (e) stations in Khuzestan and Zanjan provinces.

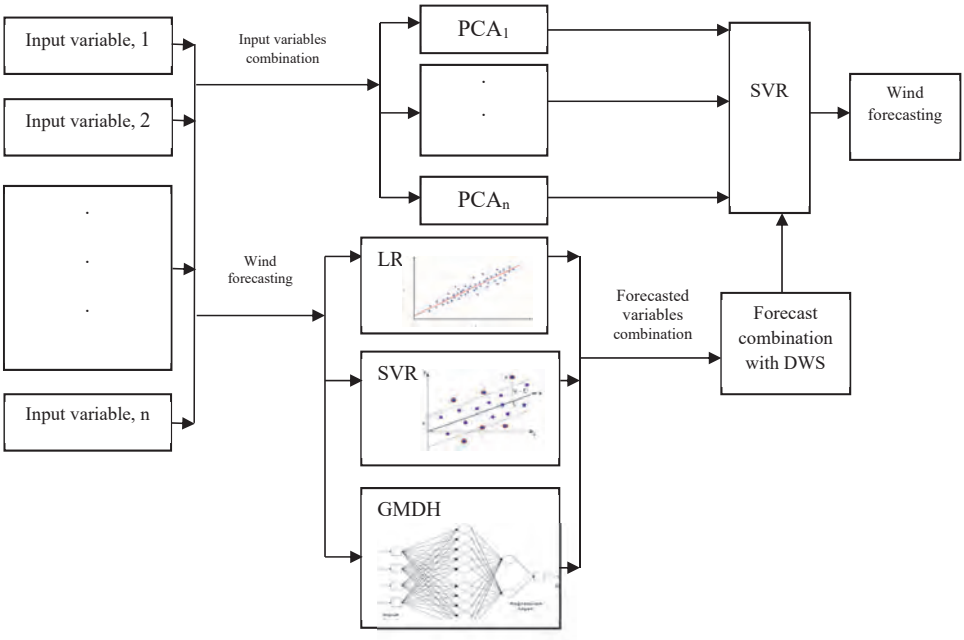

Fig. 2. Different stages of the proposed method performance.

2.2. Principal component analysis (PCA)

PCA can be defined as a linear combination of original variables and the weights assigned to the linear combination of the original variables also known as eigenvectors (*Wang* and *Wang*, 2015). In *Fig. 2,* all components were not used; only components with eigenvalues more than 1 were selected. The performance of PCA as a reduction method can be also described: *M* can be considered a *t*-dimensional data set. The retained variance is maximal orthonormal onto principal axes of G_1, G_2,…, G_N in the projected space. G_1, G_2,…, G_N are obtained with *n* leading eigenvectors of sample covariance

$$matrixC = \left(\frac{1}{L}\right)\sum_{k=1}^{L}(x_k - m)^T(x_k - m) \quad , \tag{1}$$

where *m* is the samples average and *L* is the samples number (*Avci* and *Turkoglu,* 2009).

PCA can discover and reduce the dimensionality of data by their clustering (*Wang* and *Wang*, 2015), and it can also identify and observe the source of variation (*UI-Saufie et al*., 2013).

2.3. Support vector regression (SVR)

Relying on statistical learning or Vapnik-Chervonenkis theory, support vector machines (SVMs) have found applications in yet-to-be-seen data. The generalization of the classification problem can be regarded as a regression problem. In this case, the output of the model is a continuous value. Therefore, the performance of the regression model relies on continuous-valued multivariate function estimation. The classification problems can be solved by the convex optimization problems using SVMs (*Vapnik*, 1998). The optimization problem tries to find the maximum margin separation of the hyperplane. In SVM, the optimal hyperplane can be represented by support vectors. Generalization of SVM to SVR can be achieved by introducing the ε-insensitive region around the function also known as the ε-tube. The construction of SVR with the ε-insensitive loss function was proposed by *Vapnik* (1998).

The form of a linear function *f(x)* can be written as

$$f(x) = \langle \omega, x \rangle + b, \tag{2}$$

where *b* is the bias.

The problem could be considered a convex optimization problem. The optimization structure encompasses a regularization parameter, which affects the tradeoff between the approximation error and the weight vector norm. The optimization problem could be changed into a dual problem using Lagrange multipliers with a kernel function. Kernel functions have diverse types including linear, polynomial, Gaussian radial basis function (RBF), and sigmoid as presented (*Acosta et al*., 2022) in the following:

$$k(x_n, x) = x_n^T x\ , \tag{3}$$

$$k(x_n, x) = (\gamma x_n^T x + u)^d\ , \tag{4}$$

$$k(x_n, x) = exp(-\frac{1}{2r^2}\|x_n - x\|^2 = exp(-\gamma\|x_n - x\|^2)\ , \tag{5}$$

$$k(x_n, x) = tanh(\gamma x_n^T x + u), \tag{6}$$

where d is the degree of the polynomial and r defines the width of kernel, $\gamma = \frac{1}{2}r^2 and r > 0$.

2.4. Group method of data handling (GMDH)

The structure of GMDH consists of neurons that could be linked by the quadratic polynomial, giving rise to new neurons in the next layer. This model is aimed to minimize the squared of the differences between the forecasted and observed data:

$$\sum_{i=1}^{M}[\hat{f}(x_{i1}, x_{i2}, \ldots, x_{in}) - y_i]^2 \rightarrow min \quad (7)$$

The complex discrete form of the Volterra functional series can be used to state all connections between the input and output data defined as the Kolmogorov-Gabor polynomial:

$$y = a_0 + \sum_1^n a_i x_i + \sum_1^n \sum_1^n a_{ij} x_i x_j + \sum_1^n \sum_1^n \sum_1^n a_{ijk} x_i x_j x_k + \quad (8)$$

The coefficient of the polynomial can be found with the regression method which minimizes the difference between observed and estimated values (*Razzaghi et al.*, 2021).

2.5. Forecasts combination

In the linear mode of the combination methods, the combination of forecasts can be calculated with the linear function of the contributing individual forecasts from individual models. The importance of individual models can be determined by assigning nonnegative and unbiased weights:

$$\hat{y}_k = w_1 \hat{y}_k^{(1)} + w_2 \hat{y}_k^{(2)} + \ldots + w_n \hat{y}_k^{(n)}, \quad (9)$$

where *w* is the weights of single models and *n* is the number of single models (*Adhikari* and *Agrawal*, 2014).

The error-based methods (*Armstrong*, 2001), the least square regression (*Frietas* and *Rodrigues*, 2006), and the differential weighting scheme (DWS) of *Newbold* and *Granger* (1974) are among the forecast combination methods the differential weighting method is selected from in this study. The minimization of the combined forecast error variance is one of the approaches in the determination of the weights of forecast combinations. *Newbold* and *Granger* (1974) proposed five differential weighting schemes. Two of them have exhibited excellent performance (*Winkler* and *Maridais*, 1983) as presented in the following formulas:

$$w_i = (\sum_{s=t-v}^{t-1}(e_s^{(i)})^2)^{-1} / \sum_{j=1}^{n}(\sum_{s=t-v}^{t-1}(e_s^{(j)})^2)^{-1}, DWS - I \quad (10)$$

$$w_{i,t} = \beta w_{i,t} + (1-\beta)[\sum_{s=t-v}^{t-1}(e_s^{(i)})^2)^{-1} / \sum_{j=1}^{n}(\sum_{s=t-v}^{t-1}(e_s^{(j)})^2)^{-1}], DWS - II, \quad (11)$$

where *n* is the number of single models, *t* is the forecasted time period, $w_{i,t-1}$ is the weight of the *i*th model using the data of preceding period, *v* and β are constant parameters, where β is between 0 and 1, and e_t is the percentage forecast error (*Winkler* and *Makridakis*, 1983).

2.6. *Evaluation metrics*

Two classes of metrics were used to evaluate the wind speed forecasting performance of the novel method (PCA-DWS). Metrics which investigate the accuracy of forecasts are listed in *Table 1*, where O_i and F_i (i=1,…,N) are the observed and forecasted time series, respectively, while O_{max} and O_{min} are the maximum and minimum values of the observed time series. The following metric explores the stability of forecasting:

$$DIS = \sqrt{\frac{\sum_{i=1}^{N}(e_i - (\frac{\sum_{i=1}^{N} e_i}{N}))^2}{N}}, \tag{12}$$

where e_i is the difference between observed and forecasted data.

Table 1. The evaluation metrics for investigation the accuracy of forecast.

AMAPE	Adopted mean absolute percent error	$AMAPE = \frac{1}{N}\sum_{i=1}^{N}(\frac{\lvert F_i - O_i\rvert}{\frac{1}{N}\sum_{i=1}^{N} O_i}) \times 100\ \%$
RMSE	Root mean square error	$RMSE = \sqrt{\frac{1}{N}\sum_{i-1}^{N}(F_i - O_i)^2}$
RRMSE	Relative root mean square error	$RRMSE = \frac{RMSE}{\overline{O}}$
NRMSE	Normalized root mean square error	$NRMSE = \frac{RMSE}{O_{\max} - O_{\min}}$
MAE	Mean absolute error	$MAE = \frac{1}{N}\sum_{i-1}^{N}\lvert O_i - F_i\rvert$
AE	Average error	$AE = \frac{1}{N}\sum_{i=1}^{N}(F_i - O_i)$
TIC	Thiel inequity coefficient	$TIC = \frac{\sqrt{\frac{1}{N}\sum_{i-1}^{N}(F_i - O_i)^2}}{\sqrt{\frac{1}{N}\sum_{i-1}^{N}(O_i)^2} + \sqrt{\frac{1}{N}\sum_{i-1}^{N}(F_i)^2}}$
VAF	Values of account for	$VAF = \left[1 - \frac{\mathrm{var}(O_i - F_i)}{\mathrm{var}(O)}\right]$
NSE	Nash –Sutcliffe coefficient	$NSE = 1 - \frac{\sum_{i=1}^{N}(F_i - O_i)^2}{\sum_{i=1}^{N}(O_i - \overline{O})^2}$

Better forecasting performance can be obtained with lower values of RMSE, DIS, AMAPE, MAE, TIC, RRMSE, and NRMSE. The values of NSE close to 1 indicate the perfect fit. The higher values of VAF are indicative of forecast improvement (*Wang et al.,* 2021a*; Luo et al*., 2021*; Temeng et al.,* 2020; *Dhiman et al.,* 2019; *Yang et al.,* 2020; *Minaeian* and *Ahangari,* 2013).

In addition to the mentioned criteria, some improvement percentage indicators such as PRMSE were employed to compare the performance of different models. PRMS is defined in as

$$PRMSE = \left|\frac{RMSE_1 - RMSE_2}{RMSE_2}\right| \times 100\% , \quad (13)$$

where $RMSE_1$is the RMSE of the first model, $RMSE_2$is the RMSE of the second model (*Liu et al.,* 2021).

3. Results

Minimum, maximum, and mean temperatures, relative humidity, precipitation, average visibility, and dew point temperature were regarded as independent variables for monthly wind forecasting through linear regression, GMDH, and SVR models. Evaluation of the assimilation of forecast combination scheme and PCA was conducted from 2019 to 2020. The correlation coefficients of wind speed with the mentioned variables are listed in *Table 2*. According to *Table 2*, the maximum correlation coefficient of meteorological variables and wind speed in Zanjan and Ahvaz was that of mean temperature and relative humidity. The significant correlation coefficients in the Ahvaz station are mean, maximum, and minimum temperatures, relative humidity, and precipitation. In Zanjan station, these significant correlation coefficients include mean, maximum, and minimum temperatures, relative humidity, and dew point.

Table 2. Correlation coefficients of meteorological variables and wind speed.

meteorological variables	stations	
	Zanjan	Ahvaz
Mean temperature	0.427**	0.623**
Maximum temperature	0.398**	0.597**
Minimum temperature	0.425**	0.619**
Relative humidity	-0.459**	-0.176*
Precipitation	-0.112	-0.386**
Average visibility	0.034	-0.031
Dew point temperature	0.338**	0.017

*. Correlation is significant at the 0.05 level (2-tailed)
**. Correlation is significant at the 0.01 level (2-tailed)

Therefore, temperature and relative humidity can be regarded as effective variables on wind speed. The average correlation coefficient of temperature (maximum, minimum, and mean) with wind speed in Ahvaz is higher than in Zanjan. The first step of the developed method is to use linear regression, ε-SVR, and GMDH (regarded as single models) to model the relationship between meteorological variables and wind speed. The parameters of SVR and GMDH are listed in *Table 3*.

Table 3. Parameters of single models for wind forecasting

Model	Name of parameter	station	
		Zanjan	**Ahvaz**
GMDH	Maximum number of neurons in a layer	9	5
	Maximum number of layers	2	2
	Selection pressure	0.9	0.9
SVR	Kernel function	Linear function	Gaussian radial basis function
	Regularization parameter, C	0.25	0.25

The sensitivity analysis is one of the most important steps in the modeling process. The MAE decreasing of SVR from sigmoid to linear kernel function (C=0.25) was 55.83% in Zanjan. The variation of maximum number of neurons per layer from 5 to 9 decreased MAE by 35.09% in Ahvaz. After sensitivity analysis of models, the wind forecasting performance of three models was investigated with some evolution metrics as shown in *Fig. 3*.

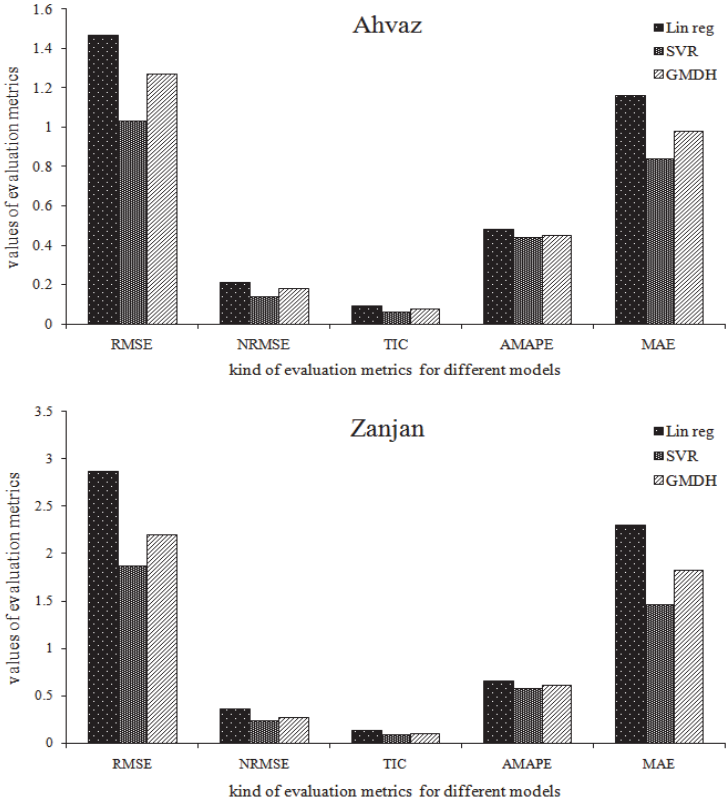

Fig. 3. Evaluation of the performance of three models, linear regression (Lin reg), SVR, and GMDH regarding to wind forecasting with some evaluation metrics in the two stations.

Evaluation metrics in *Fig. 3* are improved upon using SVR compared to the other models. In Ahvaz station, the RMSE, NRMSE, TIC, AMAPE, and MAE decrease from linear regression to SVR was 29.38%, 18.26%, 33.33%, 22.22%, and 30%, respectively. The amount of decline in the same parameters from GMDH to SVR was 18.18%, 8.33%, 2.22%, 27.58%, and 14.28%, respectively. The decrement in RMSE, NRMSE, TIC, AMAPE, and MAE from GMDH to SVR in Zanjan was 15%, 14.81%, 11.57%, 4.91%, and 20.21%, respectively. The average decrease in RMSE, NRMSE, TIC, AMAPE, and MAE in Ahvaz and Zanjan was 15.032% and 13.3%, respectively. The TIC decrement (average for two stations) from linear regression and GMDH to SVR was 32.69% and 14.87%, respectively, reflecting the better performance of SVR and GMDH relative to

linear regression. The AE values of the two stations related to SVR were positive, suggesting forecast overestimation. The obtained forecasts from three models were combined with two methods (DWS-I and DWSII), and the combined forecasts methods (DWS-I) were compared with the best model among the three models as illustrated in *Fig. 4*.

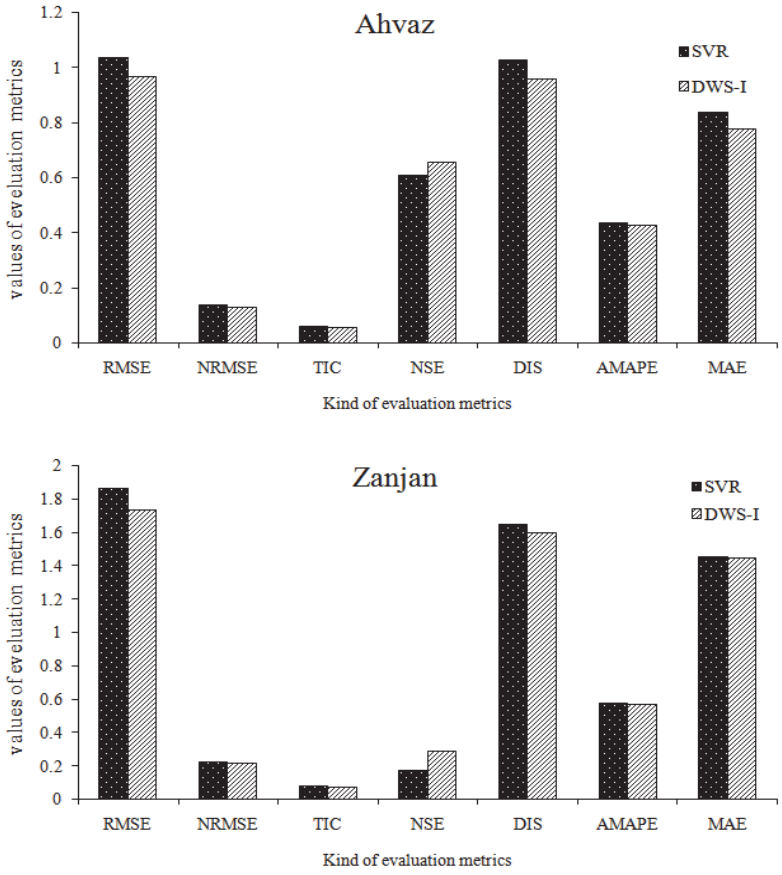

Fig. 4. Evaluation metrics related to SVR and DWS-I performances in the two stations.

DWS method outperformed the SVR, GMDH, and linear regression models, based on *Fig. 4*. The decrease in RMSE, NRMSE, and TIC from SVR to DWS was 6.45%, 7.14%, and 6.34% in Ahvaz and 6.95%, 4.34%, and 5.95% in Zanjan,

respectively. The RMSE, NRMSE, TIC, and DIS decrement (average of two stations) from SVR to DWS was 6.7%, 5.74%, 6.14%, and 4.91%, respectively. The average reduction in RMSE, NRMSE, TIC, DIS, AMAPE, and MAE from SVR to DWSI-I for Ahvaz and Zanjan was 6.02% and 3.78%, respectively. Moreover, the values of NSE showed an increase in the two stations. NSE decrease was 8.19% in Ahvaz. AE of DWS-I in Ahvaz and Zanjan was negative and positive, respectively, reflecting the underestimated and overestimated forecasts. DWS-II exhibited better performance relative to the single models, but the difference in the evaluation metrics of DWS-II and DWS-I was low, especially in Ahvaz station. For example, in Ahvaz, the RMSE of DWS-I and DWS-II was 0.971 and 0.973, while its NRMSE was 0.059 and 0.06, respectively. Generally, DWS-I led to more acceptable results. The second combination of the developed method involved the combination of independent variables using PCA. The coefficients of each variable in the first component are displayed in *Fig. 5*.

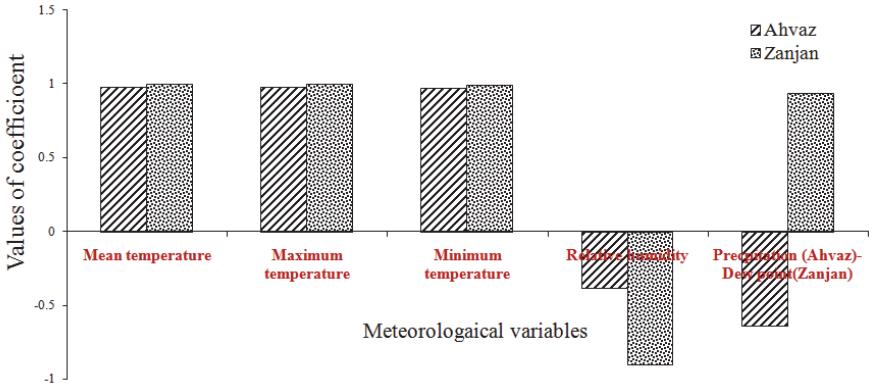

Fig. 5. The coefficients of meteorological variables in the first component of the two stations.

PCA transforms some independent variables into different components by multiplying the coefficient of each variable to its corresponding variable. It must be said thatas a result of this study, DWS implies DWS-I. According to *Fig. 5*, the maximum coefficient of variables in the first component was related to temperature. It also well matches with the variables by high correlation coefficient of *Table 2*. Finally, the incorporation of independent and output variables was conducted using PCA and DWS with SVR. The comparison of DWS with the novel method is represented in *Fig. 6*.

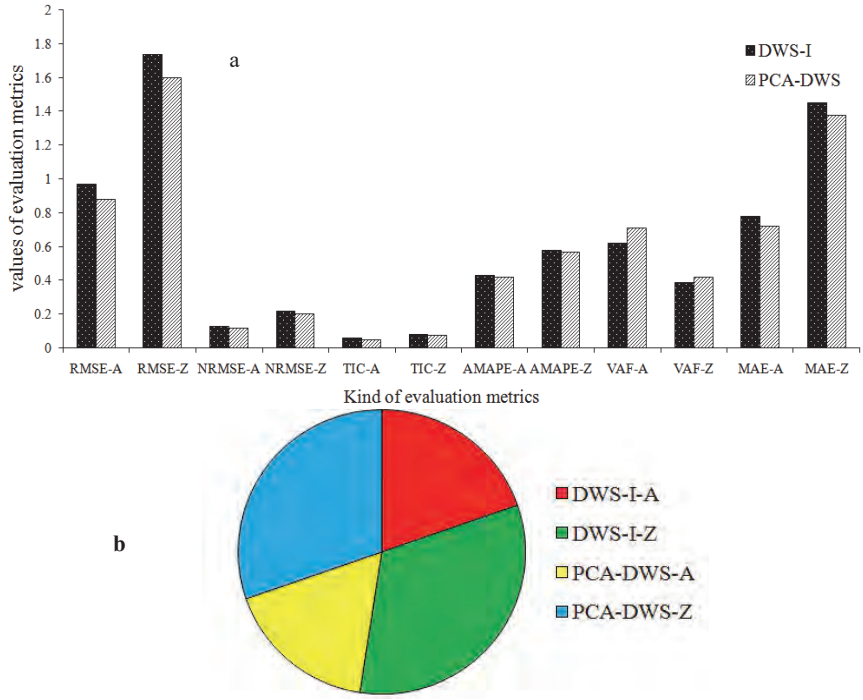

Fig. 6. Comparison of combined and proposed methods with some evolution metrics (a), investigation of the forecast stability of two methods with DIS (b). A and Z indicate Ahvaz and Zanjan.

Evaluation metrics of the proposed method in *Fig. 6a* suggests a better situation for the proposed method than for DWS. The RMSE, NRMSE, TIC, AMAPE, and MAE decrease from DWS to PCA-DWS was 9.27%, 7.69%, 15.25%, 2.32%, and 7.69% for Ahvaz and 8.04%, 9.09%, 7.59%, 1.21%, and 4.82% for Zanjan, respectively. The average decline of RMSE, NRMSE, TIC, AMAPE, and MAE was 8.44% and 6.15% for Ahvaz and Zanjan, respectively, showing a greater decline in calculated average values for Ahvaz than for Zanjan. The rise in VAF from DWS to the proposed method was 14.51% and 7.69% for Ahvaz and Zanjan, respectively. The value of VAF in Ahvaz was higher than in Zanjan. Also, the NRMSE of Ahvaz was lower than of Zajnan. The share of the pie diagram in *Fig. 6b* was decreased by the incorporation of independent and output variables. It indicates the more preservation of forecasts stability in the proposed method. DIS decrease from DWS to the proposed method in Ahvaz and Zanjan was 11.45% and 7.5%, respectively. Positive AE values were seen in the two stations using PCA-DWS, indicating the overestimation of the forecast. The variation of wind speed in the verification period is shown in *Fig. 7*.

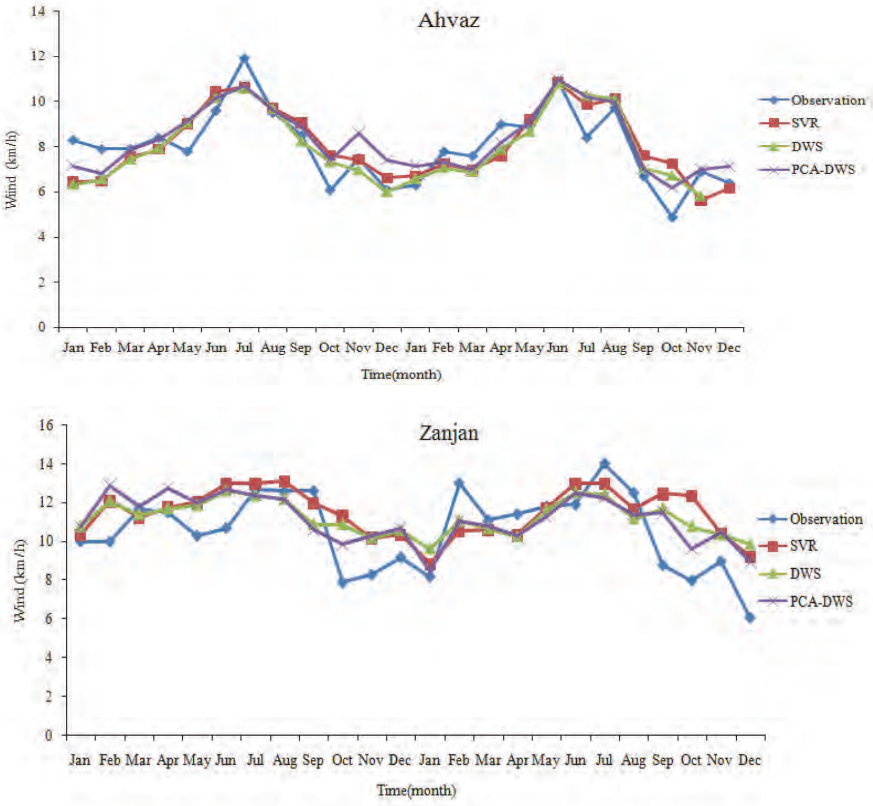

Fig. 7. Observed and forecasted monthly wind speeds with different models in the verification period, 2019-2020, for the two stations.

The average maximum wind speed during the two years of the verification period, 2019 and 2020, occurred in June in the observation data; this time was preserved with SVR, DWS, and PCA-DWS in Ahvaz. The minimum observed wind speed was in October, which was only preserved in the PCA-DWS method. The fitted R-square of the lines presents the maximum value for the PCA-DWS method. The increment in the R-square of the fitted lines from SVR and DWS to PCA-DWS method was 18.4% and 9.45% for Ahvaz and 44.8% and 16.6% for Zanjan, respectively. To compare the performance of the studied models (with regard to linear regression), PRMSE, PNRMSE, PTIC, and PNSE were calculated in *Table 4.*

Table 4. Some improvement percentage indicators for comparison of PCA-DWS with other models.

Station	Indicators	SVR	GMDH	DWS-I	PCA-DWS
Ahvaz	PRMSE	0.41	0.15	0.51	0.67
	PNRMSE	0.5	0.16	0.52	0.66
	PTIC	0.42	0.17	0.52	0.8
Zanjan	PRMSE	0.53	0.3	0.64	0.79
	PNRMSE	0.56	0.33	0.63	0.8
	PTIC	0.54	0.36	0.64	0.78

The maximum and minimum values of improvement indicators were related to PCA-DWS and GMDH. The maximum value of indicators was for PTC and PNRMSE, while the minimum values of the indicator were seen for PRMSE. In the following, the performance of the proposed method for monthly wind speed forecasting was investigated one by one; the RRMSE values are presented in *Fig. 8*.

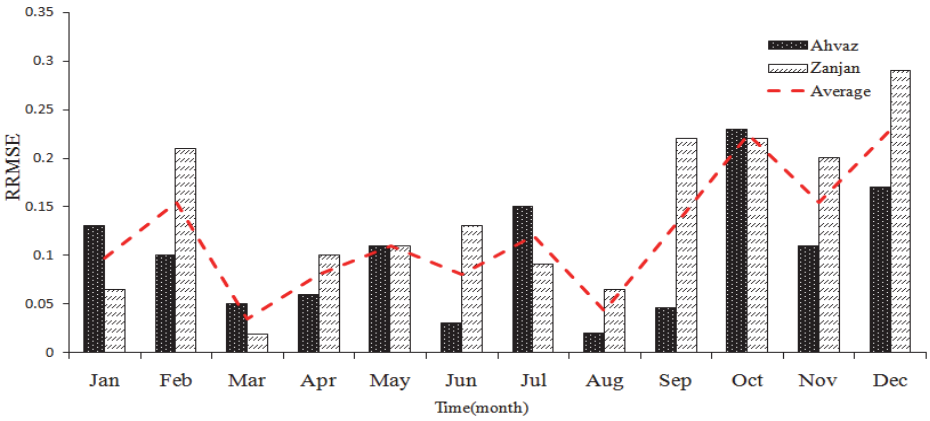

Fig. 8. Performance of PCA-DWS in each month of the verification period for the two stations with RRMSE.

The minimum value of RRMSE in *Fig. 8* for Ahvaz, Zanjan, and their average was in August, March, and March, respectively. The maximum value of RRMSE was in October and December. It can be said that the maximum value of RRMSE occurred in autumn. The maximum value of RRMSE in Ahvaz was lower than in Zanjan, whereas a similar minimum value of RRMSE was detected in the two stations. Adherence of average series from Zanjan series can be assigned to the high error in wind forecasting of Zanjan relative to Ahvaz. To investigate the performance of the novel method, another comparison was made related to the annual scale whose results are depicted in *Fig.9*.

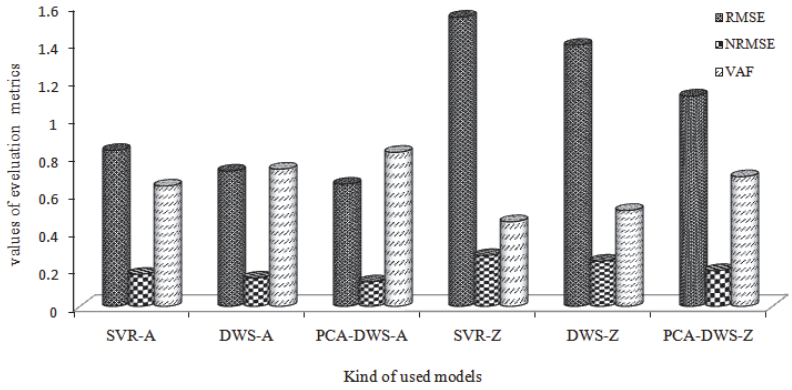

Fig. 9. Some evaluation metrics for PCA-DSW performance evaluation in annual scale. A and Z indicate Ahvaz and Zanjan.

In *Fig. 9* PCA-DWS led to better forecasts relative to SVR and DWS. The RMSE decrease from SVR to DWS and DWS to PCA-DWS was 13.25% and 9.77% in Ahvaz and 9.74% and 19.42% in Zanjan, respectively. The NRMSE decline from SVR to DWS and DWS to PCA-DWS was respectively 11.76% and 13.33% in Ahvaz and 11.11% and 20.88% in Zanjan. The increment in VAF from SVR to DWS and DWS to PCA-DWS was 14.06% and 12.32% in Ahvaz and 13.33% and 35.29% in Zanjan, respectively. In Ahvaz, the VAF of PCA-DWS was lower than that of in Zanjan. VAF of each station in the annual series was higher than in the monthly series. The observed annual wind speed in the two stations in 2019 was greater than in 2020, which was preserved in the PCA-DWS method.

4. Discussion

One approach for meteorological data forecasting is to model meteorological variables with the best correlation with each other. *Afkhami et al*. (2015); *Kumar* and *Malik* (2016), and *Khosravi et al*. (2018) employed meteorological data such as temperature to forecast wind speed. In this study, temperature and relative humidity showed the maximum significant correlation with wind speed. The effect of temperature on wind speed was also reported by *Khakzad et al.* (2017) and *Wang et al*. (2021b). Linear regression, the GMDH, and SVR were used to model the relation between correlated meteorological variables and wind speed. In each station, SVR outperformed GMDH and linear regression methods. The superiority of SVM to GMDH was reported in some studies such as the work of *Khosravi et al.* (2018) for wind speed and direction forecasting, *Raza et al*. (2020) for evapotranspiration estimation in four climatic regions, and *Yaghoubi et al.* (2019) for monthly forecasting of streamflow. Comparison of the performance of three models indicated that the NRMSE of SVR in Zanjan was greater than in Ahvaz, while the VAF of SVR in Ahvaz was larger than in Zanjan. Therefore, for increasing the accuracy of forecasts, the mentioned single models were combined using the DWS method. The forecasting performance of DWS was better than the forecasts of three individual models. The rise in VAF from SVR to DWS for Zanjan and Ahvaz was 34.48% and 10.71%, respectively. The combinational forecast is a function involving the sum of weight-assigned single forecast models. The contribution of the single models on the final forecast was determined considering their weights. Therefore, a proper function in the forecast combination process can derive the information of the single models to improve the accuracy of the results. The forecast combination methods reduced the forecasted errors and led to high accuracy (*Adhikari* and *Agrawal*, 2014; *Wang et al*., 2020*; Dewangan et al*., 2020). The evaluation metrics of DWS-I and DWS-II have shown low differences in many cases. For example, the NSE of Ahvaz for DWS-I and DWS-II was 0.66 and 0.662, respectively, whereas the NRMSE of Zanjan for DWS-I and DWS-II was 0.22 and 0.23, respectively. In general, however, DWS-I outperformed DWS-II. One of the reasons explaining the poor performance of DWS-II compared to DWS-I might be the presence of ν and β. *Winkler* and *Makridakis* (1983) recommended $\nu=12$ and $\beta=0.7$. In this study, $\nu=12$ and β value was manually selected in the range of $0<\beta<1$. The values of parameters can indeed affect the forecasting performance of the combinational methods. Restriction of the forecasting to the recent observation can be due to smaller values of ν. Smaller values of β guarantee assigning more weights to recent observations (*Adhikari* and *Agrawal*, 2014). Therefore, differences in weight allocation can affect the forecasts. Regarding the success of the DWS method for wind forecasting, a novel method was proposed to increase the accuracy of DWS by using PCA on independent variables. The accordance of PCA-DWS forecasts with observed wind speed was higher than that of DWS and

SVR. The rise in NSE from DWS to the novel method in Ahvaz and Zanjan stations was 9.09% and 37.39%, respectively. The use of PCA-DWS in Ahvaz led to lower NRMSE values compared to Zanjan. The values of VAF in Ahvaz was higher than in Zanjan. The excellent performance of DWS-PCA relative to other mentioned methods was verified with the R-square of the fitted lines and some improvement percentage indicators. In addition to the monthly time scale, the PCA-DWS exhibited a proper performance on the annual scale. The VAF of the annual scale in the two stations was higher than the VAF of the monthly scale.

5. Conclusions

Wind forecasting with an accurate model can be useful in renewable energy studies, climate sciences, and hydrology studies. To increase the accuracy of wind speed forecasting, the forecast performance of three single models (linear regression, SVR, and GMDH) were combined using the DWS method. DWS outperformed the three models. Another aspect in improving the accuracy of DWS forecasts is the incorporation of DWS and PCA that exhibited good performance on annual and monthly scales. Performance comparison of the two stations indicated the better performance of Ahvaz than the performance of Zanjan, which can be due to climate effects. Some issues can affect the wind forecasting performance of PCA-DWS: 1) Using power model as the single model and its accurate sensitivity analysis. One approach to improve the performance of single models is to determine the model parameters through optimization methods such as genetic algorithm (GA) or PSO. 2) Type of forecast combination method to find the exact weights of the single models for deriving their information. 3) Using the rotation option related to the components in PCA to combine independent variables. 4) Using an efficient model for the incorporation of PCA and DWS. The novel developed method in this study offered proper effectiveness, forecasting accuracy, and stability, further encouraging its application in monthly and annual wind speed forecasts.

References

Acosta, S.M., Amoroso, A.L., Sant'Anna, Â.M.O., and *Junior, O.C.,* 2022: Predictive modeling in a steelmaking process using optimized relevance vector regression and support vector regression. *Ann. Operat. Res.* 316(2), 905–926. https://doi.org/10.1007/s10479-021-04053-9

Adhikari, R., and *Agrawal, R.K.,* 2014: Performance evaluation of weights selection schemes for linear combination of multiple forecasts. *Artific. Intellig. Rev. 42(4)*: 529–548. https://doi.org/10.1007/s10462-012-9361-z

Afkhami, H., Talebi, A., Mohammadi, M., and *Fotouhi, F.,* 2015: Investigation of the feasibility of wind speed prediction using hybrid model of neural networks, neural-fuzzy networks and wavelet (Case Study: Station of Yazd), *Iranian J. Watershed Manag. Sci. Engin. 9(30):* 31–40.

Armstrong, J.S., 2001: Principles of forecasting: a handbook for researchers and practitioners. .Kluwer Academic Publishers, Boston, *USA.* https://doi.org/10.1007/978-0-306-47630-3

Avci, E., and *Turkoglu, I.*, 2009: An intelligent diagnosis system based on principal component analysis and ANFIS for the heart valve diseases. *Exp. Syst. Appl. 36*(2) 2873–2878. https://doi.org/10.1016/j.eswa.2008.01.030

De Martonne, E., 1925: Traité Géographie. Physique: 3 tomes. Max leclcrc and H. Bourrclier, proprietors of Librairic Armard Colin: Paris. (In France)

Dewangan, C.L., Singh, S.N., and *Chakrabarti, S.*, 2020: Combining forecasts of day-ahead solar power. *Energy 202*, 117743. https://doi.org/10.1016/j.energy.2020.117743

Dhiman, H.S., Deb, D., and *Guerrero, J.M.*, 2019: Hybrid machine intelligent SVR variants for wind forecasting and ramp events. *Renew. Sustain. Energy Rev. 108*, 369–379. https://doi.org/10.1016/j.rser.2019.04.002

Emberger, C., Gaussen, H., Kassas, M., and *de Philippis, A.*, 1963: Bioclimatic map of the Mediterranean Zone, explanatory notes. UNESCO-FAO. Paris.

Fazelpour, F., Tarashkar, N., and *Rosen, M.A.*, 2016: Short-term wind speed forecasting using artificial neural networks for Tehran, Iran. *Int. J. Energy Environ. Engin. 7,* 377–390. https://doi.org/10.1007/s40095-016-0220-6

Frietas, P.S.A., and *Rodrigues A.J.L.*, 2006: Model combination in neural-based forecasting. *Eur. J. Oper. Res. 173*, 801–814. https://doi.org/10.1016/j.ejor.2005.06.057

Jamil, M., and *Zeeshan, M.*, 2019: A comparative analysis of ANN and chaotic approach-based wind speed prediction in India. *Neur. Comput. Appl. 31,* 6807–6819. https://doi.org/10.1007/s00521-018-3513-2

Jaseena, K.U., and *Kovoor, B.C.*, 2021: Decomposition-based hybrid wind speed forecasting model using deep bidirectional LSTM networks. *Energy Conv. Manage. 234*, 113944. https://doi.org/10.1016/j.enconman.2021.113944

Khakzad, S.F., Golian, S., and *Elmi, M.*, 2017: Predicting wind speed and direction using the output of numerical meteorological models. MSc Thesis in Shahrood University of Technology.

Khosravi, A., Koury, R.N., Machado, L., and *Pabon, J.J.*, 2018: Prediction of wind speed and wind direction using artificial neural network, support vector regression and adaptive neuro-fuzzy inference system. *Sust. Energy Technol. Assess. 25*, 146–160. https://doi.org/10.1016/j.seta.2018.01.001

Kumar, G., and *Malik, H.*, 2016: Generalized regression neural network based wind speed prediction model for western region of India. *Procedia Comput. Sci. 93*, 26–32. https://doi.org/10.1016/j.procs.2016.07.177

Liu, Z., Hara, R. and *Kita, H.*, 2021: Hybrid forecasting system based on data area division and deep learning neural network for short-term wind speed forecasting. *Energy Conver. Manage. 238*, 114136. https://doi.org/10.1016/j.enconman.2021.114136

Luo, L., Li, H., Wang, J., and *Hu, J.*, 2021: Design of a combined wind speed forecasting system based on decomposition-ensemble and multi-objective optimization approach. *Appl. Math. Model. 89*, 49–72. https://doi.org/10.1016/j.apm.2020.07.019

Minaeian, B. and *Ahangari, K.*, 2013: Estimation of uniaxial compressive strength based on P-wave and Schmidt hammer rebound using statistical method. *Arabian J. Geosci. 6,* 1925–1931. https://doi.org/10.1007/s12517-011-0460-y

Newbold, P. and *Granger, C.W.J.*, 1974: Experience with forecasting univariate time series and the combination of forecasts. *J. Roy.Stat. Soc.: General, 137(2)*: 131–146. https://doi.org/10.2307/2344546

Pan, L., Liu, Y., Roux, G., Cheng, W., Liu, Y., Hu, J., Jin, S., Feng, S., Du, J., and *Peng, L.*, 2021: Seasonal variation of the surface wind forecast performance of the high-resolution WRF-RTFDDA system over China. *Atmos. Res. 259*, 105673. https://doi.org/10.1016/j.atmosres.2021.105673

Raza, A., Shoaib, M., Faiz, M.A., Baig, F., Khan, M.M., Ullah, M.K., and *Zubair, M.*, 2020: Comparative assessment of reference evapotranspiration estimation using conventional method and machine learning algorithms in four climatic regions. *Pure Appl. Geophys. 177*, 4479–508. https://doi.org/10.1007/s00024-020-02473-5

Razzaghi, H., Madandoust, R., and *Aghabarati, H.*, 2021: Point-load test and UPV for compressive strength prediction of recycled coarse aggregate concrete via generalized GMDH-class neural network. *Constr. Build. Mater. 276*, 122143. https://doi.org/10.1016/j.conbuildmat.2020.122143

Song, C. and *Fu, X.*, 2020: Research on different weight combination in air quality forecasting models. *J. Clean. Product. 261*, 121169. https://doi.org/10.1016/j.jclepro.2020.121169

Temeng, V.A., Ziggah, Y.Y., and *Arthur, C.K.,* 2020: A novel artificial intelligent model for predicting air overpressure using brain inspired emotional neural network. *Int. J. Mining Sci. Technol. 30*(5), 683-9. https://doi.org/10.1016/j.ijmst.2020.05.020

Ul-Saufie, A.Z., Yahaya, A.S., Ramli, N.A., Rosaida, N., and *Hamid, H.A.,* 2013: Future daily PM10 concentrations prediction by combining regression models and feedforward backpropagation models with principal component analysis (PCA). *Atmos. Environ. 77*, 621–630. https://doi.org/10.1016/j.atmosenv.2013.05.017

Ul-Saufie, A.Z., Yahya, A.S., and *Ramli, N.A.,* 2011: Improving multiple linear regression model using principal component analysis for predicting PM10 concentration in Seberang Prai, Pulau Pinang. *Int. J. Environ. Sci. 2*, 403–410.

Vapnik, V.N., 1998: Statistical learning theory. John Wiley & Sons.

Wang, J., Li, Q., and *Zeng, B.,* 2021a: Multi-layer cooperative combined forecasting system for short-term wind speed forecasting. *Sust. Ener. Technol. Assess. 43*, 100946. https://doi.org/10.1016/j.seta.2020.100946

Wang, J., and *Wang, J.,* 2015: Forecasting stock market indexes using principle component analysis and stochastic time effective neural networks. *Neurocomputing 156*, 68–78. https://doi.org/10.1016/j.neucom.2014.12.084

Wang, J., Zhou, H., Hong, T., Li, X., and *Wang, S.,* 2020: A multi-granularity heterogeneous combination approach to crude oil price forecasting. *Energy Econ. 91*, 104790. https://doi.org/10.1016/j.eneco.2020.104790

Wang, Z.W., Zhang, W.M., Zhang, Y.F., and *Liu, Z.,* 2021b: Circular-linear-linear probabilistic model based on vine copulas: An application to the joint distribution of wind direction, wind speed, and air temperature. *J. Wind Engineer. Indust. Aerodynam. 215*, 104704. https://doi.org/10.1016/j.jweia.2021.104704

Winkler, R.L. and Makridakis, S., 1983: The combination of forecasts. J. Roy. Stat. Soc.: General 146(2), 150–157. https://doi.org/10.2307/2982011

Xie, A., Yang, H., Chen, J., Sheng, L., and *Zhang, Q.,* 2021: A Short-Term Wind Speed Forecasting Model Based on a Multi-Variable Long Short-Term Memory Network. *Atmosphere 12*(5), 651. https://doi.org/10.3390/atmos12050651

Yaghoubi, B., Hosseini, S.A., and *Nazif, S.,* 2019: Monthly prediction of streanflow using data-driven models. *J. Earth Syst. Sci. 128*(6), 1–15. https://doi.org/10.1007/s12040-019-1170-1

Yang, H., Zhu, Z., Li, C., and *Li, R.,* 2020: A novel combined forecasting system for air pollutants concentration based on fuzzy theory and optimization of aggregation weight. *Appl. Soft Comput. 87*, 105972. https://doi.org/10.1016/j.asoc.2019.105972

DOI:10.28974/idojaras.2023.1.5

IDŐJÁRÁS

Quarterly Journal of the Hungarian Meteorological Service
Vol. 127, No. 1, January – March, 2023, pp. 77–106

Regional climate projections of heavy precipitation over the Balkan Peninsula

Rilka Valcheva* and **Valery Spiridonov**

National Institute of Meteorology and Hydrology (NIMH)
66 Tsarigradsko Shose blvd, 1784 Sofia, Bulgaria

**Corresponding author E–mail: Rilka.Valcheva@gmail.com*

(Manuscript received in final form May 9, 2022)

Abstract— This article presents climate change projections of heavy (above a certain threshold) precipitation under the Representative Concentration Pathways RCP4.5 and RCP8.5 for the territory of the Balkan Peninsula. The focus is on convective rainfall which, if significant, can damage infrastructure and cause casualties. For this purpose, RegCM4.4.5 regional climate model with 20 km resolution was used for the periods 2021–2050 and 2071–2099 compared with the reference period 1975–2004. The change in the number of heavy rainfalls is determined by using the thresholds in the Meteoalarm program corresponding to the 'yellow' code. It is found that the largest changes in the number of convective precipitation events are in the coastal and mountainous areas. The increase in the number of cases of heavy rainfalls does not exclude the decrease in the amount of precipitation in these areas. This can be explained by the increase in the period in which these precipitations are possible due to the increase in temperatures.

Key-words: climate projections, heavy rainfalls, heavy convective rainfalls, RegCM, Meteoalarm

1. Introduction

The FP7 RAIN project (http://rain-project.eu/wp-content/uploads/2015/11/D2.3-Warning-Systems.pdf) notes the view expressed by stakeholders that critical infrastructure can be affected by convective events of high intensity and short duration. This is the reason why this work focuses on convective precipitation. This type of rainfall can cause different types of flooding, with flash floods being the most dangerous. They are difficult to predict, occur over a short period and can cause human casualties in addition to material damages.

The mechanism of increased heavy rainfall in the future climate is discussed in *Trenberth* (2011). It is mentioned that the water holding capacity of air increases with warming of the atmosphere. This leads to an increase in water vapor. As a result, storms, whether or not separate thunderstorms, cause more intense rainfall. An increase in the number of intense precipitations is even observed when the total amount of precipitation decreases (*Myhre et al.,* 2019). The increase in water content is considered to be the main reason for the increase in rainfall intensity in a number of studies, for example in *Dourte et al.* (2015). In areas with a general decrease in annual precipitation, the increase in the number of intensive precipitations is a consequence of the fact that the conditions for their occurrence become more likely in more months of the year. It is known that heavy rainfall prevails during the warm period of the year. Their character is mainly convective. In *Berg et al*. (2013) it is mentioned that in contrast, convective precipitation exhibited characteristic spatial and temporal scales, and its intensity in response to warming exceeded the Clausius – Clapeyron rate. It is concluded that convective precipitation reacts much more sensitively to rising temperatures than stratiform precipitation, becoming dominant in extreme precipitation. It is also noted that the Clausius - Clapeyron relation describes the rate of change of saturation vapor pressure of approximately 7% for every 1 ºC rise in at typical surface temperatures, and thereby sets a scale for increases in precipitation extremes. A statistically significant connection with near-surface temperature changes at a rate of between 5.9% and 7.7% for every 1 K rise in temperature is mentioned in *Westra et al*. (2013). A clear meridional dependence is also noted. According to *Hawcroft et al*. (2018), an increase in the number of extra tropical cyclones is the mechanism leading to an increase in extreme rainfall in the Northern Hemisphere (Europe and North America).

The increase of convective precipitation which is greater than the decrease of stratiform precipitation is noted in *Chernokulsky et al.* (2019). The influence of mountains and topography on precipitation and their intensity has been reviewed by many authors. The mechanism of impact of the mountains is described in *Houze* (2012). The convective systems are affected by channeling of airflow. The stratiform regions of mesoscale convective systems are enhanced by upslope flow when they move over mountains. In *Kirshbaum et al*. (2018) it is concluded, that the larger-scale background flow, local evapotranspiration, and transport of moisture, as well as thermodynamic heterogeneities over the complex terrain, regulate moist instability. It is noted there that longstanding limitations in the quantitative understanding of related processes, including both convective preconditioning and initiation, must be overcome to improve the prediction of this convection, and its collective effects in weather and climate models. According to *Shi* and *Durran* (2016), the sensitivity of extreme precipitation to warming in the climate simulations is lower over the mountains than over the oceans and plains. On the contrary, in *Giorgi et al.* (2016), the

summer precipitation was analyzed over the Alpine region in an ensemble of twenty-first-century projections with high-resolution (12 km) regional climate models. They found that the regional models simulate an increase in precipitation over the high Alpine elevations that is not present in the global simulations. That was associated with increased convective rainfall due to enhanced potential instability by high-elevation surface heating and moistening. It can be assumed that the reduction of convective rainfalls in mountainous areas is due to the used thresholds. In the mountains, there is an effect of forced convection that leads to an increase in precipitation. For these to be more intense, additional surface super-heating is required, which occurs in lowland areas but is probably not sufficient at temperatures that decrease with height. The presence of snow cover additionally reduces the conditions for deep convection. This prevents the mountainons areas from reaching accepted thresholds for rainfall intensity. Model resolution is also important for rainfall amounts.

This article uses the definitions given by the WMO (2016). It is noted that there were large variations in precipitation patterns throughout the world, and it was not possible to use a single definition of extreme precipitation event that was suitable for all regions. According to the definition it was recognized generally, that when a precipitation event was considered to be extreme, it related to one of the following two contexts: (1) it exceeded a certain threshold, i.e., a fixed threshold, that has a certain associated impact, or (2) it could be considered to be extreme due to its rarity, i.e., a percentile-based threshold or based on its return period. It is mentioned that for the percentile-based threshold, the rarity of occurrence tended to take the form of the upper 90th, 95th, and 99th percentile of precipitation and such percentile-based thresholds could be derived from statistical cumulative density functions generated from the observed data or some conceptual distributions for precipitation extremes (such as generalized extreme value, GEV). It is also noted that when considering the most extreme precipitation events, return period information on the extremely rare events (100 years or more) was important for many engineering applications.

The second approach, although theoretically more reasonable, leads to certain difficulties. The problems arising from different methods for extreme precipitation assessment are commented in *Schär et al.* (2016), *Turco et al*. (2017), *Fougeres et al.* (2015), *Luo et al*. (2017). These problems are primarily related to the low frequency of such events, both for the past period and for simulations for future periods. As mentioned in *Jeon et al*. (2016), there was a risk that bias correction could mask serious model errors in simulating the processes responsible for the extreme event in question. This risk was also present in more commonly-used bias correction techniques such as the use of anomalies based on subtracting off or dividing by a reference value.

The role of temperature in the sub-daily convective precipitations is discussed in *Park* and *Min* (2017). It is mentioned that they are more sensitive to temperature changes as a result of the statistical effect that involves the

transition from stratiform to convective types and the physical effect by which the convective process itself can overcome the thermodynamic limitation of the Clausius–Clapeyron relationship. The existing problem with the sub-daily precipitation is mentioned in *Alexander* (2016). It is also noted that another issue for extremes was the general mismatching of the spatial scales between observations (usually taken at point locations) and climate model simulations (typically interpreted as representing an area of a model grid), making it difficult to conduct a like-with-like comparison between observations and models. In *Westra et al*. (2014) it is mentioned, that low-resolution models have limited ability to simulate sub-daily precipitation extremes, as they do not explicitly resolve convective processes. This casts strong doubts on future projections in sub-daily precipitation extremes. This could be possible only if models had convection-permitting resolutions. Similar remarks shared by other authors justify the method adopted here using daily precipitation. The aim is to find the appropriate definition of extreme rainfall that can be applied to any grid-point of the model integration area.

According to *IPCC* (2012), it is likely that there have been statistically significant increases in the number of heavy precipitation events in more regions than there have been statistically significant decreases, but there are strong regional and sub-regional variations in the trends. There is also high confidence that changes in heavy precipitation will affect landslides in some regions. It is likely that the frequency of heavy precipitation or the proportion of total rainfall from heavy rainfalls will increase in the 21st century over many areas of the globe. The projected seasonal mean changes in temperature and heavy precipitation for three emission scenarios (A1B, RCP45, RCP85) over Europe are presented in *Jacob et al.* (2014). Projections show an increase in heavy precipitation in most parts of Europe in winter by up to 35% during the end of the century and an increase in the summer heavy precipitation, except Southern Europe. A greater annual mean atmosphere warming is shown in Southern Europe and towards the northeast. It is also shown that large parts of Eastern Europe and the Alpine region might be exposed to a temperature increase of more than 4.5 ºC by the end of the century. They also found that the high-resolution in the simulations is clearly visible in the change pattern for heavy precipitation events. The more detailed spatial patterns in the high-resolution simulations can be related to better resolved physical processes like convection and heavy precipitation.

According to the latest IPCC AR6 report (*IPCC*, 2021), the frequency and intensity of heavy precipitation events have likely increased at the global scale over a majority of land regions. Heavy precipitation has likely increased on the continental scale over Europe and will generally become more frequent and more intense with additional global warming. Human influence, in particular greenhouse gas emissions, is likely the main driver of the observed global scale intensification of heavy precipitation in land regions.

In *Vautard et al.* (2021), the performance of the large EURO-CORDEX ensemble was analyzed. This ensemble consisted of 55 simulations combining 8 global climate models (GCMs) and 11 regional climate models (RCMs). They focused on biases for the most important climate variables like temperature, precipitation, wind, radiation, sea level pressure, and a variety of extreme and impact oriented indices. They found that the simulations were overall too cold, too wet, and too windy compared to available observations or reanalyses. They have also found that the substantial model overestimation of heavy precipitation indices when assessed with E-OBS data could be reduced by resorting to high-resolution precipitation data sets, which had a denser station network, especially in topographically complex regions.

A companion paper (*Coppola et al.*, 2021) was providing an analysis of future projections, including comparison between EURO-CORDEX, CMIP5, and CMIP6 ensembles. This paper analyzed the ensemble of regional climate model projections for Europe completed within the EURO-CORDEX project. Projections were available for the two greenhouse gas concentration scenarios RCP2.6 (22 members) and RCP8.5 (55 members) at 0.11 degree resolution from 11 RCMs driven by 8 GCMs. They concluded that the maximum warming was projected by all ensembles in Northern Europe in winter, along with a maximum precipitation increase there; in summer, maximum warming occurred in the Mediterranean and Southern European regions associated with a maximum precipitation decrease. For the mean European climate, the south-north seasonal gradients in temperature and precipitation change signals were projected, with maximum warming and increase in precipitation over the northern regions in winter and maximum warming and a significant decrease in precipitation over the southern regions in summer, and in particular over the Mediterranean basin.

Recently, ensembles of models are often used to assess possible climate change. This assessment is an estimate of uncertainty rather than the basis for any averaged and more reliable scenario, because different regional models with different resolutions and driving global models have different estimates of possible changes in the temperature and rainfalls. The regional model RegCM4 (*Giorgi et al.*, 2012) was used in this work. The systematic errors in the previous version RegCM3 have been investigated in *Bergant et al.* (2007). The model shows a cold averaged bias over Europe with the exception of the northern part between −1.2 °C and +1.0 °C. It also shows a prevailing wet averaged bias. The distinction between coastal and inland regions can also be seen. An overview and analysis of newer versions of the regional models involved in the Med-CORDEX simulation can be seen in *Somot et al.* (2018). The Med-CORDEX domain includes the Mediterranean climate zone, the Mediterranean Sea, and the river catchment basins of the Mediterranean and Black Seas. As mentioned, many factors like strong land-sea contrast, ground-atmosphere feedback, intensive air-sea connection and aerosol-radiation interaction, as well as a variety of regional characteristics must be taken into account when modeling the

Mediterranean climate. In this study, a smaller and climatically homogeneous area was selected compared to those used for Europe. It includes the Balkan Peninsula and part of the Apennine Peninsula. This is done on the assumption that the factors that determine climate change are more homogeneous. Thus, we can expect a more appropriate estimate of the change in the number of intense convective precipitation events.

2. Data and method

The aim of the article is to present a possible way of estimating the expected changes in heavy rainfall. The goal is not to compare different models or model modifications. The RegCM version 4.4.5 regional climate model (*Giorgi et al.*, 2012) forced with boundary conditions from HadGEM2-ES global climate model (Hadley Centre Global Environment Model - Earth-System version 2, (*Collins et al*., 2011) has been used. The RegCM4 originates from the regional climate model developed by *Giorgi et al.* (1993a, 1993b). RegCM4.4.5 has a dynamical core of the fifth-generation Mesoscale Model (MM5) from the National Center for Atmospheric Research (NCAR) and Pennsylvania State University (*Grell et al.,* 1994). The RegCM4 is a hydrostatic, compressible, sigma-p vertical coordinate model run on an Arakawa B-grid. It uses the radiation scheme of the Community Climate Model 3 (CCM3) (*Kiehl et al.,* 1996). Many studies on the validation and calibration of numerical models have been published lately (*Torma et al*., 2011; *Pieczka et al.*, 2016; *Kotlarski et al*., 2014; *Giorgi et al.*, 2012). In addition, numerical models depend on a set of initial variables and parameters, as they use a series of simplifications and parameterizations of natural processes. In this study, the Grell scheme (*Grell,* 1993) with the Arakawa – Schubert (*Arakawa* and *Schubert*, 1974) closure assumption (Grell-AS) was used for convective precipitation parametrization. A sensitivity analysis of five experiments with different convective precipitation schemes found that the model sensitivities of extreme precipitation to global warming are lower over mountains than over oceans and plains sensible to the choice of cumulus convection scheme, and that the most appropriate convective precipitation scheme in the region covering Bulgaria is the Grell scheme with Arakawa-Schubert closure (*Valcheva* and *Peneva*, 2014). For large-scale non-convective precipitation, the sub-grid explicit moisture scheme (SUBEX) (*Pal et al*., 2000) was used. The second-generation biosphere–atmosphere transfer scheme (BATS) (*Dickinson et al*., 1993) was used for simulating land surface processes. Sensitivity experiments of RegCM4 to planetary boundary layer parameterization were done by *Güttler et al*. (2014), where the planetary boundary layer modeled on the basis of the modified scheme of *Holtslag et al*. (1990) is used. More details on the model can be found in *Elguindi et al*. (2014). The model employs 18 vertical sigma levels, with a model top at 25 hPa and a

bottom at 995 hPa. A simulation domain covering the Balkan Peninsula and part of the Apennine Peninsula is presented using Lambert conformal projection suitable for mid-latitudes (*Fig. 1*). The domain was centered at 24 E - 42 N, with a grid size of 20 km and 128×96 grid points, which correspond to 2560×1920 km^2. These spatial resolution leads to a time step of 60 seconds according to Courant - Friedrichs - Lewy criterion. The results are shown after removing the buffer zone from 12 grid points from each side of the domain. RCP scenarios were used in this study (*Moss et al*., 2010). The experiments were according to the RCP4.5 (*Thomson et al*., 2011) and RCP8.5 (*Riahi et al.,* 2011) scenarios. The reference period is from 1975 to 2004. The future periods are from 2021 to 2050 and from 2071 to 2099.

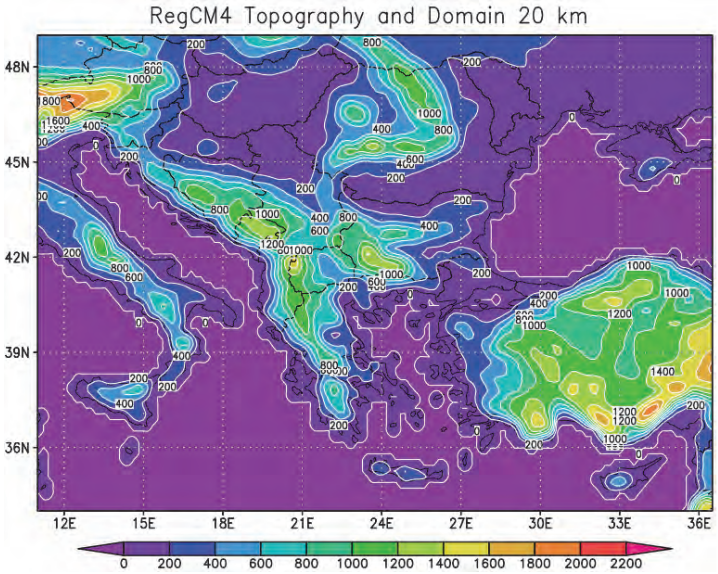

Fig. 1. Regional climate model topography (m) and domain size after removing the buffer zone.

The greenhouse gas concentrations in the RCPs closely correspond to the emission trends discussed in *Clarke et al*. (2010). RCP2.6 has a peak in carbon dioxide concentrations around 2050, followed by a modest decline to about 400 ppm, by the end of the century. RCP6 and RCP4.5 show a stabilizing carbon dioxide concentration, close to the median range in the literature. For CO_2, RCP8.5 follows the upper range, rapidly increasing carbon dioxide concentrations (*van Vuuren et al*., 2011). The hypothesis accepted here is that

the increase in greenhouse gases is the reason for the increase in the number of extreme rainfall. This is why we use RCP4.5 (stabilizing concentration) and RCP8.5 (increasing concentration) scenarios for this study.

The climate models make it possible to estimate rainfall intensities for sub-daily internals. As noted, such intervals have drawbacks, also because the shorter the time interval for determining the intensity, the greater the error will be in the extrapolation in the grid points of the model. Together with the circumstances mentioned in Section 1 for sub-daily intervals, this is the reason for estimating the changes in the number of heavy rains over a period of 24 hours.

The thresholds used by Meteoalarm (http://www.meteoalarm.org/) provide such an opportunity. Each country participating in this network has set thresholds for dangerous weather, and in particular for heavy rainfall. The threshold for heavy rainfall depends on both on the climatic norms typical for the country and on the infrastructure. The color scale is

- yellow: the weather is potentially dangerous;
- orange: the weather is dangerous;
- red: the weather is very dangerous.

The infrastructure is taken into account insofar as the purpose of this system is to warn people travelling in Europe of severe weather. This can lead to inhomogeneity in setting the thresholds for heavy rainfall. For example, two areas with the same climate may have different protection facilities. In this case, the warning thresholds may differ. In the region under consideration, the countries falling within it have very close thresholds, as can be seen from the study in the RAIN project.

Following point 1 of the WMO guidelines noted above, fixed thresholds will be examined. An important step is the choice of thresholds for intense (actually 'dangerous' rainfall). In order for the simulations to be relevant, the cases should not be too small. Their number decreases sharply with increasing threshold. Therefore, the accepted values for the ‘yellow’ code in the countries of the district will be used as a measure to change the hazardous precipitation. The threshold amounts are for the 24-hour precipitation. They with the respective threshold values accepted in them are: Bulgaria (15), Croatia (25), Hungary (20), Italy (20), Romania (25), Serbia (30), and Slovenia (20).

These thresholds are also used to determine the risk of floods. Floods depend on many factors, such as basin size, slope, land cover, soil type, etc. These are specific for each catchment and must be taken into account separately when assessing flood risk. Despite the local specific conditions, in *Hurford et al.* (2012) the average 24-hour rainfall leading to floods varies from 20 mm to 45 mm with an average value of about 35 mm.

The expression ‘rare event rule’ (*Taylor*, 2021) is accepted in the statistics: ‘If specifically observed event is extremely rare, then the assumption is probably incorrect’. Two series of events are usually compared:

– an event that easily occurs,
– an event that is highly unlikely to occur.

Here, only the accepted thresholds are compared, without statistical analysis and use of confidence intervals. It is assumed that a detailed statistical analysis with even more observations was performed everywhere before determining the hazard categories.

The E-OBS observational database, version 23.1e (*Cornes et al.*, 2018) is available on a 0.1 and 0.25 degree regular grid. In this study, E-OBS v.23.1e daily precipitation sum above the mentioned threshold were used on 0.25 regular grid, for the period 1975–2004. From *Fig. 1* it is seen, that the cases with precipitation of 30 mm/24h are missing in large areas of the considered domain (including Bulgaria). Increasing the threshold will lead to fewer events and a breach of the rare event rule. In these areas, the ‘yellow code’ thresholds for the country concerned guarantee the existence of an acceptable number of cases (e.g., over 15), but this is not the case for the 'orange code' thresholds.

3. Results and discussions

In *Figs. 2* and *3* we compare the annual number of cases when precipitation is greater than or equal to 15, 20, 25, and 30 mm/24h from observations (*Fig. 2*) and simulations (*Fig. 3*). Firstly, we prepare daily precipitation sum from RegCM precipitation data, after that we count the cases with precipitation above the mentioned thresholds, and finally the result is divided by the number of years (30 or 28, depending on the period) to get annual (seasonal) number of cases (*Fig. 3*). The same procedure is applied for E-OBS precipitation data (*Fig. 2*) in order to compare simulated data with observational data. As we can see, RegCM4 overestimates the annual number of cases above all the thresholds, especially over the Carpathian Mountains, the eastern coast of Adriatic, Ionian and Aegean Seas.

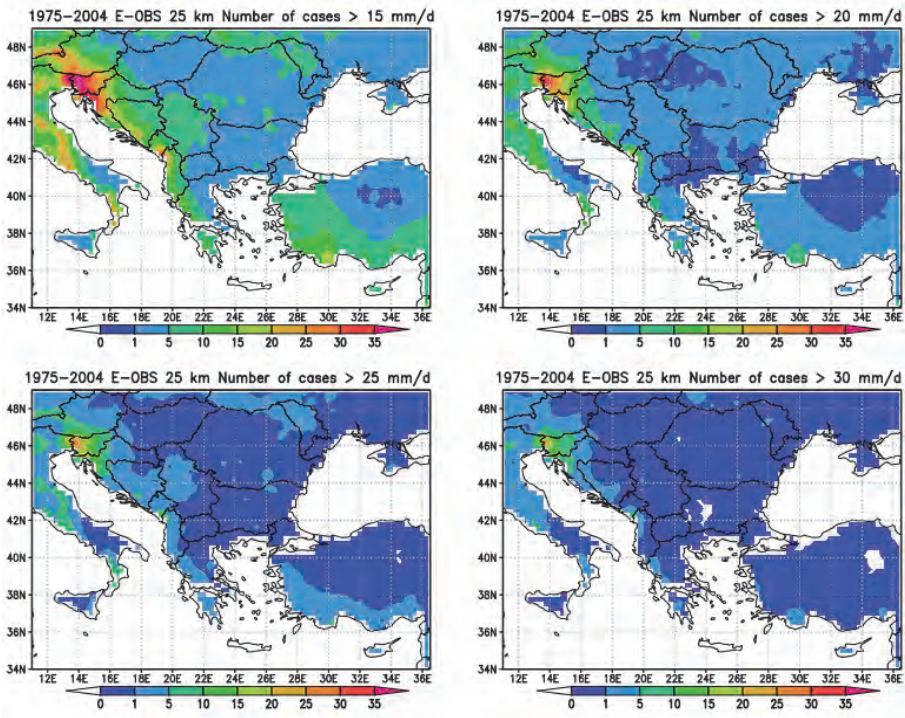

Fig. 2. Annual number of cases when precipitation >= 15, 20, 25, and 30 mm/24h according to the E-OBS precipitation data with 0.25º x 0.25º resolution for the period 1975–2004.

In *Spiridonov* and *Balabanova* (2021), the conclusion is made that the number of cases with convective precipitation over 35 mm / day is preserved during the year, although it decreases in the summer. The reason is the increase in temperature during the other seasons, which creates conditions for the development of convective precipitation. These values are in the 'orange' area of the indicated countries. The experiments were performed using the RCM ALADIN model according to scenario A1B. The consequence of this is that above this threshold, the number of heavy rains will not differ from that for the reference period. The difference is only in their distribution during the year. With warming, the conditions for these precipitation events are available over a larger period of the year, thus compensating the reduction in their number in summer (shown in the article below).

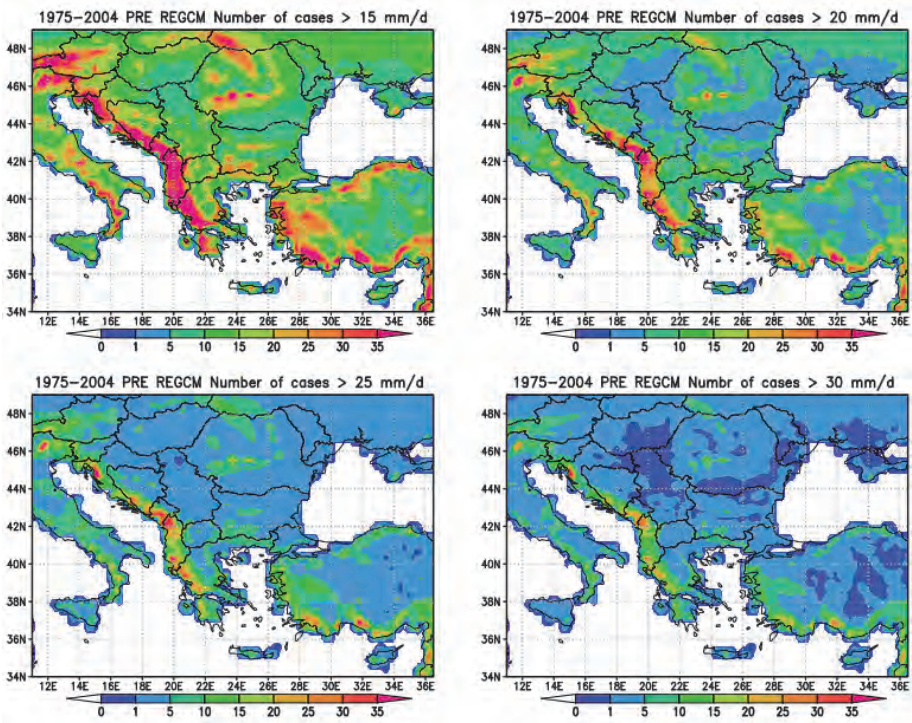

Fig. 3. Annual number of cases when precipitation >= 15, 20, 25, and 30 mm/24h according to the RegCM4 precipitation data with 20 km resolution for the period 1975–2004.

It is noteworthy that the areas with increasing and decreasing number of cases are different for the different intervals of intense rainfall. This may be due to the different effect of temperature conditions for the period under consideration as well as other local conditions. It is possible that the increase in precipitation in one interval is at the expense of their decrease in the other. This problem must be considered on its own.

In *Fig. 4,* simulated annual and seasonal mean changes in temperature in ºC are shown according to the RCP4.5 and RCP8.5 scenarios for the periods 2021–2050 and 2071–2099 compared with the reference period 1975–2004. Warming is observed throughout the year, especially during the summer season.

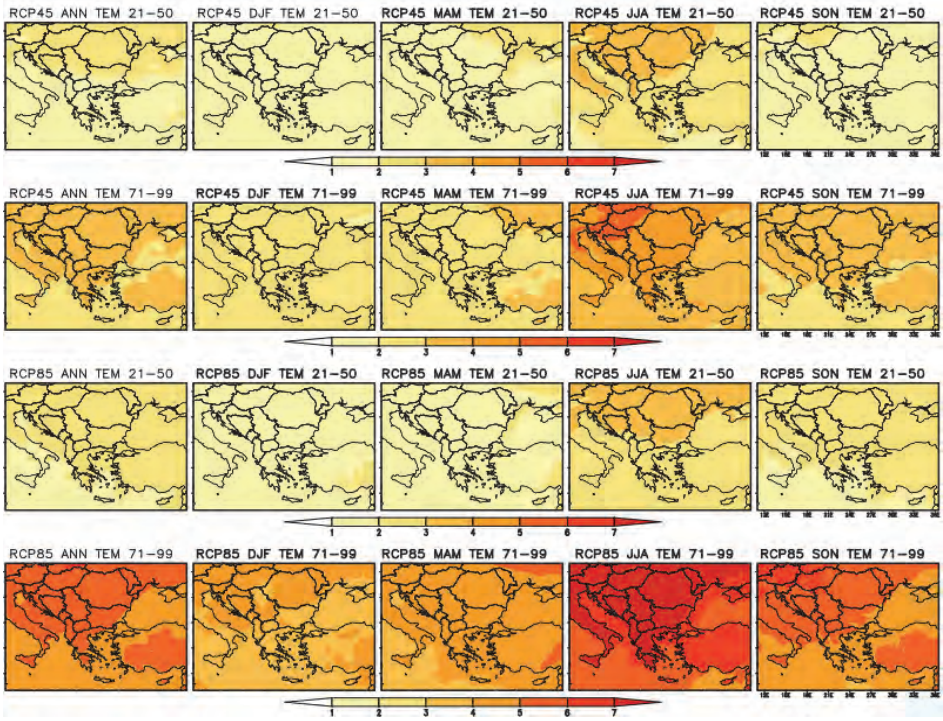

Fig. 4. Simulated annual and seasonal mean changes in temperature (in °C) with the regional climate model RegCM4-for the periods 2021-2050 and 2071-2099 according to the RCP4.5 (first two rows) and RCP8.5 (last two rows) scenarios compared with the reference period 1975–2004.

According to the RCP4.5 scenario, the annual temperature increase is between 1.5 ºC and 2.3 ºC in the first period and up to 3.5 ºC in the second period for the whole study area. During the first period 2021–2050, the greatest warming can be expected during the summer season between 2.5 ºC and 3 ºC. During the other seasons, the temperature rise is smaller, between 1.5 ºC and 2 ºC. During the second period 2071–2099, the temperature rises between 2 ºC and 2.5 ºC in the winter season and between 2.5 ºC and 3.5 ºC in spring and autumn. The temperature increase in summer can reach 5 ºC in the northern and northwestern parts of the region. According to the RCP8.5 scenario, the annual temperature increase is between 1.8 °C and 2.5 °C in the first period and between 4.2 °C and 5.8 °C in the second period for the whole region. During the first period 2021–2050, the greatest warming can be expected during the summer season between 2.5 °C and 3.5 °C. During the other seasons, the temperature rise is smaller, between 1.5 °C and 2.5 °C. During the second period

2071–2099, the temperature rise is between 3.5 °C and 4 °C in winter and spring and between 4.5 °C and 5.5 °C in autumn. The temperature increase in summer can reach 5–7 °C.

The simulations for convective precipitation above the used 24-hour thresholds are shown in *Figs. 5, 6, 7,* and *8*. They present changes between the future and the reference number of convective precipitation above the accepted threshold averaged per year (season).

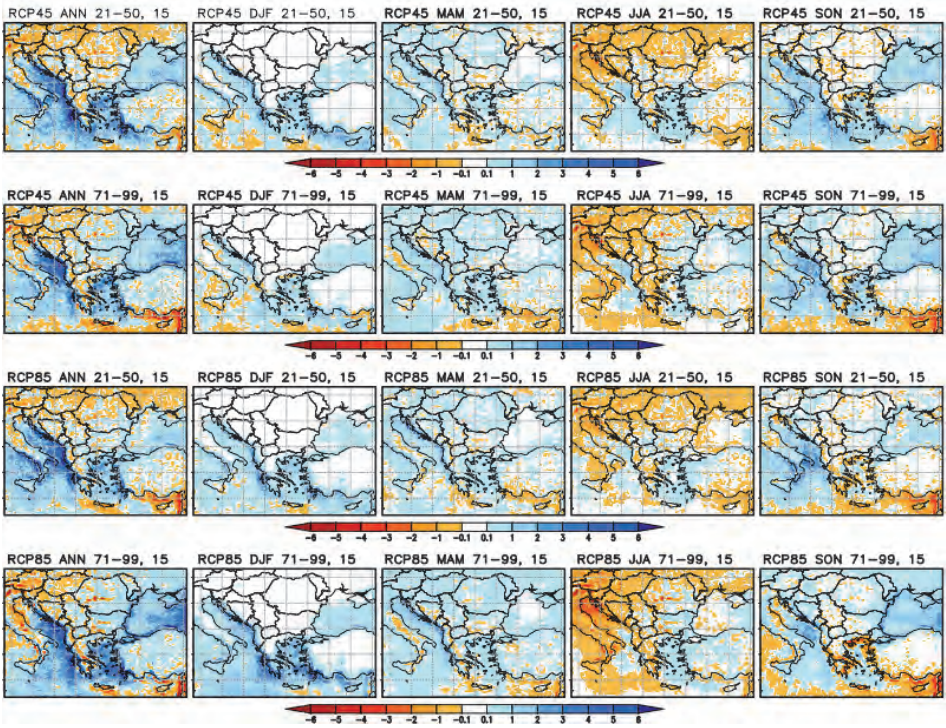

Fig. 5. Simulated annual and seasonal changes in the number of cases with 24-hour convective precipitation above the fixed threshold from 15 mm/24h averaged per a year (season) with the regional climate model RegCM4 for the periods 2021-2050 and 2071–2099 according to the RCP4.5 (first two rows) and RCP8.5 (last two rows) scenarios compared with the reference period 1975–2004.

Fig. 5 shows the annual and seasonal change in the number of cases with 24-hour convective precipitation above the threshold from 15 mm/24h averaged per year (season) for the periods 2021–2050 and 2071–2099 according to the

RCP4.5 and RCP8.5 scenarios compared with the reference period 1975–2004. The first column shows an increase in the number of cases of annual heavy convective precipitation along the eastern coasts of the Adriatic, Ionian, and Aegean Seas with 4–6 cases per year for both periods and for both scenarios and an increase with 1–2 cases over the half part of the continental areas. According to the RCP8.5 scenario, extreme rainfall can be expected to increase along the western coast of the Black Sea and also the Marmara Sea with 2–4 cases per years by the end of the century. A decrease in the number of cases of annual heavy convective rainfall can be expected in mountainous areas, especially in the eastern parts of the Alps, nevertheless the area holds the maximum precipitation total in the Alpine region according to the high-resolution observational precipitation dataset EURO4M (*Isotta et al.*, 2014). The number of cases of annual heavy convective precipitation decreases in the Carpathians and the Balkan Mountains by 3–4 cases per year by the end of the century. When looking at the seasons, an increase in extreme rainfall is shown along the Adriatic and Aegean coasts in the winter season and along the eastern coast of the Adriatic Sea in autumn by 1–2 cases per season according to the RCP4.5 and by 2–3 cases for the period 2071–2099 according to the RCP8.5 scenario. There is no change in the number of extreme convective rainfall cases in winter season over the continental part of the studied area. A reduction in the number of extreme convective rainfall events in mountainous areas is shown during the summer season with 3–4 cases in the eastern parts of Alps and the Carpathians according to the RCP8.5 scenario by the end of the century. In the summer season, there is an increase in the number of extreme precipitation events in some parts of the coastal areas. In spring, there is an increase in the number of extreme convective events by 1–2 cases in almost the whole study area and an increase by 2–3 cases along the eastern Adriatic coast for the period 2071–2099 according to the RCP8.5 scenario. For Bulgaria according to the RCP8.5 scenario, extreme precipitation events in the Danube plain and the Dobrudzha plateau are expected to increase with 1–2 cases per year by the end of the century and along the Black Sea coast with 3 events per year. There is an increase in extreme convective precipitation events along the Black Sea coast in the autumn season by 1–2 events and along the Danube plain and the Dobrudzha plateau with 1–2 events per season. A decrease in extreme precipitation in mountainous regions is observed in the summer season with 3–4 cases per season, especially in the high parts of the Rila-Rhodope region and the Balkan mountain according to the RCP8.5 scenario for the period 2071–2099. According to the Meteoalarm program, this threshold corresponds to ‘yellow’ code in Bulgaria.

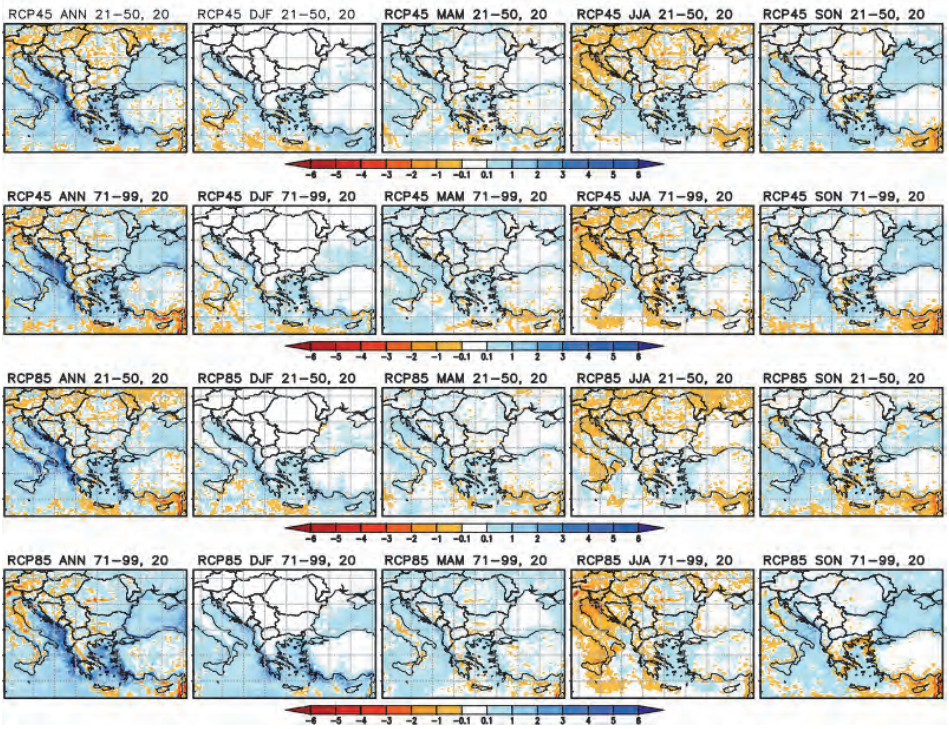

Fig. 6. Same as *Fig. 5*, but for the fixed threshold from 20 mm/24h.

Fig. 6 shows the annual and seasonal changes in the number of convective rainfall cases above the threshold of 20 mm/24h averaged per year (season). The first column shows an increase in the number of annual heavy precipitation events along the coasts of Adriatic, Ionian, and Aegean Seas with about 4–5 cases per year for both scenarios and both periods and Black Sea coast by 2–4 events according to RCP8.5 by the end of the century. In annual average, both RegCM simulations also depict an increase of extreme convective precipitation events over about half of the continental region, especially by the end of the century. There is a decrease in the number of annual heavy convective precipitation events in the continental parts of the studied area, especially over the mountainous regions (Carpathians, eastern parts of the Alps, Balkan Mountains, Rila-Rhodope region) by about 3–4 cases per year. When looking at the seasons, an increase in extreme rainfall is shown along the Adriatic and Aegean coasts in the winter season by 2–3 cases per season and along the eastern coast of the Adriatic Sea in autumn by 2–3 cases according to the RCP8.5 scenario by the end of the century. There is no change in the number of extreme convective precipitation events in winter over the continental part of the

area. In spring, there is an increase in extreme rainfalls with 1–2 cases along the Adriatic coast. A decrease in the number of extreme convective rainfall events is shown in mountainous areas during the summer season with 3 cases per season, especially in the eastern parts of the Alps and the Carpathians. In summer, there is also an increase in the number of extreme precipitation events in some parts of the coastal areas by 1–2 cases. According to the Meteoalarm program, this threshold corresponds to 'yellow' code in Hungary, Italy, and Slovenia.

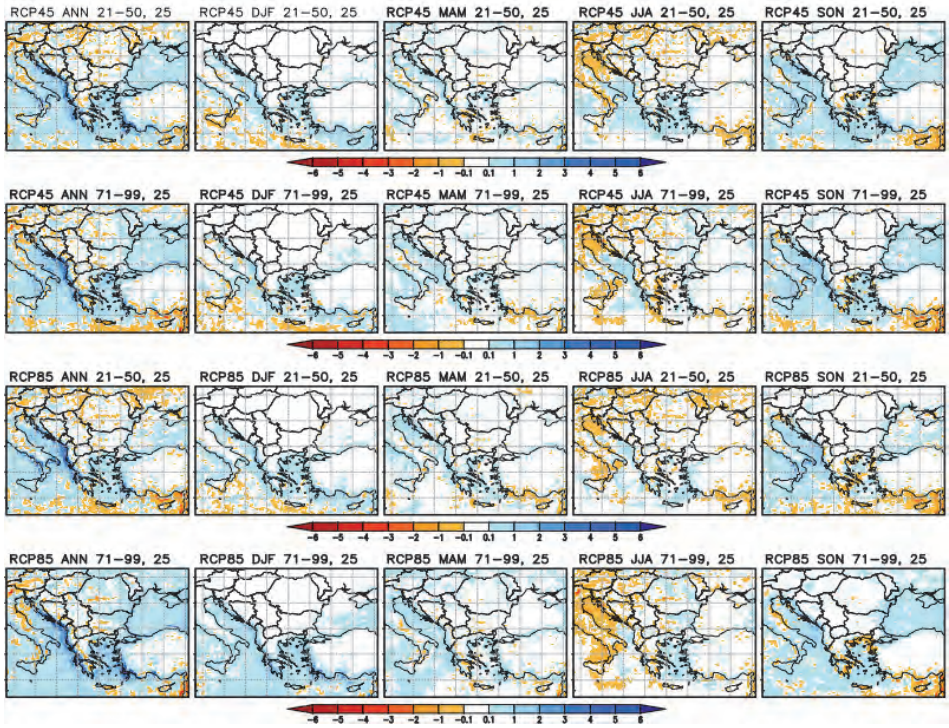

Fig. 7. Same as Fig. 5, but for the fixed threshold from 25 mm/24h.

Fig. 7 shows the annual and seasonal changes in the number of cases with 24-hour convective precipitation above the threshold from 25 mm/24h for the periods 2021–2050 and 2071–2099 according to the RCP4.5 and RCP8.5 scenarios compared with the reference period 1975–2004. Annual heavy precipitation events increase with 2–4 cases over the eastern coast of the Adriatic and Ionian Seas and western coast of Turkey. An increase in extreme rainfall cases is shown along the Adriatic and Aegean coasts in the winter season by 1–2 cases per season and along the eastern coast of the Adriatic Sea

and over the Black Sea in autumn by 1–2 cases for both periods and both scenarios. There is no visible change in the number of extreme convective events in winter over the continental part of the area. In summer and spring, there is an increase in extreme rainfalls with 1–2 cases in some parts of the coastal areas. Again, we can expect a decrease in the extreme rainfall cases over the mountains areas on annual basis and a decrease over the continental parts during the summer season. According to the Meteoalarm program, this threshold corresponds to 'yellow' code in Romania and Croatia.

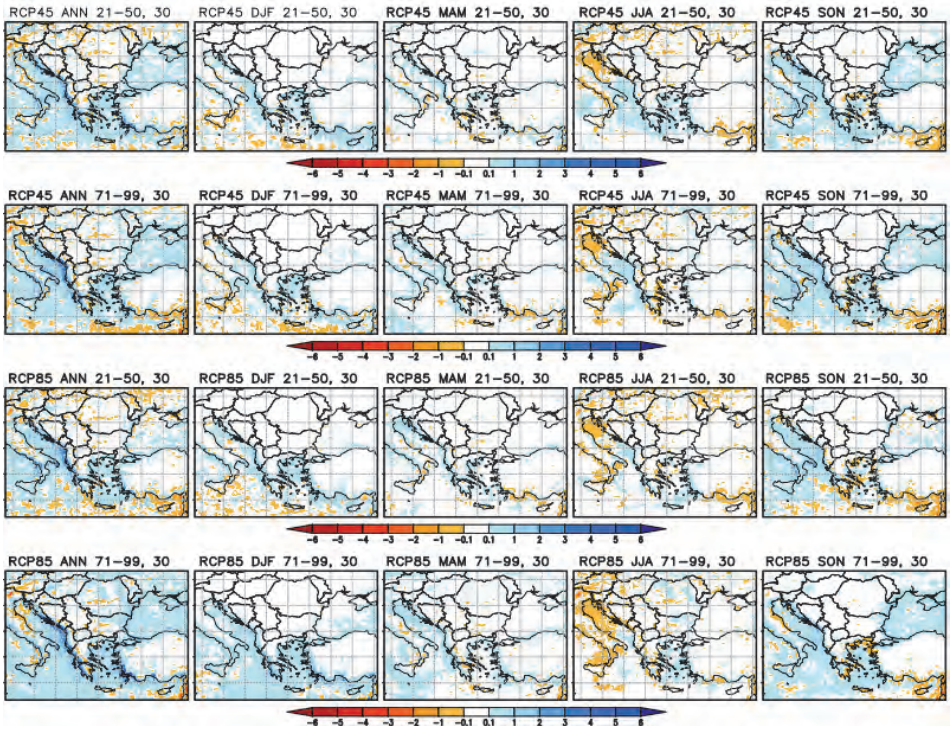

Fig. 8. Same as Fig. 5, but for the fixed threshold from 30 mm/24h.

Fig. 8 shows the annual and seasonal changes in the number of cases with 24-hour convective precipitation above the threshold from 30 mm per 24 hours averaged per year (season) for the periods 2021–2050 and 2071–2099 according to the RCP4.5 and RCP8.5 scenarios compared with the reference period 1975–2004. The first column shows an increase in the number of annual heavy convective rainfall cases along the coastline by 2–3 cases per year, especially along the eastern coast of the Adriatic Sea and the coast of Southern Italy, Greece, and Turkey for both scenarios and both periods. There is a decrease in

the number of annual heavy rainfall cases in the mountainous areas by 1–2 cases per year. When considering the seasons, an increase in extreme rainfalls are expected in the autumn and winter seasons along the eastern coast of the Adriatic Sea by 1–2 cases for both periods and both scenarios. According to the Meteoalarm program, this threshold corresponds to 'yellow' code in Serbia.

For both periods of climate change simulation, in both scenarios the number of heavy convective rainfalls decreases in the mountainous areas. The corresponding increase in water content is not enough to increase the number of intense convective precipitation events. This effect is expressed mainly in the summer when the number of convective and / or stratiform precipitation decreases. The decrease in the number of cases of heavy rainfall does not exclude the increase in the amount of precipitation in these areas due to the increased water content according to the law of Clausius – Clapeyron. For that reason, *Fig. 9* shows the annual and seasonal changes in the amount of convective precipitation according to the RCP8.5 and RCP4.5 scenarios in percentages by the end of the century.

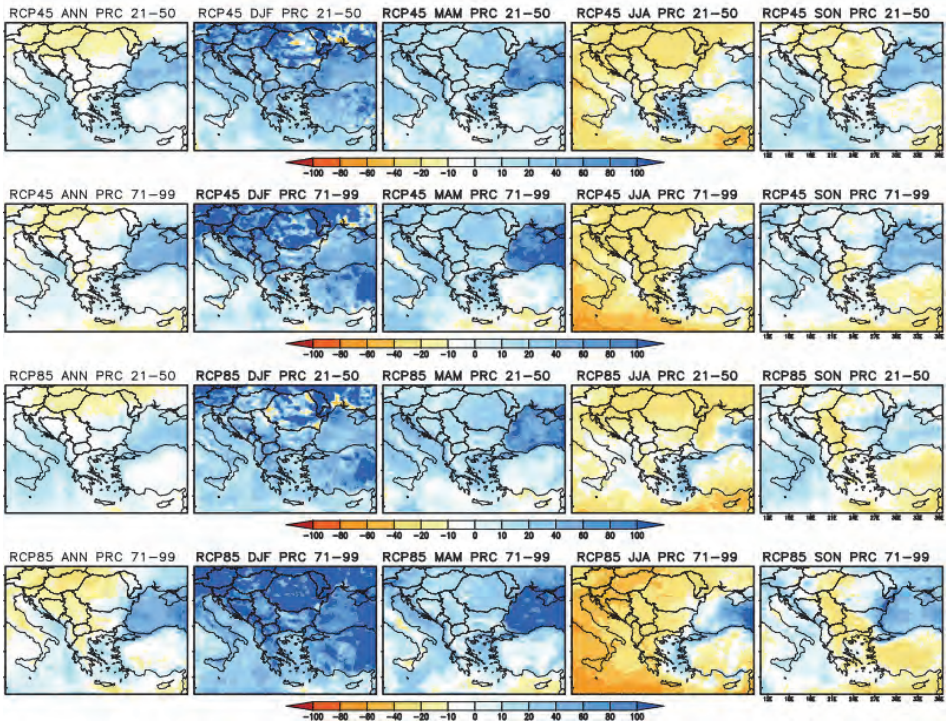

Fig. 9. Simulated annual and seasonal changes in the amount of convective precipitation (in %) with the regional climate model RegCM4 for the periods 2021–2050 and 2071–2099 according to the RCP4.5 (first two rows) and RCP8.5 (last two rows) scenarios compared with the reference period 1975–2004.

The first column of *Fig. 9* shows a decrease in the amount of the annual convective precipitation by 10–20% over the continental northwestern parts of the studied area and an increase in precipitation over seas, by 10–20% over the Adriatic and Aegean Seas, reaching 30–40% over the Black Sea. The most significant increase in convective rainfall is shown in the winter season according to the RCP8.5 scenario with almost 90% over the continental parts of the studied area for the both periods (2021–2050) and (2071–2099). Conversely, during the winter season there are no visible changes in the number of extreme rainfall cases above the 'yellow' code over the continental part of the domain (*Figs. 5*, *6*, *7*, and *8*). The amount of convective rainfall during the spring season also increases by 20–40% over the northern parts of the domain and especially over the Black Sea region by over 60%. During the summer season, the amount of precipitation decreases by 20–40% in almost the entire study area, except for the Aegean Sea and the eastern parts of the Black Sea. During the autumn season, there is a decrease in convective rainfall by 20–40% in the northwestern and southeastern continental parts of the region and an increase over the seas by 20–40%.

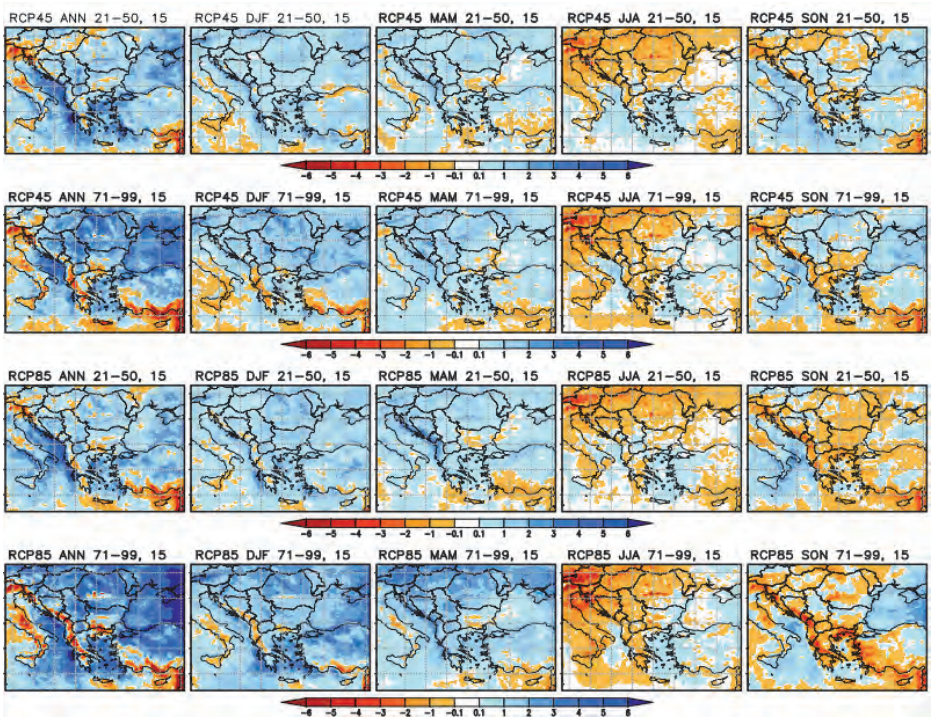

Fig. 10. Simulated annual and seasonal changes in the number of cases with 24-hour total precipitation above the fixed threshold from 15 mm/24h averaged per a year (season) with the regional climate model RegCM4 for the periods 2021–2050 and 2071–2099 according to the RCP4.5 (first two rows) and RCP8.5 (last two rows) scenarios compared with the reference period 1975–2004.

Due to the fact that the Meteoalarm thresholds are for total precipitation we have presented an additional information in *Figs. 10, 11, 12,* and *13* for the simulated annual (first columns) and seasonal (last four columns) changes in the number of cases with total precipitation above the fixed thresholds from 15, 20, 25, and 30 mm/24h, and also an information about the percentage (%) of the convective precipitation of total precipitation on *Fig. 14*.

Fig. 10 shows the simulated annual and seasonal changes in the number of cases with 24-hour total precipitation above the fixed threshold from 15 mm/24h for the periods 2021–2050 and 2071–2099 according to the RCP4.5 and RCP8.5 scenarios compared with the reference period 1975–2004 averaged per a year (season). The first column shows an increase in the number of extreme precipitation cases with 2–4 cases per year over the continental parts of the domain and in increase with 5–6 cases per year over the Adriatic, Ionian, Marmara, and Aegean Seas. There is an increase with 6–9 cases per year over the central part of the Black Sea by the end of the century. A decrease in the number of extreme rainfall can be expected over parts of eastern Alps, Dinaric, Pindus, Rila-Rhodope and Balkan Mountains, the southernmost parts of Turkey, and parts of Italy. When looking at the seasons there is an increase in extreme cases in winter and spring over almost the whole territory with 1–2 cases for both scenarios for the period 2021–2050 and 2–3 cases per season for the RCP8.5 scenario by the end of the century, a decrease in the summer season over the most parts of continental area of the studied domain, and an increase of extreme cases over half of domain in autumn. A reduction in the extreme rainfall is shown during the summer season with 4 to 6 cases, especially in the eastern parts of the Alps and the Carpathians according to the RCP8.5 scenario for the period 2071–2099, but also an increase in some parts of coastal areas.

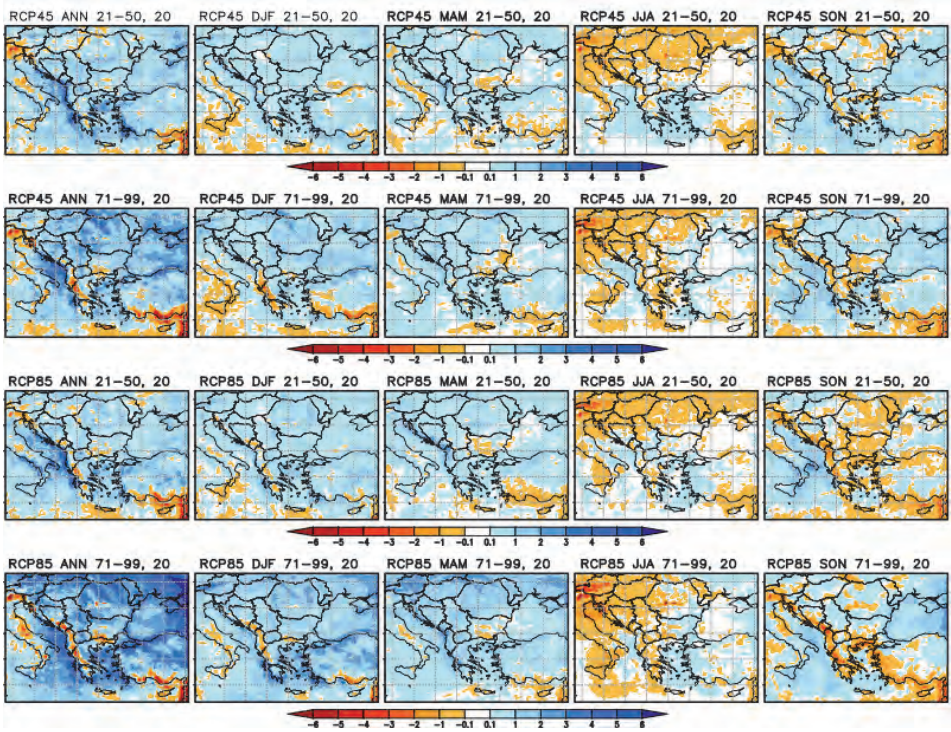

Fig. 11. Same as *Fig. 10*, but for the fixed threshold from 20 mm/24h.

Fig. 11 shows the simulated annual and seasonal changes in the number of cases with 24-hour total precipitation above the fixed threshold from 20 mm/24h averaged per a year (season) for the periods 2021–2050 and 2071–2099 according to the RCP4.5 (first two rows) and RCP8.5 (last two rows) scenarios compared with the reference period 1975–2004. The first column shows an increase in the number of annual heavy precipitation events over the continental parts of the studied area with 1–3 cases per year by 2050 and 4–5 cases by 2099, and an increase with 5–6 cases per year over the coastline according to both scenarios by the end of the century. A decrease in the number of extreme rainfalls is shown in the mountainons regions with 4–5 cases per year. In winter and spring an increase of extreme rainfall can be expected with 1–2 cases per season over most of the studied domain, an decrease in the number of extreme cases during the summer season, especially over the northern and northwestern parts of the domain, and in autumn over mountains areas.

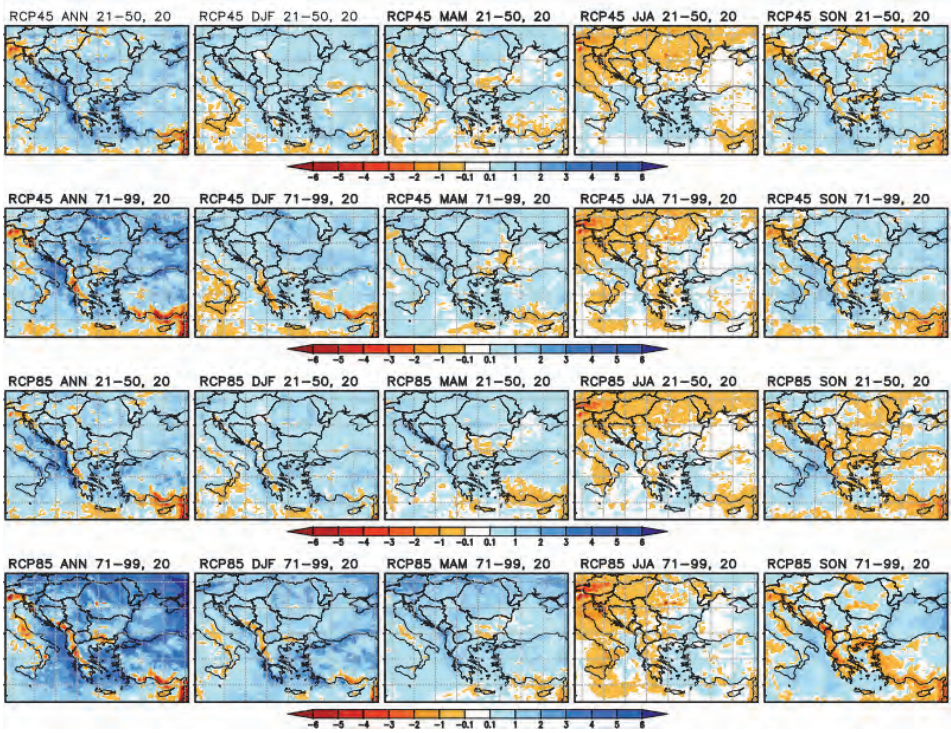

Fig. 12. Same as *Fig. 10*, but for the fixed threshold from 25 mm/24h.

Fig. 12 shows the annual and seasonal changes in the number of cases with 24-hour total precipitation above the threshold from 25 mm/24h for the periods 2021–2050 and 2071–2099 according to the RCP4.5 and RCP8.5 scenarios compared with the reference period 1975–2004. The annual heavy precipitation events increase with 2–4 cases over the continental parts and by 3–5 cases over the Aegean, Ionian, and the eastern coast of the Adriatic Seas. When looking at the seasons, there is an increase in the number of extreme rainfalls in winter and spring over almost the entire continental part of the domain, and a decrease in summer, especially over the northern and northwestern parts of the studied domain. In the autumn season, increase can be expected in the number of extreme rainfalls except in the mountains regions.

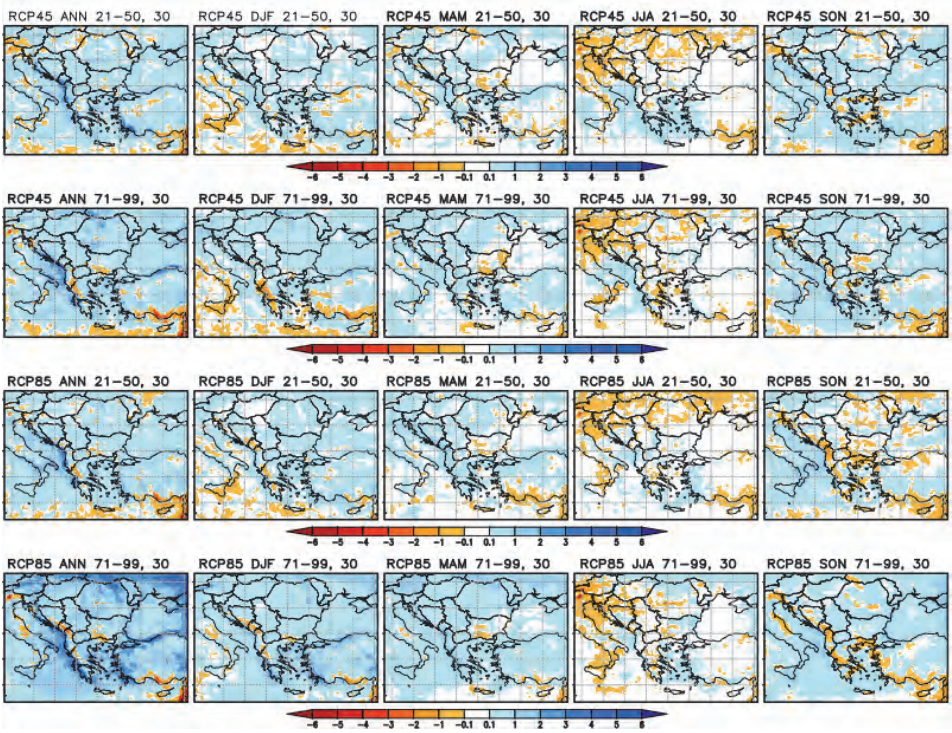

Fig. 13. Same as *Fig. 10*, but for the fixed threshold from 30 mm/24h.

Fig. 13 shows the annual and seasonal changes in the number of cases with 24-hour total precipitation above the threshold from 30 mm/24 hours averaged per year (season) for the periods 2021–2050 and 2071–2099 according to the RCP4.5 and RCP8.5 scenarios compared with the reference period 1975–2004. The first column shows an increase in the number of extreme events along the coastline with 2–3 cases per year, especially along the eastern coast of the Adriatic Sea and the coast of Southern Italy, Greece, and Turkey for both scenarios and both periods. An increase in extreme rainfalls is expected in the winter and spring seasons by 1–2 cases over most of the studied territory. A decrease in extreme rainfall is shown during the summer season in the northern and northwestern parts of the domain and an increase in the coastal areas.

The ratio of convective precipitation to total precipitation in the NCEP-NCAR analysis during the months of January, April, July, and October can be seen in *Myoung* and *Nielsen-Gammon* (2010). This ratio, obtained with the RegCM model by season is shown in *Fig. 14*.

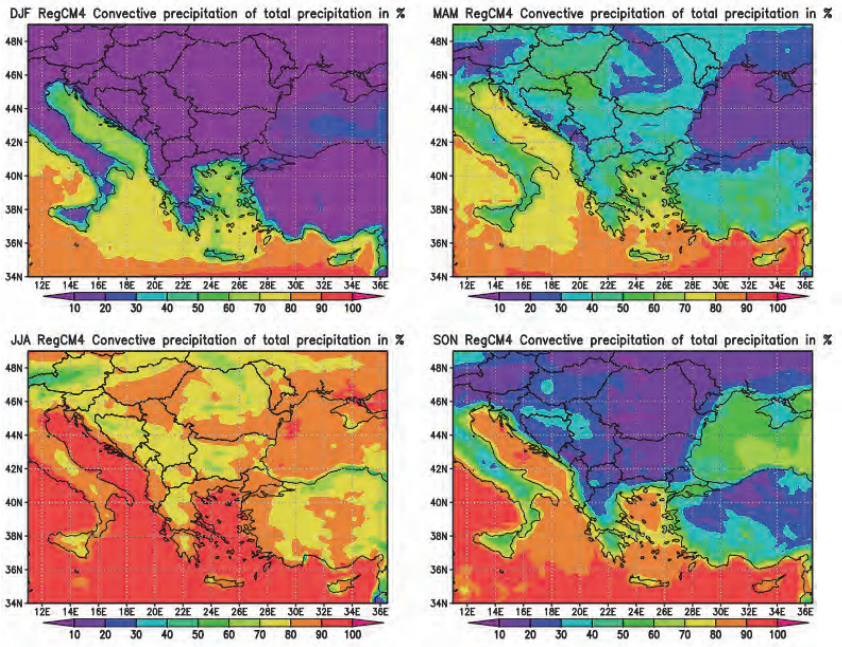

Fig. 14. Seasonal ratio of convective precipitation to total precipitation in % for the period 1975–2004.

Fig. 14 shows the seasonal ratio of convective precipitation to total precipitation in % for the period 1975–2004. In winter, the convective rainfall is 10% of the total rainfall over the continental part of the study area, with the exception of the coastal areas of the Adriatic, Ionian, and Aegean Seas, where the convective rainfall is about 20–50% of the total rainfall. In spring, the convective precipitation is 40–60% over the continental parts excluding mountains (20–30%) and 80–90% over the seas excluding the Black Sea (20–30%). In summer, 80–90% of the precipitation is convective except for the mountains (50–70%). In autumn, 10–30% of the precipitation is convective over the continental parts except over Italy and coastal areas (50–70%). In the annual rainfall (not shown here), between 80 and 90% of annual rainfall over the seas is convective except the Black Sea (between 30–50%). Over the continental parts of the domain, between 20 and 40% of the total precipitation is convective except the Adriatic, Ionian, and Aegean coasts (50–80%). For Bulgaria, according to the regional climate simulations, annual convective precipitation is 30–40% of the total precipitation for the whole territory: 40–50% for Hungary, 20–40% for Romania, 40–70% for Italy, 30–40% for Slovenia, 40–70% for Croatia, and 30–50% for Serbia.

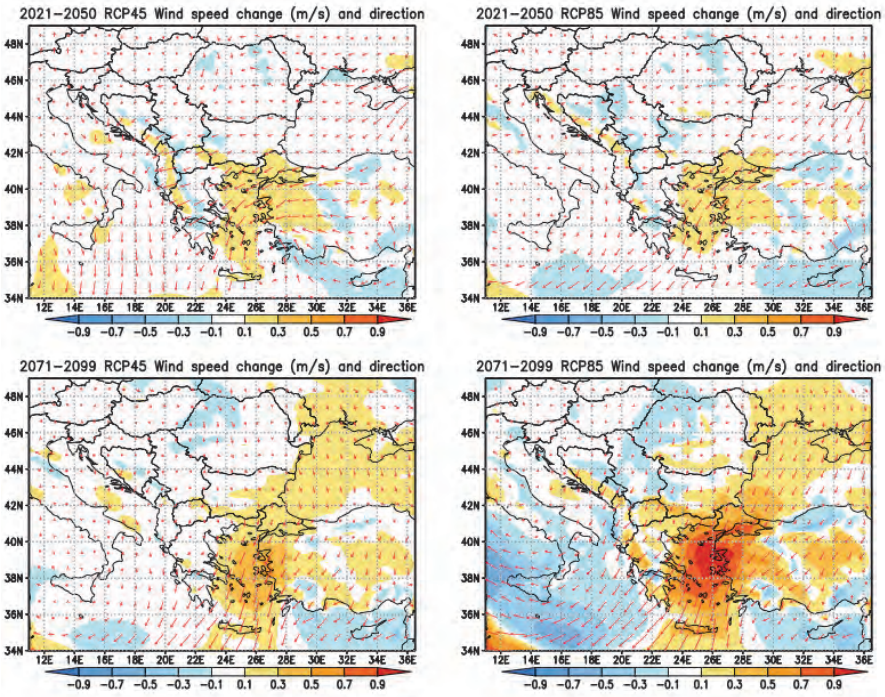

Fig. 15. Simulated annual mean changes of 10 m wind speed (m/s) and direction with the regional climate model RegCM4 for the periods 2021–2050 and 2071–2099 according to the RCP4.5 (first column) and RCP8.5 (second column) scenarios compared with the reference period 1975–2004. Wind direction and speed changes have been shown in vectors and shades, respectively.

Because of the strong increase of the extreme precipitation in the coastal area, we have also shown the simulated annual mean change of 10 m wind speed (m/s) and direction (*Fig. 15*) for the periods 2021–2050 and 2071–2099 according to the RCP4.5 (first column) and RCP8.5 (second column) scenarios compared with the reference period 1975–2004. The wind direction and speed change have been shown in vectors and shades, respectively. In the period 2021–2050, an increase in the annual wind speed of 10 m by 0.1–0.3 m/s is observed mainly in the coastal areas of the Aegean and Marmara Seas, parts of the eastern coast of the Adriatic Sea, and parts of western Turkey under both scenarios. In the period 2071–2099, an increase of 0.1–0.3 m/s is observed over the Black and Marmara Seas and by 0.3–0.5 m/s over the Aegean Sea under the RCP4.5 scenario. According to the RCP8.5 scenario, the increase is 0.3–0.5 m/s over the western Black Sea coast and parts of the eastern Adriatic coast, and 0.7–0.9 m/s over the Aegean and Marmara Seas.

4. Conclusions

The thresholds used by the Meteoalarm program were used as a measure of change in the hazardous precipitation over the studied domain. The accepted threshold values for 'yellow' code accepted in the countries from the district used in this study were: Bulgaria (15 mm/24h), Croatia (25 mm/24h), Hungary (20 mm/24h), Italy (20 mm/24h), Romania (25 mm/24h), Serbia (30 mm/24h), and Slovenia (20 mm/24h). Overall, it can be concluded that it is possible to identify areas with an increased risk of heavy rainfall using the Meteoalarm criteria.

According to the regional climate simulations with 20 km resolution, an increase in the number of hazardous total precipitation events can be expected in the coastal areas for both scenarios and for both periods, especially in the coastal areas of the Adriatic, Ionian, Aegean, Black, and Marmara Seas. In general, the number of extreme precipitation events can be expected to decrease over the mountains in this region on annual basis (eastern parts of the Alps, Carpathians, Dinaric Mountains, Pindus Mountains, Balkan Mountains, and Rila-Rhodopes Mountains). An increase in the number of dangerous precipitation cases can be expected in the winter and spring season, for all thresholds, an increase in the autumn season over the half continental part of the studied area, a decrease in summer season over the continental parts of the domain, and an increase in summer in some parts of the coastal areas.

Overall, the number of extreme convective precipitation cases above the accepted thresholds from 15, 20, 25, and 30 mm for 24-hour increase for both scenarios and both periods in the coastal areas and decrease over the mountains on annual basis. In the winter season, there is no change in the number of extreme convective rainfall cases over the continental part of the studied area. The reason for this is that simulations show that the winter convective precipitation is about 10% of the total precipitation in the continental parts of the study area. An increase in the extreme rainfall cases is shown along the Adriatic and Aegean coasts in the winter season and along the eastern coast of the Adriatic Sea in autumn for both periods, both scenarios, and all thresholds. In spring, there is an increase in the number of extreme convective events in almost the whole study area especially along the eastern Adriatic coast (cases above 15 and 20 mm/24h) and along the coastal areas (cases above 25 and 30 mm/24h). A reduction in the number of extreme convective rainfall events is shown in the mountainous areas during the summer season for all periods and all thresholds.

According to the regional climate simulations, between 20 and 40% of the annual precipitation is convective except for the Adriatic, Ionian, and Aegean coasts (50–80%). In the winter season, about 10% of the total rainfall is convective over the continental part of the studied area, with the exception of the coastal areas of the Adriatic, Ionian, and Aegean Seas, where the convective rainfall is about 20–50% of the total rainfall. In spring, 40–60% of the

precipitation is convective over the continental parts excluding the mountainons regions (20–30%) and over the seas (80–90%) excluding the Black Sea (20–30%). In the summer season, about 80–90% of the precipitation is convective except for the mountains (50–70%). In autumn, 10–30% of the precipitation is convective over the continental parts except for Italy and coastal areas (50–70%).

Because of the strong increase of extreme precipitation in the coastal area, we have also presented spatial maps of the simulated annual mean change of the 10 m wind. An increase in the annual wind speed can be expected by 0.1–0.3 m/s, mainly over the coastal areas for the period 2021–2050 for both scenarios and by 0.3–0.5 m/s for the period 2071–2099 under the RCP4.5 scenario. According to the RCP8.5 scenario, an increase can be expected by 0.3–0.5 m/s over the western coast of the Black Sea, parts of the eastern coast of the Adriatic Sea, and by 0.7–0.9 m/s over the Aegean and Marmara Seas for the period 2071–2099.

Acknowledgments: This research was funded by the Bulgarian National Science Fund through contract № КП-06-М 57/3-16.11.2021. We acknowledge the E-OBS dataset from the EU-FP6 project UERRA (https://www.uerra.eu) and the Copernicus Climate Change Service, and the data providers in the ECA&D project (https://www.ecad.eu). We thank the Abdus Salam International Centre for Theoretical Physics (ICTP) and the Earth System Physics (ESP) group for providing free-of-charge RegCM4 software and HadGEM2 data.

References

Alexander, L.V., 2016: Global observed long-term changes in temperature and precipitation extremes: A review of progress and limitations in IPCC assessments and beyond. *Weather Climate Extr. 11*, 4–16, https://doi.org/10.1016/j.wace.2015.10.007

Arakawa, A. and *Schubert, W.H.,* 1974: Interaction of cumulus cloud ensemble with the largescale environment, Part I. *J. Atmos. Sci. 31*, 674–701. https://doi.org/10.1175/1520-0469(1974)031<0674:IOACCE>2.0.CO;2

Berg, P., Moseley, C., and *Haerter, J.O.,* 2013: Strong increase in convective precipitation in response to higher temperatures. *Nat. Geosci. 6*, 181–185. https://doi.org/10.1038/ngeo1731

Bergant, K.; Belda, M.; and *Halenka, T.,* 2007: Systematic errors in the simulation of European climate (1961–2000) with RegCM3 driven by NCEP/NCAR reanalysis. *Int. J. Climatol. 27*, 455–472. https://doi.org/10.1002/joc.1413

Chernokulsky, A., Kozlov, F., Zolina, O., Bulygina, O., Mokhov, I., and *Semenov, V.*, 2019: Observed changes in convective and stratiform precipitation in Northern Eurasia over the last five decades. *Environ. Res. Lett. 14*, 045001. https://doi.org/10.1088/1748-9326/aafb82

Clarke, L., Edmonds, J., Krey, V., Richels, R., Rose, S., and *Tavoni, M.,* 2010: International climate policy architectures: overview of the EMF 22 international scenarios. *Energ. Econ. 31,* (suppl. 2): S64–S81. https://doi.org/10.1016/j.eneco.2009.10.013

Collins, W.J., Bellouin, N., Doutriaux-Boucher, M., Gedney, N., Halloran, P., Hinton, T., Hughes, J. Jones, C.D., Joshi, M., Liddicoat, S., Martin, G., O'Connor, F., Rae, J., Senio,r C., Sitch, S., Totterdell, I., Wiltshire, A., and *Woodward, S.*, 2011: Development and evaluation of an Earth-system model – HadGEM2, *Geosci. Model Dev. Discuss., 4*, 997–1062. https://doi.org/10.5194/gmdd-4-997-2011

Coppola, E., Nogherotto, R., Ciarlo', J., Giorgi, F., Meijgaard, E., Kadygrov, N., Iles, C., Corre, L., Sandstad, M., Somot, S., Nabat, P., Vautard, R., Levavasseur, G., Schwingshackl, C., Sillmann, J., Kjellström, E., Nikulin, G., Aalbers, E., Lenderink, G., Christensen, O., Boberg, F., Sørland,

S., Demory, M., Bülow, K., Teichmann, C., Warrach-Sagi, K., and *Wulfmeyer, V.*, 2021: Assessment of the European climate projections as simulated by the large EURO-CORDEX regional and global climate model ensemble. Journal of Geophysical Research: *Atmospheres, 126(4)*, e2019JD032356. https://doi.org/10.1029/2019jd032356

Cornes, R., G. van der Schrier, E.J.M. van den Besselaar, and *P.D. Jones.,* 2018: An Ensemble Version of the E-OBS Temperature and Precipitation Datasets, *J. Geophys. Res. Atmos. 123*. 9391–9409. https://doi.org/10.1029/2017JD028200

Dickinson, R., Henderson-Sellers, A., and *Kennedy, P.,* 1993: Biosphere-Atmosphere Transfer Scheme (BATS) version 1 as coupled to the NCAR community climate model. NCAR Technical Note NCAR/TN-387 + STR. http://dx.doi.org/10.5065/D67W6959

Dourte, D.R., Fraisse, C.W., and *Bartels, W.L.,* 2015: Exploring changes in rainfall intensity and seasonal variability in the Southeastern U.S.: Stakeholder engagement, observations, and adaptation. *Climate Risk Manage. 7,* 11–19. https://doi.org/10.1016/j.crm.2015.02.001

Elguindi, N., Bi, X., Giorgi, F., Nagarajan, B., Pal, J., Solmon, F., Rauscher, S., Zakey, A., O'Brien, T., Nogherotto, R., and *Giuliani G.,* 2014: Regional Climate Model RegCM User Manual Version 4.4; International Centre for Theoretical Physics (ICTP), Trieste, Italy.

Fougères, A.-L., de Haan, L., and *Mercadier, C.,* 2015: Bias correction in multivariate extremes. *Ann. Statist. 43* (2) 903–934. https://doi.org/10.1214/14-AOS1305

Giorgi, F., Bates, G.T., and *Nieman, S.,* 1993a: The multi-year surface climatology of a regional atmospheric model over the Western United States. *J. Climate 6,* 75−95. https://doi.org/10.1175/1520-0442(1993)006<0075:TMSCOA>2.0.CO;2

Giorgi, F., Marinucci, M.R., and *Bates, G.T.,* 1993b: Development of a second generation regional climate model (RegCM2). Part I: Boundary layer and radiative transfer processes. *Mon. Weather Rev. 121,* 2794−2813. https://doi.org/10.1175/1520-0493(1993)121<2794:DOASGR>2.0.CO;2

Giorgi, F., Coppola, E., Solmon, F., Mariotti, L., Sylla, M.B ; Bi, X., Elguindi, N., Diro, G.T ., Nair, V., Giuliani, G., Turuncoglu, U.U., Cozzini, S., Güttler, I., O'Brien, TA., Tawfik, A.B., Shalaby, A., Zakey, A.S., Steiner, A.L., Stordal, F., Sloan, L.C., and *Brankovic, C.,* 2012: RegCM4: model description and preliminary tests over multiple CORDEX domains. *Clim. Res. 52,* 7–29. https://doi.org/10.3354/cr01018

Giorgi, F., Torma, C., Coppola, E., Ban, N., Schär, C., and *Somot, S.,* 2016: Enhanced summer convective rainfall at Alpine high elevations in response to climate warming. *Nature Geosci. 9*, 584–589 https://doi.org/10.1038/ngeo2761

Grell, G., Dudhia, J., and *Stauffer, D.R.,* 1994: A description of the fifth generation Penn State/NCAR Mesoscale Model (MM5). NCAR Tech Note NCAR/TN-398 + STR, NCAR, Boulder, CO.

Güttler, I., Branković, Č., O'Brien, T.A., Coppola, E., Grisogono, B., & Giorgi, F., 2014: Sensitivity of the regional climate model RegCM4.2 to planetary boundary layer parameterisation. *Climat. Dyn. 43*, 1753–1772, https://doi.org/10.1007/s00382-013-2003-6

Hawcroft, M., Walsh, E., Hodges, K., and *Zappa, G.,* 2018: Significantly increased extreme precipitation expected in Europe and North America from extratropical cyclones. *Environ. Res. Lett. 13,* 124006. https://doi.org/10.1088/1748-9326/aaed59

Houze, R.A. Jr., 2012: Orographic effects on precipitating clouds. *Rev. Geophys., 50,* RG1001. https://doi.org/10.1029/2011RG000365

Hurford, A., D.J. Parker, S.J. Priest, and *D.M. Lumbroso*, 2012: Validating the return period of rainfall thresholds used for Extreme Rainfall Alerts by linking rainfall intensities with observed surface water flood events. *J. Flood Risk Manage. 5,* 134–142. https://doi.org/10.1111/j.1753-318X.2012.01133.x

IPCC, 2012: *Managing the Risks of Extreme Events and Disasters to Advance Climate Change Adaptation.* A Special Report of Working Groups I and II of the Intergovernmental Panel on Climate Change [Field, C.B., V. Barros, T.F. Stocker, D. Qin, D.J. Dokken, K.L. Ebi, M.D. Mastrandrea, K.J. Mach, G.-K. Plattner, S.K. Allen, M. Tignor, and P.M. Midgley (eds.)], Cambridge University Press, Cambridge, UK, and New York, NY, USA.

IPCC, 2021: Climate Change 2021: The Physical Science Basis. Contribution of Working Group I to the Sixth Assessment Report of the Intergovernmental Panel on Climate Change. (eds. *Masson-Delmotte, V., P. Zhai, A. Pirani, S.L. Connors, C. Péan, S. Berger, N. Caud, Y. Chen, L.*

Goldfarb, M.I. Gomis, M. Huang, K. Leitzell, E. Lonnoy, J.B.R. Matthews, T.K. Maycock, T. Waterfield, O. Yelekçi, R. Yu, and B. Zhou). Cambridge University Press, Cambridge, United Kingdom and New York, NY, USA. doi:10.1017/9781009157896

Isotta, F.A., Frei, C., Weilguni, V., Tadić, M.P., Lassègues, P., Rudolf, B., Pavan, V., Cacciamani, C., Antolini, G., Ratto, S.M., Munari, M, Micheletti, S., Bonati, V., Lussana, C., Ronchi, C., Panettieri, E., Marigo, G., and *Vertačnik, G.*, 2014: The climate of daily precipitation in the Alps: Development and analysis of a high-resolution grid dataset from pan-Alpine rain gauge data. *Int. J. Climatol. 34*, 1657–1675. https://doi.org/10.1002/joc.3794

Jacob, D., Petersen, J., Eggert, B., Alias, A., Christensen, O.B., Bouwer, L.M., Braun, A., Colette, A., Déqué, M.,Georgievski, G., Georgopoulou, E., Gobiet, A., Menut, L., Nikulin, G., Haensler, A., Hempelmann, N., Jones, C., Keuler, K., Kovats, S., Kröner, N., Kotlarski, S., Kriegsmann, A., Martin, E., van Meijgaard, E., Moseley, C., Pfeifer, S., Preuschmann, S., Radermacher, C., Radtke, K., Rechid, D., Rounsevell, M., Samuelsson, P., Somot, S., Soussana, JF., Teichmann, C., Valentini, R., Vautard, R., Weber, B., and *Show, P.Y.*, 2014: EURO-CORDEX: new high-resolution climate change projections for European impact research. *Reg. Environ. Change 14*, 563–578, https://doi.org/10.1007/s10113-013-0499-2

Jeon, S., Paciorek, C.J., Wehner, M.F., 2016: Quantile-based Bias Correction and Uncertainty Quantification of Extreme Event Attribution Statements. *Weather Climate Extr. 12*, 24–32. https://doi.org/10.1016/j.wace.2016.02.001

Kiehl, J., Hack, J., Bonan, G., Boville, B., Breigleb, B., Williamson, D. and *Rasch, P.*, 1996: Description of the NCAR community climate model (CCM3). Technical report, National Center for Atmospheric Research.

Kirshbaum, D.J., B. Adler, N. Kalthoff, C. Barthlott, and *S. Serafin*, 2018: Moist Orographic Convection: Physical Mechanisms and Links to Surface-Exchange Processes. *Atmosphere 9*(3), 80. https://doi.org/10.3390/atmos9030080

Kotlarski, S., Keuler, K., Christensen, O.B., Colette, A., Déqué, M., Gobiet, A., Goergen, K., Jacob, D., Lüthi, D., van Meijgaard, E., Nikulin, G., Schär, C., Teichmann, C., Vautard, R., Warrach-Sagi, K., and *Wulfmeyer, V.*, 2014: Regional climate modeling on European scales: a joint standard evaluation of the EURO-CORDEX RCM ensemble. *Geosci. Model Dev. 7*,1297–1333. https://doi.org/10.5194/gmd-7-1297-2014

Luo, M., Liu, T., Meng, F., Duan, Y., Frankl, A., Bao, A., and *De Maeyer, P.*, 2018: Comparing Bias Correction Methods Used in Downscaling Precipitation and Temperature from Regional Climate Models: A Case Study from the Kaidu River Basin in Western China. *Water 10(8),* 1046. https://doi.org/10.3390/w10081046

Moss, R.H., Edmonds, J.A., Hibbard, K.A., Manning, M.R., Rose, S.K., van Vuuren, D.P., Carter, T.E., Emori, S., Kainuma, M., Kram, T., Meehl, G.A., Mitchell, J.F.B., Nakicenovic, N., Riahi, K., *Smith, S.J., Stouffer, R.J., Thomson, A.M., Weyant, J.P.,* and *Wilbanks, .J.*, 2010: The next generation of scenarios for climate change research and assessment. *Nature 463*, 747–756. https://doi.org/10.1038/nature08823

Myhre, G., K. Alterskjær, C.W. Stjern, Ø. Hodnebrog, L. Marelle, B.H. Samset, J. Sillmann N. Schaller, E. Fischer, M. Schulz, and *A. Stohl,* 2019: Frequency of extreme precipitation increases extensively with event rareness under global warming. *Sci. Rep. 9*, 16063. https://doi.org/10.1038/s41598-019-52277-4

Myoung, B. and *J.W. Nielsen-Gammon,* 2010: Sensitivity of monthly convective precipitation to environmental conditions. *J. Climate, 23*, 166–188. https://doi.org/10.1175/2009JCLI2792.1

Pal, J.S., E.E. Small, and *E.A.B. Eltahir,* 2000: Simulation of regional-scale water and energy budgets: Representation of subgrid cloud and precipitation processes within RegCM. *J. Geophys. Res.-Atmos. 105*(D24), 29579–29594. https://doi.org/10.1029/2000JD900415

Park, I-H. and *Seung-Ki, M.,* 2017: Role of Convective Precipitation in the Relationship between Subdaily Extreme Precipitation and Temperature, *J. Climate 30* AMS, 9527–9537. https://doi.org/10.1175/JCLI-D-17-0075.1

Pieczka, I., Pongrácz, R., André, K., Kelemen, F.D., and *Bartholy, J.*, 2016: Sensitivity analysis of different parameterization schemes using RegCM4.3 for the Carpathian Region. *Theor. Appl. Climatol. 130*, 1175–1188. https://doi.org/10.1007/s00704-016-1941-4

Riahi, K., S. Rao, V. Krey, C. Cho, V. Chirkov, G. Fischer, G. Kindermann, N. Nakicenovic, P. Rafaj, 2011: RCP8.5 scenario of comparatively high greenhouse gas emissions. *Climatic Change 109*, 33–57. doi 10.1007/s10584-011-0149-y.

Schär, C., Ban, N., Fischer, E.M., Rajczak, J., Schmidli, J., Frei, C., Giorgi, F., Karl, T.R., Kendon, E.J., Tank, A.M., G. Klein; O'Gorman, P.A.; S. Jana; Z. Xuebin, and *Zwiers, F.W.*, 2016: Percentile indices for assessing changes in heavy precipitation events. *Climatic Change 137*, 201–216. https://doi.org/10.1007/s10584-016-1669-2

Shi, X., Durran, D., 2016: Sensitivities of Extreme Precipitation to Global Warming Are Lower over Mountains than over Oceans and Plains. *Journal of Climate, 29(13)*, 4779–4791. doi:10.1175/JCLI-D-15-0576.1

Somot, S., Ruti, P., Ahrens, B., Coppola, E., Jordà, G., Sannino, G., and *Solmon, F.*, 2018: Editorial for the Med-CORDEX special issue. *Climate Dynam. 51*, 771–777. https://doi.org/10.1007/s00382-018-4325-x

Spiridonov,V. and *Balabanova, S.*, 2021: Chapter 9 - The impact of climate change on intensive precipitation and flood types in Bulgaria, Editor(s): Mărgărit-Mircea Nistor, Climate and Land Use Impacts on Natural and Artificial Systems1, Elsevier, 153–169. https://doi.org/0.1016/B978-0-12-822184-6.00001-6

Taylor, C., 2021: An Introduction to Hypothesis Testing. ThoughtCo, Aug. 6, 2021, thoughtco.com/introduction-to-hypothesis-testing-3126336

Thomson, A.M., Calvin, K.V., Smith, S.J., G. Page Kyle, April Volke, Pralit Patel, Sabrina Delgado-Arias, Ben Bond-Lamberty, Marshall A. Wise, Leon E. Clarke & James A. Edmonds, 2011: RCP4.5: A pathway for stabilization of radiative forcing by 2100. *Climatic Change 109*, 77 https://doi.org/10.1007/s10584-011-0151-4

Torma, C., Coppola, E., Giorgi, F., Bartoly, J., Pongracz, R., 2011: Validation of a high resolution version of the regional climate model RegCM3 over the Carpathian basin. *J. Hydrometeorol. 12*, 84–100. https://doi.org/10.1175/2010JHM1234.1

Trenberth, K., 2011: Changes in precipitation with climate change. *Climate Res. 47*, 123–138. https://doi.org/10.3354/cr00953

Turco, M., Llasat, M.C., Herrera, S., and *Gutiérrez, J.M.*, 2017: Bias correction and downscaling of future RCM precipitation projections using a MOS-Analog technique. *J. Geophys. Res. Atmos. 122*, 2631–2648. https://doi.org/10.1002/2016JD025724

Valcheva, R. and *E. Peneva*, 2014: Sensitivity to the parametrization of cumulus convection in the RegCM4.3 simulations focused on Balkan Peninsula and Bulgaria, *Annual of Sofia University "St. Kliment Ohridski", Faculty of Physics 107*, 113–131.

van Vuuren, D.P., Edmonds, J., Kainuma, M., Riahi, K., Thomson, A., Hibbard, K., Hurtt, G.C,. Kram, T., Krey, V., Lamarque, J.F., Masui, T., Meinshausen, M., Nakicenovic, N., Smith, S.J., Rose, S.K., 2011: The representative concentration pathways: an overview. *Climatic Change 109*, 5. https://doi.org/10.1007/s10584-011-0148-z

Vautard, R., Kadygrov, N., Iles, C., Boberg, F., Buonomo, E., Bülow, K., Coppola, E., Corre, L., van Meijgaard, E., Nogherotto, R., Sandstad, M., Schwingshackl, C., Somot, S., Aalbers, E., Christensen,O.B., Ciarlo, J.M., Demory, M.E., Giorgi, F., Jacob, D., Jones, R.G., Keuler, K., Kjellström, E., Lenderink, G., Levavasseur, G., Nikulin, G., Sillmann, J., Solidoro, C., Sørland, S.L., Steger, C., Teichmann, C., Warrach-Sagi, K., Wulfmeyer, V., 2021: Evaluation of the large EURO-CORDEX regional climate model ensemble. *J. Geophys. Res.: Atmos. 126*, e2019JD032344. https://doi.org/10.1029/2019JD032344

Westra, S., H.J. Fowler, J.P. Evans, L.V. Alexander, P. Berg, F. Johnson, E.J. Kendon, G. Lenderink, and *N.M. Roberts,* 2014: Future changes to the intensity and frequency of shortduration extreme rainfall. *Rev. Geophys. 52*, 522–555. https://doi.org/10.1002/2014RG000464

Westra, S., L.V. Alexander, and *F.W. Zwiers,* 2013, Global Increasing Trends in Annual Maximum Daily Precipitation. *J. Climate 26*, 3904–3918. https://doi.org/10.1175/JCLI-D-12-00502.1

WMO – World Meteorological Organization, 2016: Guidelines on the definition and monitoring of extreme weather and climate events. Draft version – first review by TT-DEWCE (Dec 2015). http://www.wmo.int/pages/prog/wcp/ccl/opace/opace2/documentsDraftversionoftheGuidelinesontheDefinitionandMonitoringofExtremeWeatherandClimateEvents.pdf

DOI:10.28974/idojaras.2020.1.6

IDŐJÁRÁS

Quarterly Journal of the Hungarian Meteorological Service
Vol. 127, No. 1, January – March, 2023, pp. 107–122

Investigation of the location of an immission measuring point in an urban environment

Georgina Tóth-Nagy* and **Fruzsina Németh**

Sustainable Solution Research Laboratory
Faculty of Engineering, University of Pannonia
10 Egyetem St., Veszprem, Hungary H-8200

**Corresponding author E-mail: nagy.georgina@almos.uni-pannon.hu*

(Manuscript received in final form January 12, 2022)

Abstract— Life could not exist on Earth without air; this is why its protection is so important. However, air pollution has been known since ancient times, nowadays pollutants from anthropogenic sources occur in much higher quantities. Previously, the primary emission sources were factories due to the industrial revolution, then the development of transportation and the presence of internal-combustion engines made air pollution a major issue. Therefore, more and more efforts have been made over the last decades to reduce the emissions of air pollutants in the industrial sector and the everyday life of the population. Because of this, it is essential to know the factors influencing the air quality of the settlement and to monitor the pollutants properly. Therefore, within the framework of the research work, we examined the possibilities of placing an immission measuring point. To do that, we needed to explore the most important characteristics of the town. Therefore, we examined its structure, meteorological and climatic factors, which fundamentally affect the air quality. We made immission maps using a Geographical Information Program (QGIS) based on the received data. Finally, based on the results, we examined the possibilities of placing an immission measuring station.

Key-words: air pollution, air quality, immission, sensor, particulate matter, QGIS

1. Introduction

In recent decades, environmental protection has become increasingly important to humanity. Within this, the most frequently mentioned topics include water quality protection, soil protection, waste management, wastewater treatment and, last but not least, the protection of ambient air. The atmosphere is made up of gases and liquid and solid particles in different proportions, and the processes between them affect our lives (*Kinney*, 2008; *Kampa* and *Castanas*, 2008; *Gurjar et al*., 2010). From a biological point of view, it is one of the most critical components of our metabolism (*Kim et al.*, 2013), so its protection plays an extremely important role. The appearance of air pollution dates back a long time; it can be linked to man's appearance; it has been known in the form of smoke since ancient times (*Anderson*, 2009). In the 1700s, densely populated large cities were created due to the industrial revolution, making air pollution an increasing problem compared to the past (*Stevens et al*., 2020; *Ghirga*, 2021). However, the emissions are not yet considered significant compared to the current ones. The development of industry, and transport is much more defining and influencing air quality today (*Briggs et al*., 2000; *Krämer et al*., 2000; *Tang* and *Wang*, 2007). These are collectively referred to as anthropogenic sources.

The amount and type of artificial air pollutants emitted into the atmosphere may vary from country to country, depending, among other things, on the amount produced by industrial activity; modernity of the equipment used; type of fuel; degree of removal of contaminants; population; climate; and, last but not least, age, number, and technical adequacy of motor vehicles (*Aunan* and *Wang*, 2014; *Xu et al*., 2018; *Wang et al*., 2020). However, the leading causes of air pollution in urban areas are hazardous pollutants of anthropogenic origin, such as carbon monoxide, sulfur dioxide, nitrogen oxides, ozone, and particulate matter (*Chenet al.,* 2007; *Orellano et al.,* 2020). Our research focused on airborne dust pollution (PM_{10}, $PM_{2.5}$). They are often catalogued as 'floating dust' but are best known as particulate matter (PM), linked with most pulmonary and cardiac-associated morbidity and mortality (*Al-Hemoud et al*., 2018; *Pope et al.,* 1991; *Lu et al.,* 2015). In addition, long-term exposure to current ambient PM concentrations may lead to a marked reduction in life expectancy (*van Zelm et al.,* 2008; *Khaniabadi et al.,* 2016).

The air quality of the settlement is the result of interactions of natural and anthropogenic factors. With the continuous strengthening of environmental awareness, the population became increasingly interested in their living environment, especially the quality of the ambient air. Automatic monitoring stations are now installed almost everywhere globally to monitor the amount of pollutants in the atmosphere and inform the inhabitants of the settlement about the air quality. As the study area is a dynamically developing settlement, it may be necessary to locate a measuring station. Although the population data do not justify this, it can be a reasonable basis for settlement development and planning

decisions. In addition, it can help to prepare smog alarm plans and monitor the relationship between the air quality of the settlement and the health of the population.

2. Methodology

2.1. Study area

Balatonalmádi is located on the northern shore of Lake Balaton, about 8 km long, in the southern part of Veszprém county. It has an area of 49.88 km^2, 9,823 people (2019) and a population density of 197 people/km^2 ("Balatonalmádi population, population, area", 2022). The inner area is 759.89 ha, which can be said to be large, and the size of the holiday zone is over 294 ha (KD-ITS Konzorcium, 2015). The city is bordered on the east by Lake Balaton and the north by the Transdanubia Mountains. The topographic conditions played a decisive role in forming the settlement structure, and in some respects, they indicate the boundaries of the city districts.

The settlement consists of four parts of the city, which have different functions due to their character. The largest of them is the city center (called Almádi district), where most town institutions are located. In addition to the administrative function, a significant part of trade and hospitality is there. In addition, there is a considerable amount of residential and recreational area in this area. Due to the railway line separating the coastal strip from the city district there is direct connection between the two areas. The Budatava district officially belongs to Balatonalmádi, but it can be considered an independent district due to its structure and use. It has a unique structure that results from performing different functions. In the area, you will find a single-family residential neighbourhood, four-storey residential buildings, commercial units, a high school, and a site related to urban management. Budatava has many accessible areas that can be used for various functions ("Balatonalmádi", 2022). Vörösberény district was formerly an independent settlement, retaining some of its independence even after its merger with Balatonalmádi in 1971 (*Kredics* and *Lichtneckert,* 1995). In this part of the settlement, there are mostly residential areas, the center of the district is the Veszprémi road and the Ady Endre street. Here you will find the indispensable institutions of city life, such as the post office, GP surgeries, kindergartens, commercial units, and the house of culture. In terms of the nature of Káptalanfüred district, it is the most recreational area; the permanent population is 4% of the city's total population. The proportion of green and wooded areas is higher here than in the rest of the town. In addition to the forested areas, the natural value of Lake Köcsi and the coastal reeds is high.

2.2. Meteorological characteristics, green areas

The climate corresponds to the Hungarian average, usually warm and moderately dry. The number of hours of sunshine per year exceeds 2000, 800–810 hours in summer and only 190 hours in winter. The average annual temperature also corresponds to the climate and the general characteristics of the country (10.2–10.5 ° C), which is around 16.5–16.8 °C in summer (KD-ITS Konzorcium, 2015). The annual rainfall is 580–600 mm, above the national average of 567 mm. The prevailing wind direction is northern, with an average wind speed of 3 m/s, also in line with the national average. Overall, the climate is favorable for frost-sensitive arable crops and vine and fruit production. Its climatic potential offers outstanding tourism opportunities.

In terms of the hydrography of the area, Lake Balaton is dominant, as are the Vörösberényi Séd (5.4 km) and the Remete stream (2.5 km). Lake Köcsi in Káptalanfüred is a temporary lake.

The proportion of the green areas of Balatonalmádi (60 604 m^2) is low compared to the neighboring settlements. Peripheral forests cover more than 300 ha and contribute to improving the environment. Most public parks are located on the shores of Lake Balaton and in the central part of the city. In contrast, Vörösberény and Káptalanfüred contain less green space, which is due to the formation of the structure of the city districts. In Balatonalmádi, the number of rows of trees is typically low, and the location of the existing inland green areas is island-like. The preservation of forest patches on the vineyards is a priority due to the development of the future vision of the settlement.

2.3. Primary pollution source - traffic characteristics

Balatonalmádi can be called a sleeping town; the number of people who commute from the settlement is typically high. However, because the city is a tourist center, it increases 1.5–2 times during the summer. According to the data of the Central Statistical Office, in 2016, a total of 46,746 guests spent at least one night in the town ("Hungarian Central Statistical Office", 2022). The main road (highway 71) connecting Balatonvilágos with Keszthely passes through the city, handling significant tourist traffic. Although there is no direct connection to the expressway network, the M7 motorway can be reached at Balatonvilágos, 25 km from Balatonalmádi. The street view of Vörösberény and Öreghegy adapted to the topography. In contrast, in the case of Budatava and Káptalanfüred, the street system is more regular and designed. Most of the municipal roads are built, their general condition can be said to be adequate.

There are three traffic light junctions and nine railway crossings in the city. The low number of pedestrian crossings is a problem, making it difficult to cross due to increased traffic. The figure below (*Fig. 1*) shows the traffic situation in

the town. Significant congestion usually occurs at two traffic light junctions, both are is located on the main road.

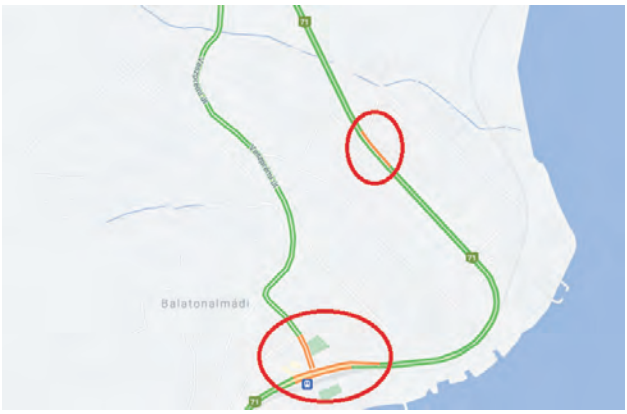

Fig. 1. The traffic situation in Balatonalmádi (source: Google Traffic Monitor)

The increased number of vehicles makes it increasingly difficult to park in the city (*Fig. 2*), especially during the summer months. However, car parks are on the beaches, in the city center, at the municipality and commercial facilities, all free of charge.

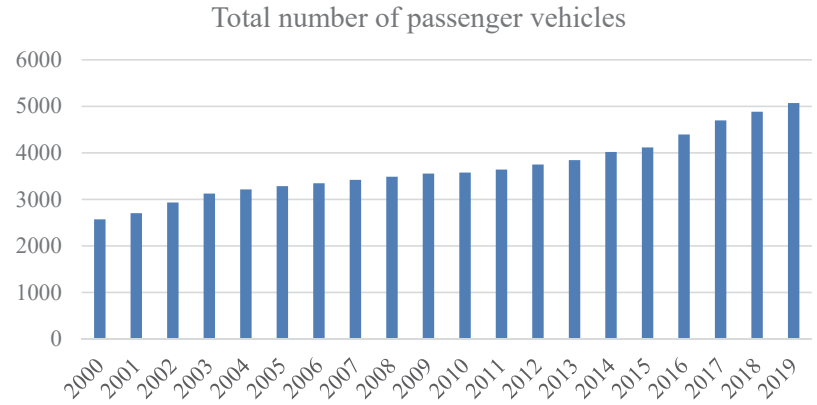

Fig. 2. Number of passenger vehicles in Balatonalmádi 2010-2019 (Source: in Hungarian Statistical Office)

2.4. The air quality of the settlement

The National Air Pollution Measurement Network operates a manual measuring station in the settlement (Bajcsy-Zsilinszky út 20.). Data on sulfur dioxide, settling dust and nitrogen dioxide have been available for this station since 2002. However, from 2006, only NO2 was measured at the measuring station ("OLM - Rólunk", 2022; "OLM - Manuális mérőhálózat", 2022). Based on the available data, the air quality of the settlement was good in each of the years. The problem with the manual measuring station is that it is not always possible to operate it continuously; longer or shorter periods of missing data can occur. As a result, the use of installed automatic measuring stations is more appropriate, especially in areas where significant, persistent air pollution can be expected. Alternatively, the daily fluctuations in pollution can be better monitored.

2.5. The instrument used for measurements

We measured the air pollution with a sensor called Laser $PM_{2.5}$ Sensor (*Fig. 3*). This laser sensor is suitable for measuring both $PM_{2.5}$ and PM_{10} fractions. The measuring range for both components is 0–999 $\mu g/m^3$. The principle of operation of the laser sensor is the following. The passage of particles through a detector results in the scattering of light converted into an electrical signal. This electrical signal is amplified by an amplifier and processed. The signal waveform depends on the number and size of the particles obtained during the analysis ("Laser $PM_{2.5}$ Sensor Specification", 2022). The technical parameters of the sensor used are shown in *Table 1*.

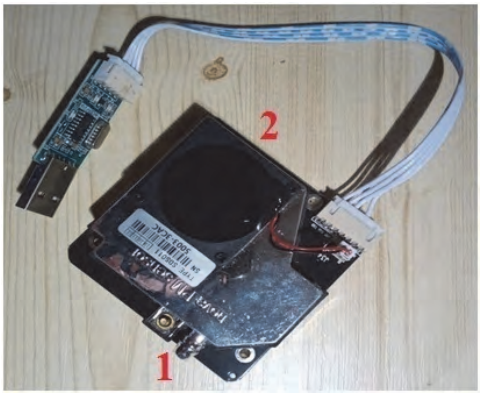

Fig. 3. The sensor used for measurements - The air is introduced at pipe marked with and the outlet at the fan is marked with 2.

Table 1. Technical data of the measuring instrument

Property	Sensor
Measured parameters	PM_{10}, $PM_{2,5}$
Measuring range	0,0-999,9 μg/m^3
Operating voltage	5 V
Operating current	70 mA ± 10 mA
Temperature range (during measurement)	-10 – 50 °C
Humidity (during measurement)	Max 70%
Pressure	86 kPa – 110 kPa
Setup time	1 s
Relative error	Max 15% 10 μg/m^3 esetén
Size	71×70×23 mm

3. Measurements and results

The measurements were performed on foot along dedicated routes in Balatonalmádi in two periods: in March 30 – April 11 and June 1–10 in 2021, almost every day between 7–8 in the morning and 16–17 in the afternoon. The primary purpose of choosing the date was to assess air pollution caused by peak traffic. We used a mobile phone application (Caynax GPS Sport Tracker) to record the routes, GPS coordinates, and time. When choosing the routes, we tried to give a good illustration of the air load caused by the busier areas, but at the same time, we would form a comprehensive picture of the air pollution of the largest possible area. The measurements were performed in Almádi, Budatava, and Vörösberény districts. As Káptalanfüred district is primarily a resort area, we did not examine that area during the measurements.

The measured values were recorded with a free downloadable program called DustSensorViewer v1.3. We set the sampling frequency to 1 minute with the program, which was the lowest value. From the measurement results, we calculated an average of the three routes for each day, which was plotted on the X-axis, showing the date of the measurement and the concentration in μg/m^3 on the Y-axis.

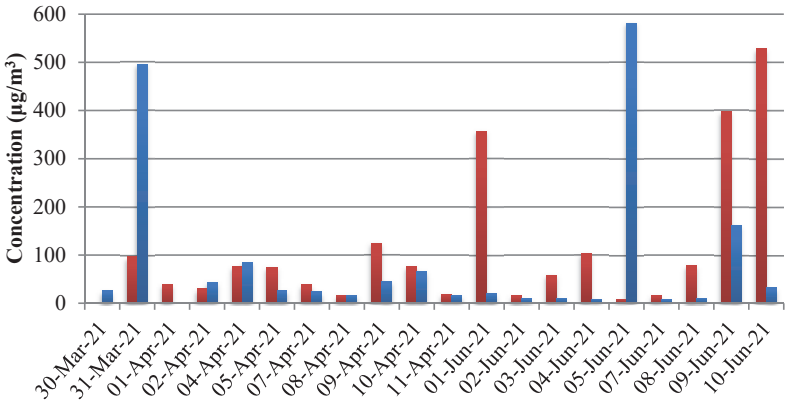

Fig. 4. Average PM_{10} concentrations in Balatonalmádi, Budatava, and Vörösberény districts (red: morning, blue: afternoon).

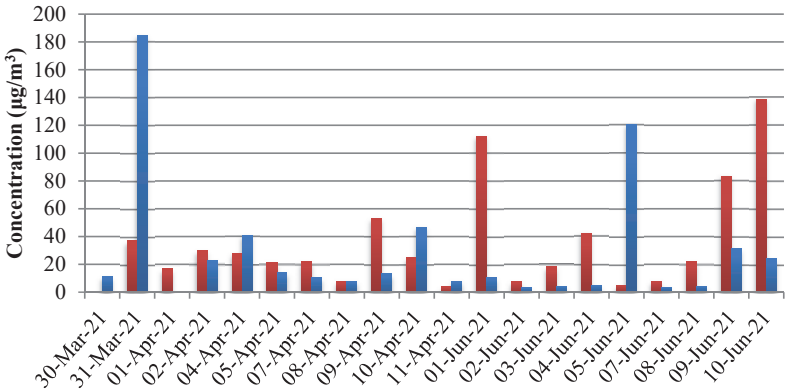

Fig. 5. Average $PM_{2.5}$ concentrations in Balatonalmádi, Budatava, and Vörösberény districts (red: morning, blue: afternoon).

Higher values for both fractions were detected in the morning (*Figs. 4* and *5*). The obtained results were lower than expected, according to which the concentration of airborne dust in the air is higher in the winter heating period. Compared to this, we observed persistently higher values during the measurements in June, which can be traced back to traffic and the release of pollen into the air. The higher values in June may also be explained by the April measurements taken during the closures due to the COVID-19 epidemic, when the schools were closed.

The results were plotted using an open-source GIS program called Quantum GIS 3.18.3. [38] First, we exported the GPS coordinates of the measurement routes from the application as a GPX file and then added this to the map as a new vector layer in the QGIS GIS program for map representation. We loaded the Open Street Map using the QuickMapServices module. Subsequently, the measured PM_{10} and $PM_{2.5}$ concentration values were assigned to the coordinates in $\mu g/m^3$, and the new layer was saved as an "shp" file. Then, the particulate dust concentrations were mapped using the inverse distance weighting (IDW) method. This is based on the fact that the weighting varies inversely with distance. On the resulting map, we set the display to "Palette / Custom Values" for the properties and the "Duplicate" function for the blending mode. Thus, the higher concentration values are displayed in red, while the lower ones are shown in blue, and the measurement paths and the base map are visible. We provided the finished maps with a scale, direction sign and legend.

In terms of all measurements, the concentration of particulate matter was remarkably high during the afternoon measurements, as shown in *Fig. 6*. Furthermore, the highest air load was on the Veszprém road section of the measurement route instead of the main road (highway 71) with generally higher road traffic. A similar distribution can be observed for $PM_{2.5}$.

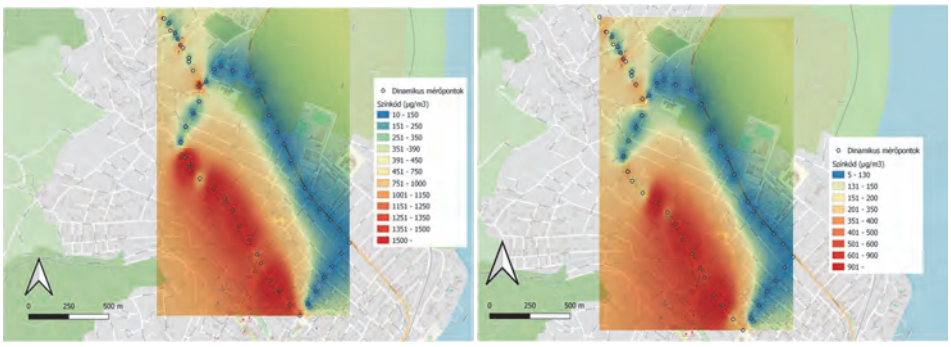

Fig. 6. PM_{10} (left) and $PM_{2.5}$ (right) measurement results of the most polluted day (afternoon of March 31, 2021).

During the morning measurement on April 4 (*Fig. 7*), the environment of Veszprém road was again more exposed to air pollution. The highest values were found on highway 71 Veszprém Road and measured at the intersection of Thököly út, connecting it with the main road. There is a lot of traffic at this intersection every day.

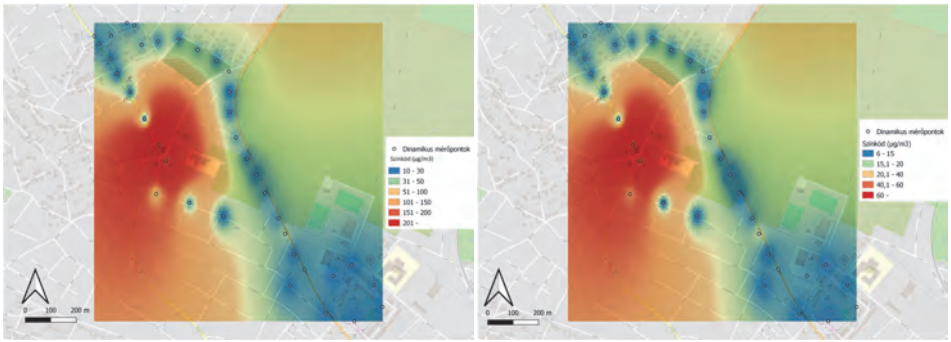

Fig. 7. PM_{10} (left) and $PM_{2.5}$ (right) concentrations in the morning of April 4, 2021.

In the afternoon measurement on April 5 (*Fig. 8*), unlike the previous ones, the highest immission was measured mainly not on the main routes, but ins típically single lane narrow streets whose small width contribute to higher concentraions. In the case of Balázs Béla street, where the air pollution was the highest, the topography also strongly influences the air quality. The middle section of the road lies in a kind of valley, and towards its two ends, it is usually bordered by a stone wall on at least one side. This significantly impedes the flow and mixing of air. As the paving of the surrounding streets being inadequate, their pollination is intense as well.

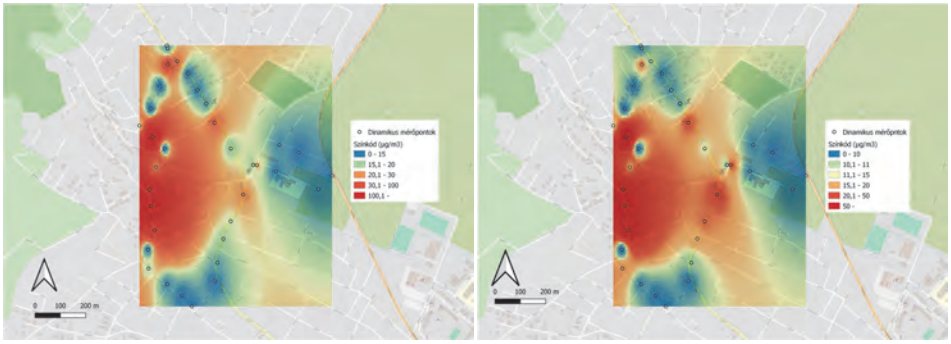

Fig. 8. PM_{10} (left) and $PM_{2.5}$ (right) concentrations in the afternoon of April 5, 2021.

In the case of the third route (*Fig. 9*), unlike the previous examples, the highest air pollution is shown in the vicinity of the main road. This was due to increased road traffic between 7 and 8 p.m.

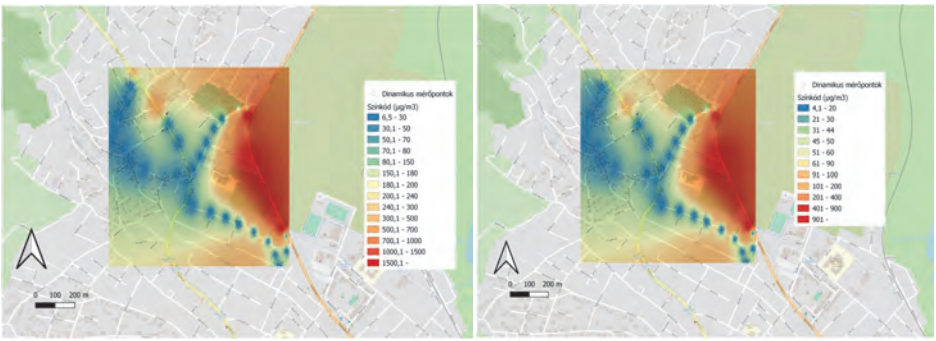

Fig. 9. PM_{10} (left) and $PM_{2.5}$ (right) concentrations in the morning of June 1, 2021.

For the fourth route, the concentration of $PM_{2.5}$ (*Fig. 10*) was also close to the remarkably high concentrations measured at the main road.

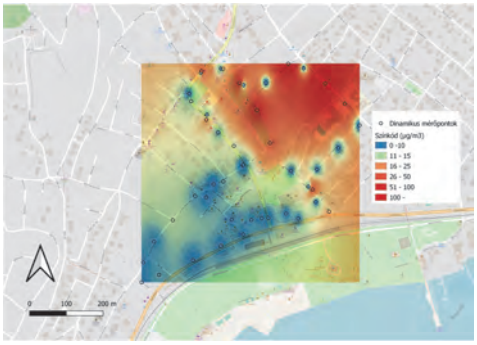

Fig. 10. $PM_{2.5}$ concentration in the morning of June 3, 2021.

4. Discussion – location of the immission measuring station

The immission measuring point must permanently be installed on a ventilated area, so there can be no disturbing landmarks in the environment that obstruct airflow. This condition significantly reduces the amount of suitable regions due to the characteristics of the settlement. In addition, a point must be selected that has no disturbing emission sources or traffic routes within a radius of 100 m. The settlement structure also limits this; the width of the streets does not allow it in several places.

Given the above factors, the best choice for locating an urban background pollution measuring station is a park with enough open space for unobstructed airflow. There are two parks in Balatonalmádi and on the coastal promenade. Of these areas, the waterside promenade is not suitable for the location of the measuring station, as there is significant tourist traffic there, and the visual impact of the measuring station must be taken into account. *Fig. 11* shows the location of the two parks. They are located close to each other at the bus station. For the first time out of the two areas, the Szent István Park may be a better choice in terms of size. The park along the Széchenyi promenade is rather long than wide, and the built-in area is strong here as well, so the airflow is obstructed. In Szent István Park, on the other hand, the air can flow freely around the measuring station, but there the existence of a distance of 100 m from the traffic road is questionable, as the busy bus station is right next to it.

Fig. 11. Investigation of the location of the immission measuring point in Balatonalmádi.

However, an area in the Vörösberény district may suit the measuring station (*Fig. 12*). There is a local primary school close to the main road (highway 71) and there is an open, grassy area between them where air can flow unimpeded. Sufficient distance from the traffic road can also be ensured. However, building a power supply in the area may require more resources than the previous two alternatives.

Fig. 12. The proposed area for placing the immission measuring point in Balatonalmádi.

The visible grassy area is currently unused; it is not significant from a tourist point of view, so the deterioration of the view is not a factor in the design of the measuring station. However, we would prioritize the landscaping in case of later utilization, thus creating a buffer zone between the school and the main road.

5. Conclusion

Environmental protection is playing an increasingly important role in our daily lives. In our research, we dealt with air quality protection, and within that with air pollution, its development and monitoring in urban environments. During our work, we mapped the air quality of the city of Balatonalmádi, focusing mainly on particulate matter. The purpose of immission measurement may be to determine the types and concentrations of air pollutants, map the spatial extent and the time course of the pollution, predict the dangerous situation, and search for sources and possible focal points. In addition, it can be used to obtain data during spatial and urban planning, establish official activities (impact assessment, permitting procedure), check the effectiveness of measures aimed at protecting air quality, provide data for scientific activities, and investigate public complaints. We paid special attention to the air pollution of the areas we considered problematic during the immission measurements. These are primarily located in the vicinity of the main transport routes. Furthermore, since several educational institutions are in the settlement, we tried to map their surroundings too. Because of the factors

mentioned above, a park with sufficient open space for the unobstructed airflow seemed to be the best choice for locating an urban background station.

We have previously stated that the concentration of airborne dust is highly dependent on traffic and road traffic. For this reason, the widespread use of more modern, more environmentally friendly vehicles is an important goal. To this end, it is necessary to move from petrol and diesel vehicles to more sustainable alternatives like car gas (LPG), hybrid and electric vehicles for both passenger and freight transport. In the case of passenger cars, the construction and promotion of P + R (Park and Ride) car parks can also be adequate. Promoting public transport is also an excellent way to reduce air pollution. For this, of course, the modernization of the vehicle fleet is essential. Providing discounted travel opportunities for the public can also help to promote public transport. In addition, supporting cycling by installation of a rental bike network can improve the air qiality. However, constructing new cycle paths in older built-up areas may be difficult due to the urban structure.

As we have experienced high immissions on several occasions near two educational institutions, it would be essential to intervene in these areas to protect children's health. The main road (highway 71) and the slightly busy but similar Veszprém road pass near the primary school in Vörösberény, which puts a heavy load on the students. There is also a playground next to the school, which is also exposed to a load of flying dust. Afforestation should be used in this area to sequester contaminants. It would be expedient to reduce car traffic in the vicinity of another school in the central part of the town, as afforestation cannot be solved there. There may be a successful competition system among students, the essence of which is that the classes from which most pupils come to school without using a car will be rewarded. In addition to the reform of the transport system, the creation of green spaces and the increase of their size is of paramount importance againtst air pollution. Tree planting in the settlement improves air quality and has a favorable effect on the microclimate, reducing the size of urban heat islands. That could make the town more livable.

References

Al-Hemoud, A., Al-Dousari, A., Al-Shatti, A., Al-Khayat, A., Behbehani, W., and *Malak, M.,* 2018: Health Impact Assessment Associated with Exposure to PM10 and Dust Storms in Kuwait. *Atmosphere 9*(1), 6. doi: 10.3390/atmos9010006

Anderson, H., 2009: Air pollution and mortality: A history. *Atmos. Environ. 43*, 142–152. https://doi.org/10.1016/j.atmosenv.2008.09.026

Aunan, K. and *Wang, S.,* 2014: Internal migration and urbanization in China: Impacts on population exposure to household air pollution (2000–2010). *Sci. Total Environ. 481*, 186–195. https://doi.org/10.1016/j.scitotenv.2014.02.073

Balatonalmádi population, population, area, 2022: Retrieved January 11, 2022, from http://nepesseg.com/veszprem/balatonalmadi

Briggs, D., de Hoogh, C., Gulliver, J., Wills, J., Elliott, P., Kingham, S., and *Smallbone, K.*, 2000: A regression-based method for mapping traffic-related air pollution: application and testing in four contrasting urban environments. *Sci. Total Environ. 253*, 151–167. https://doi.org/10.1016/s0048-9697(00)00429-0

Chen, T., Kuschner, W., Gokhale, J., and *Shofer, S.*, 2007: Outdoor Air Pollution: Nitrogen Dioxide, Sulfur Dioxide, and Carbon Monoxide Health Effects. *Amer. J. Medical Sci. 333*, 249–256. https://doi.org/10.1097/maj.0b013e31803b900f

Ghirga, G., 2021: Air pollution was high centuries before industrial revolutions and may have been responsible for cancer rates in medieval Britain. *Cancer 127*, 3698–3698. https://doi.org/10.1002/cncr.33681

Gurjar, B., Jain, A., Sharma, A., Agarwal, A., Gupta, P., Nagpure, A., and *Lelieveld, J.*, 2010: Human health risks in megacities due to air pollution. *Atmos. Environ. 44*, 4606–4613. https://doi.org/10.1016/j.atmosenv.2010.08.011

Hungarian Central Statistical Office. 2022: Retrieved January 11, 2022, from https://www.ksh.hu/?lang=en

Kampa, M. and *Castanas, E.*, 2008: Human health effects of air pollution. *Environmental Pollution*, *151*(2), 362-367. https://doi.org/10.1016/j.envpol.2007.06.012

KD-ITS Konzorcium, 2015: Balatonalmádi Város Integrált Településfejlesztési Stratégiája. http://archiv.balatonalmadi.hu/files/6914/4230/6431/kd_its_balatonalmadi_megalapozo_vizsgalat_0817.pdf

Khaniabadi, Y., Goudarzi, G., Daryanoosh, S., Borgini, A., Tittarelli, A., and *De Marco, A.*, 2016: Exposure to PM10, NO2, and O3 and impacts on human health. *Environ. Sci. Pollut. Res. 24*, 2781–2789. https://doi.org/10.1007/s11356-016-8038-6

Kim, K., Jahan, S., and *Kabir, E.*, 2013: A review on human health perspective of air pollution with respect to allergies and asthma. *Environ. Int. 59*, 41–52. https://doi.org/10.1016/j.envint.2013.05.007

Kinney, P., 2008: Climate Change, Air Quality, and Human Health. *Amer. J. Prev. Medicine 35*, 459–467. https://doi.org/10.1016/j.amepre.2008.08.025

Krämer, U., Koch, T., Ranft, U., Ring, J., and *Behrendt, H.*, 2000: Traffic-Related Air Pollution Is Associated with Atopy in Children Living in Urban Areas. *Epidemiology 11*, 64–70. https://doi.org/10.1097/00001648-200001000-00014

Kredics, L. and *Lichtneckert A.*, 1995: Balatonalmádi és Vörösberény története. Almádiért Alapítvány, Balatonalmádi. (In Hungarian)

Lu, F., Xu, D., Cheng, Y., Dong, S., Guo, C., Jiang, X., and *Zheng, X.*, 2015: Systematic review and meta-analysis of the adverse health effects of ambient PM2.5 and PM10 pollution in the Chinese population. *Environ. Res. 136*, 196–204. https://doi.org/10.1016/j.envres.2014.06.029

OLM – Manuális mérőhálózat, 2022: Retrieved January 11, 2022, from http://www.levegominoseg.hu/manualis-merohalozat

OLM – Rólunk, 2022: Retrieved January 11, 2022, from http://www.levegominoseg.hu

Orellano, P., Reynoso, J., Quaranta, N., Bardach, A., and *Ciapponi, A.*, 2020: Short-term exposure to particulate matter (PM10 and PM2.5), nitrogen dioxide (NO2), and ozone (O3) and all-cause and cause-specific mortality: Systematic review and meta-analysis. *Environ. Int. 142*, 105876. https://doi.org/10.1016/j.envint.2020.105876

Pope, C., Dockery, D., Spengler, J., and *Raizenne, M.*, 1991: Respiratory Health and PM10Pollution: A Daily Time Series Analysis. *American Review Of Respirat. Disease 144*(3_pt_1), 668–674. https://https://doi.org/.org/10.1164/ajrccm/144.3_pt_1.668

Stevens, C., Bell, J., Brimblecombe, P., Clark, C., Dise, N., and *Fowler, D. et al.*, 2020: The impact of air pollution on terrestrial managed and natural vegetation. *Philosoph. Trans. Roy. Soc. A: Math. 378*(2183), 20190317. https://doi.org/10.1098/rsta.2019.0317

Tang, U. and *Wang, Z.*, 2007: Influences of urban forms on traffic-induced noise and air pollution: Results from a modelling system. *Environ. Model. Software 22*, 1750–1764. https://doi.org/10.1016/j.envsoft.2007.02.003

van Zelm, R., Huijbregts, M., den Hollander, H., van Jaarsveld, H., Sauter, F., and *Struijs, J. et al.,* 2008: European characterization factors for human health damage of PM10 and ozone in life cycle impact assessment. *Atmos. Environ. 42*, 441–453.
https://doi.org/10.1016/j.atmosenv.2007.09.072

Wang, S., Gao, S., Li, S., and *Feng, K.,* 2020: Strategizing the relation between urbanization and air pollution: Empirical evidence from global countries. *J. Clean. Product. 243*, 118615. https://doi.org/10.1016/j.jclepro.2019.118615

Xu, X., González, J., Shen, S., Miao, S., and *Dou, J.*, 2018: Impacts of urbanization and air pollution on building energy demands — Beijing case study. *Appl. Energy 225*, 98–109. https://doi.org/10.1016/j.apenergy.2018.04.120

DOI:10.28974/idojaras.2020.1.7

IDŐJÁRÁS

Quarterly Journal of the Hungarian Meteorological Service
Vol. 127, No. 1, January – March, 2023, pp. 123–142

Comparison of four precipitation based meteorological drought indices in the Yesilirmak Basin, Turkey

Utku Zeybekoglu[1,*], **Alyar Boustani Hezarani**[2], and **Aslı Ulke Keskin**[2]

[1]*Sinop University,*
Department of Construciton,
Boyabat, Sinop, Turkey

[2]*Ondokuz Mayis University,*
Department of Civil Engineering,
Atakum, Samsun, Turkey

**Corresponding author E-mail: utkuz@sinop.edu.tr*

(Manuscript received in final form January 24, 2022)

Abstract— Drought, which is often defined as not enough precipitation, does not a mean simple lack of precipitation. This condition, which occurs when humidity is less than the average value for many years, is caused by a disrupted balance between precipitation and evaporation in a region. It is very difficult to predict the start and the end time of drought. In the present study, the drought conditions of the stations selected from Yesilirmak Basin between 1970 and 2014 were determined by using Z-Score Index (ZSI), China-Z Index (CZI), Modified China-Z Index (MCZI), and Standard Precipitation Index (SPI), and the compliance of these indices to the SPI was investigated. It was determined that these indices gave parallel results to each other, and SPI detected drought earlier than other indices.

Key-words: drought indices, drought monitoring; standard precipitation index, Z-score index, modified China-Z index

1. Introduction

Drought, which is the most dangerous among natural disasters, has not yet been defined in full in the world literature. The effects of drought are felt increasingly all over the world. In general, human beings become aware of drought when there is water shortage (*Hejazizadeh* and *Javizadeh,* 2011). It is very difficult to predict

the start and end time of droughts because it is a disaster occurring insidiously showing effects gradually, and continuing for a long time. Although earthly and regional climate characteristics play very important roles in the emergence of drought, the change of climate is not the only reason. The reasons for the emergence of droughts are not always the same factor in every basin. Also, the same lack of precipitation causes different perceptions at different times of the year in different areas. The causes of droughts are not yet clearly defined. Drought, which is often defined as not enough precipitation, is not a mere lack of precipitation. Drought occurs if humidity is less than the average value for many years due to a disrupted balance between precipitation and evaporation in an area (*Downer et al.,* 1967).

It has been observed in recent years that researchers have used various drought indices with greater emphasis on drought studies with global warming (*Lloyd-Hughes* and *Saunders,* 2002; *Sirdas* and *Sen,* 2003; *Yildiz*, 2009; *Oguzturk* and *Yildiz,* 2014, 2015, 2016; *Deo* and *Sahin,* 2015; *Yue et al.,* 2015; *Osuch et al.,* 2016; *Ionita et al.,* 2016; *Wang et al.,* 2017; *Gumus* and *Algin,* 2017; *Yacoub* and *Tayfur,* 2017; *Ramkar* and *Yadav,* 2018; *Myronidis et al.,* 2018; *Bushra et al.,* 2019; *Garcia-Leon et al.,* 2019; *Payab* and *Turker,* 2019; *Pathak* and *Dodamani,* 2019; *Yenigun* and *Ibrahim*, 2019; *Kumanlioglu,* 2020; *Vergni et al.,* 2021). *Wu et al.* (2001) compared results of three drought indices (standard precipitation index (SPI), China-Z index (CZI), and Z-score index (ZSI)) for China. *Morid et al.* (2006) compared seven different drought indices (SPI, percent of normal (PN), deciles iIndex (DI), ZSI, CZI, modified China-Z index (MCZI), and effective drought index (EDI)). As a result of the study, it was concluded that DI reacted rapidly to precipitation events in certain years, but exhibited temporal and field inconsistencies, while SPI and EDI were good at detecting the start of drought showing temporal and field consistency, but EDI produced more sensitive results than SPI. *Dogan et al.* (2012) compared six different drought indices in the Konya Closed Basin. They used the drought indices of PN, rainfall decile-based drought index (RDDI), ZSI, CZI, SPI and EDI. *Soleimani et al.* (2013) conducted a study to determine drought in Talegani city, which is a semi-arid area in Iran and analyzed SPI, RDDI, and CZI relatively to each other. They found that SPI yielded the best results. *Jain et al.* (2015) observed drought events in the Ken River Basin with SPI, EDI, ZSI, CZI, Rainfall Departure and DI. *Zarei et al.* (2017) compared performance of CZI, ZSI, SPI, and EDI for drought assessment in Chaharmahal-Bakhtiari province, Iran. *Nedham* and *Hassan* (2019) compared SPI, ZSI, and PPA in Iraq. The authors revealed, that all drought indices had a strong positive relationship between each other. *Katipoglu et al.* (2020) investigated droughts of the Euphrates Basin with SPI, ZSI, RAI, SPEI, and RDI. *Sridhara et al.* (2021) applied and compared five precipitation-based indices (DI, PN, CZI, ZSI, and SPI). Authors stated that SPI, CZI, and ZSI performances were similar in identifying drought. *Dikici* and *Aksel* (2021) monitored meteorological and hydrological drought by 13 drought indices for Ceyhan Basin, Turkey.

The purposes of this study were (i) to identify drought events and (ii) to evaluate the performance of four meteorological drought indices (ZSI, CZI, MCZI, SPI) in the Yesilirmak Basin. The monthly precipitation records of four meteorological observation stations (Amasya, Corum, Samsun, and Tokat) located in Yesilirmak Basin were used. When longer records are used to calculate drought indices, more reliable results can be obtained (*Wu et al.,* 2001). For this reason, applications were made for a 45-year-long period between 1970 and 2014, which was the longest data range available at the meteorology stations in the basin.

2. Study area

The Yesilirmak Basin covers the area in the northern part of Anatolia, which discharges its waters into the Black Sea with Yesilirmak. The Basin Area is surrounded by the Canik, Giresun, Gumushane, Pulur, Cimen, Kizildag, Kose, Tekeli, Yildiz, Çamlıbel, Akdaglar, Karababa, İnegöl, and Kunduz mountain peaks with water separation line, and the Black Sea; and constitutes approximately 38732.8 km^2. The precipitation area of the Yesilirmak Basin is 36129 km^2, with an annual precipitation of 646 mm (*TUBITAK,* 2010). The localization of Amasya, Corum, Samsun, and Tokat meteorological stations used in the study in the basin are given in *Fig 1* and positional characteristics are given in *Table 1*.

Table 1. Positional characteristics of selected meteorological stations

Station Name	Station Code	Elevation (m)	Latitude (N)	Longitude (E)
Amasya	17085	409	40.6668	35.8353
Corum	17084	776	40.5461	34.9362
Samsun	17030	4	41.3435	36.2553
Tokat	17086	611	40.3312	36.5577

Fig. 1. Distribution of meteorological stations in the Yesilirmak Basin (*TUBITAK*, 2010)

3. Drought indices

3.1. Standard precipitation index

McKee et al. (1993) developed SPI to identify and monitor regional droughts. In fact, SPI ensures the standardized conversion of the observed precipitation probability; and can be calculated for desired time periods (1, 3, 6, 9, 12, 24, and 48 months). Short-term time periods (weekly and monthly) are important for agricultural water requirements and water potentials, and long-term time periods such as years (12, 24, 36 months) are important for water supply, water resources management, and groundwater studies (*Mishra* and *Singh,* 2011). SPI can be used according to normal, log-normal, and gamma distributions of precipitation (*Yacoub* and *Tayfur,* 2017). However, it was reported that climatic precipitation series match gamma distribution better (*Thom*, 1958; *Mishra* and *Singh,* 2010; *Yacoub* and *Tayfur,* 2017). The probability density function of the gamma distribution, *g(x)* is given as

$$g(x) = \frac{1}{\beta^{\alpha}\Gamma(\alpha)} x^{\alpha-1} e^{\frac{-x}{\beta}}; x, \alpha, \beta > 0 \,, \tag{1}$$

and the gamma function is given as

$$\Gamma(\alpha) = \int_0^{\infty} x^{\alpha-1} e^{-y} dx \,, \tag{2}$$

where *x* refers to the amount of precipitation, $\Gamma(\alpha)$ is the gamma function, α and β *are the shape and scale parameters, respectively*. SPI requires that a Gamma probability density function is adapted to frequency distribution given with precipitation totals for a station. The shape (α) and scale (β) parameters of the gamma probability density function are predicted for each station and time period in question. The maximum probability solutions given by *Thom* (1958) are used in predicting the α and β (*Bacanli et al.,* 2009; *Bacanli* and *Kargi,* 2019). α and β are obtained as

$$\alpha = \frac{1}{4A}\left(1 + \sqrt{1 + \frac{4A}{3}}\right); \beta = \frac{\overline{x}}{\alpha}; A = ln(\overline{x}) - \sum \frac{ln(x)}{n} \,, \tag{3}$$

where *n* refers to the number of observations. The resulting parameters are used in forming the probability function *G(x)* given by the following formula (*Bacanli,* 2017)

$$G(x) = \int_0^x g(x)dx = \frac{1}{\beta^{\alpha}\Gamma(\alpha)} \int_0^x x^{\alpha-1} e^{\frac{-x}{\beta}} dx \tag{4}$$

When $t=x/\beta$, the gamma function is by the following formula (*Yacoub* and *Tayfur*, 2020)

$$G(x) = \frac{1}{\Gamma(\alpha)} \int_0^x t^{\alpha-1} e^{-t}\, dt\ . \tag{5}$$

The gamma distribution is non-defined for zero values of x; however, since the precipitation series may contain zero values, the cumulative probability distribution $H(x)$ for zero precipitation and precipitations other than zero is identified as (*Lloyd-Hughes* and *Saunders*, 2002):

$$H(x) = q + (1-q)G(x) \tag{6}$$

where q is the probability of zero. If m is the number of zeros in the precipitation time series, it can be predicted as $q=m/n$. The probability function $H(x)$ is converted into SPI that has an average of zero and a variance of 1 with a standard normal random value. The SPI value according to the $H(x)$ value obtained in this way is calculated by the following formulas (*Abramowitz* and *Stegun*, 1965):

$$0 < H(x) < 0.5, SPI = -\left(t - \frac{c_0+c_1t+c_2t^2}{1+d_1t+d_2t^2+d_3t^3}\right), t = \sqrt{ln\left(\frac{1}{(H(x))^2}\right)}, \tag{7}$$

and

$$0.5 < H(x) < 1.0, SPI = +\left(t - \frac{c_0+c_1t+c_2t^2}{1+d_1t+d_2t^2+d_3t^3}\right), t = \sqrt{ln\left(\frac{1}{(1.0-H(x))^2}\right)}, \tag{8}$$

where $c_0 = 2.515517$, $c_1 = 0.802853$, $c_2 = 0.010328$, $d_1 = 1.432788$, $d_2 = 0.189269$ and $d_3 = 0.001308$ are constant throughout the equation (*McKee et al.*, 1995).

Dry and humid periods are represented in the same way in the selected time period as a result of the normalization of SPI values. The month in which the index value falls below -1 is defined as the start of the drought, and the time period in which the index continues below -1 is defined as the dry period in drought evaluations (*McKee et al.*, 1995; *Mishra* and *Singh*, 2011). According to the index results, drought categories are given in *Table 2*.

3.2. Z-score index

Raw precipitation data are used in the ZSI method, which is a unidimensional drought index. As seen in Eq.(9), it is obtained by dividing the difference of the

average into the standard deviation without converting the precipitation to normal distribution within the specified time period (*Wu et al.,* 2001). ZSI has standard deviation and standard average, in other words, the standard average is 0, and the standard deviations of ZSI values are equal to 1, the values above the average are positive, and those below are negative.

$$ZSI = \frac{x_i - \bar{x}}{\sigma}, \tag{9}$$

where x_i refers to the precipitation values in the time period, $\bar{x}$ refers to the average precipitation data, and σ refers to the standard deviation. The drought classification according to ZSI is given in *Table 2*.

3.3. China-Z index

It is a drought index assuming that the CZI precipitation data fits to the Pearson-type III distribution. It has been used by the China National Climate Center since 1995 to monitor drought conditions throughout the country; and is calculated as (*Morid et al.,* 2006; *Dogan et al.,* 2012; *Jain et al.,* 2015; *Payab* and *Turker,* 2019):

$$CZI = \frac{6}{C_s}\left(\frac{C_s}{2} ZSI + 1\right)^{1/3} - \frac{6}{C_s} + \frac{C_s}{6};\ C_s = \frac{\sum_{j=1}^{n}\left(x_j - \bar{x}\right)^3}{n * \sigma^3}, \tag{10}$$

where x_j refers to the amount of precipitation converted into normal distribution in the time period, n refers to the total number of time periods, ZSI refers to the results of the Z-score index, and C_s refers to the skewness coefficient of precipitation data. The drought classification according to CZI value is given in *Table 2*.

3.4. Modified China-Z index

The calculation of MCZI is similar to the calculation of CZI, only the median value (*Me*) is used instead of the average in Eq.(10) (*Wu et al.,* 2001; *Morid et al.,* 2006). The acquisition of the index is given as (*Morid et al.,* 2006):

$$MCZI = \frac{6}{C_s}\left(\frac{C_s}{2}\varphi_j + 1\right)^{1/3} - \frac{6}{C_s} + \frac{C_s}{6};\ C_s = \frac{\sum_{j=1}^{n}\left(x_j - Me\right)^3}{n * \sigma^3};\ \varphi_j = \frac{x_j - Me}{\sigma}, \tag{11}$$

where φ_j is the standard variable, and *Me* refers to the median value of precipitation. The drought classification according to MCZI value is given in *Table 2*.

Table 2. Classification of drought conditions according to the SPI, ZSI and CZI/MCZI (*Morid et al.,* 2006; *McKee et al.,* 1995; *Kutiel et al.,* 1996; *Jain et al.,* 2015)

Category	SPI	ZSI	CZI/MCZI
Normal	−0.99 to 0.99	−0.99 to 0.99	−0.99 to 0.99
Moderately dry	−1.0 to −1.49	−1.0 to −1.49	−1.0 to −1.49
Severe dry	−1.5 to −1.99	−1.5 to −1.99	−1.5 to −1.99
Extreme dry	≤−2	≤−2	≤−2

4. Results and discussion

In the scope of the study, SPI, ZSI, CZI, and MCZI were applied in three different time scales (3 months,12 months, 24 months) for 4 meteorological stations selected in the Yesilirmak Basin, and the progression of the indices on the time axis are given in *Figs. 2–5*. In the evaluations, SPI was identified as the reference index since it showed the beginning of droughts earlier, moreover, it was reliable, required only precipitation data, and yielded better results (*Morid et al.,* 2006; *Dogan et al.*, 2012; *Mishra* and *Singh,* 2011; *Yacoub* and *Tayfur,* 2017).

Figs. 2–5 in which the temporal change of the 4 drought indices were given were evaluated, and *Tables 3–6* were prepared. The most severe and the longest durations of the droughts determined by the indices for each station are determined in these Tables, and the start and end dates of the droughts in question are given.

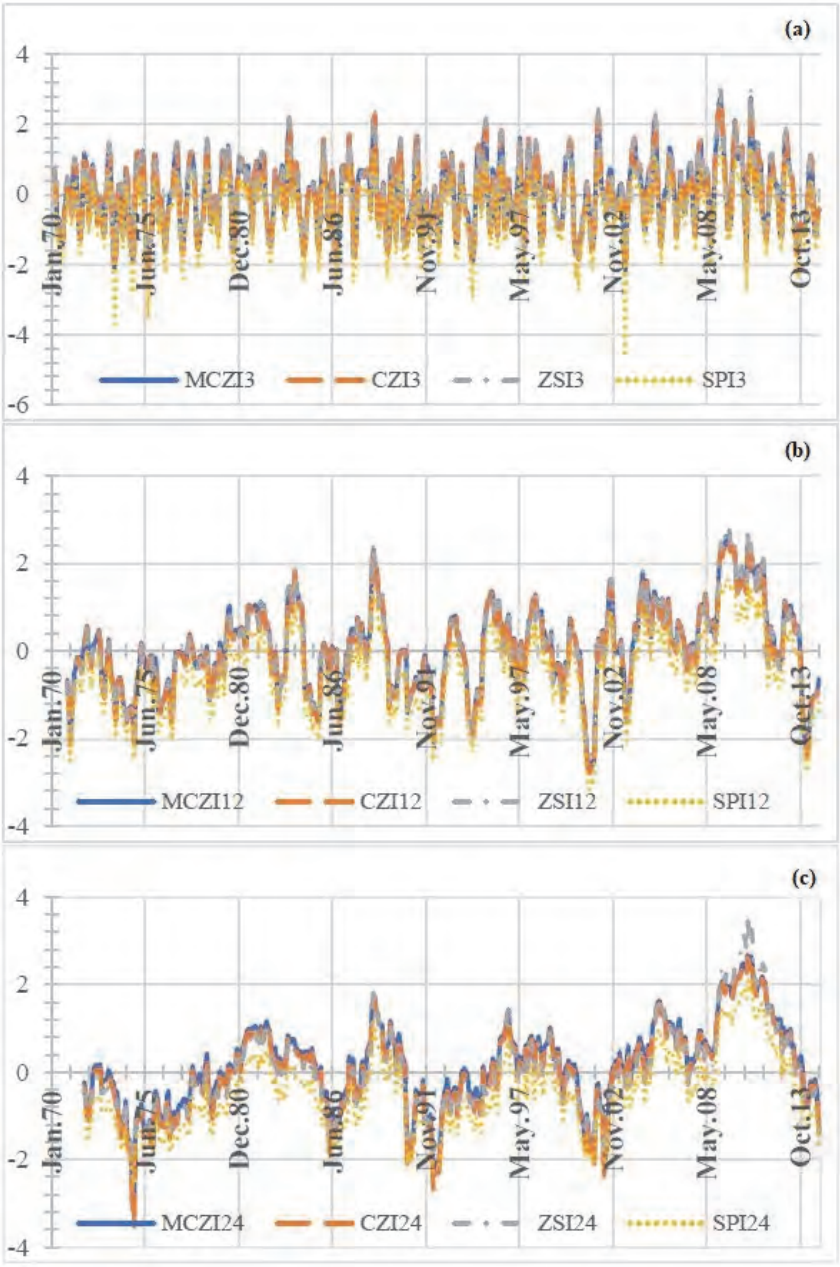

Fig. 2. Drought indices values of Amasya stationfor 3-, 12-, and 24-month periods.

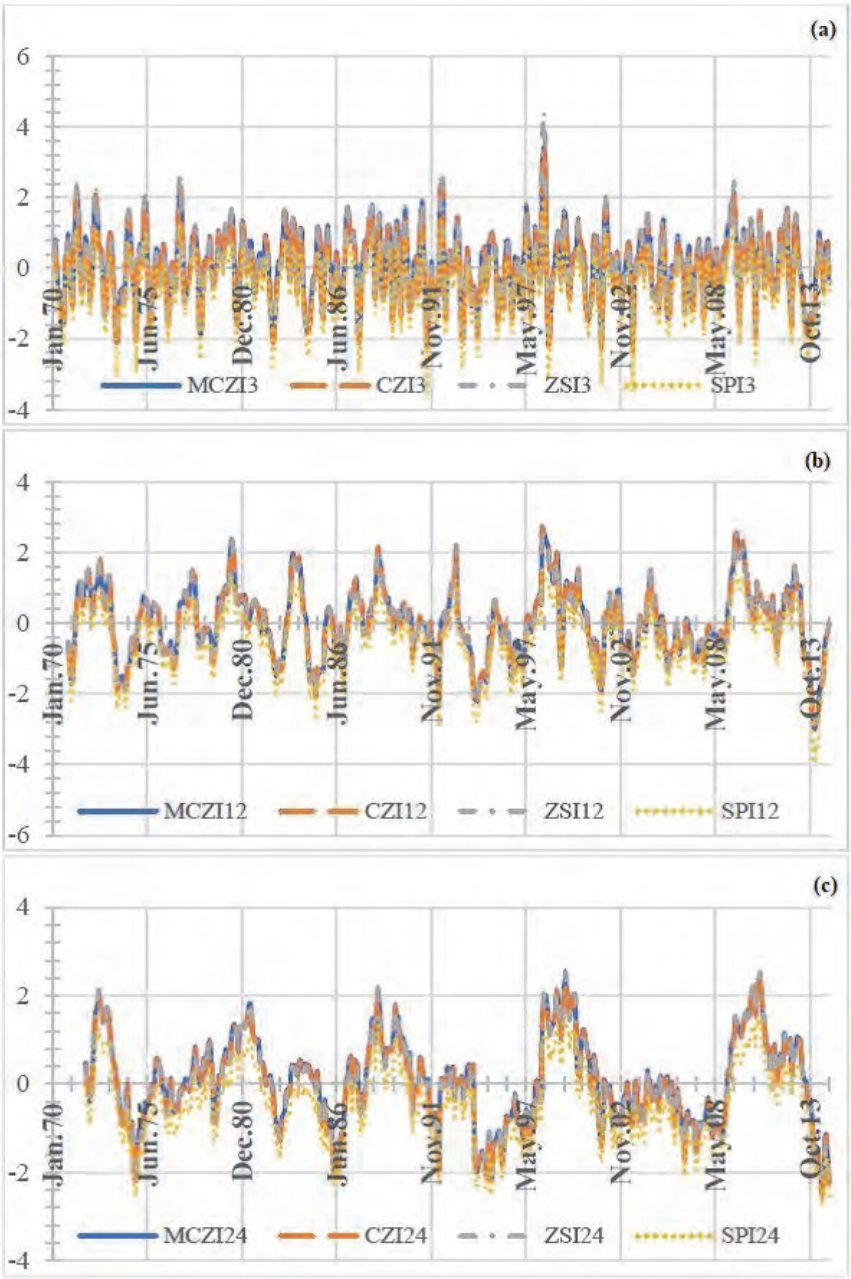

Fig. 3. Drought indices values of Corum station for 3-, 12-, and 24-month periods.

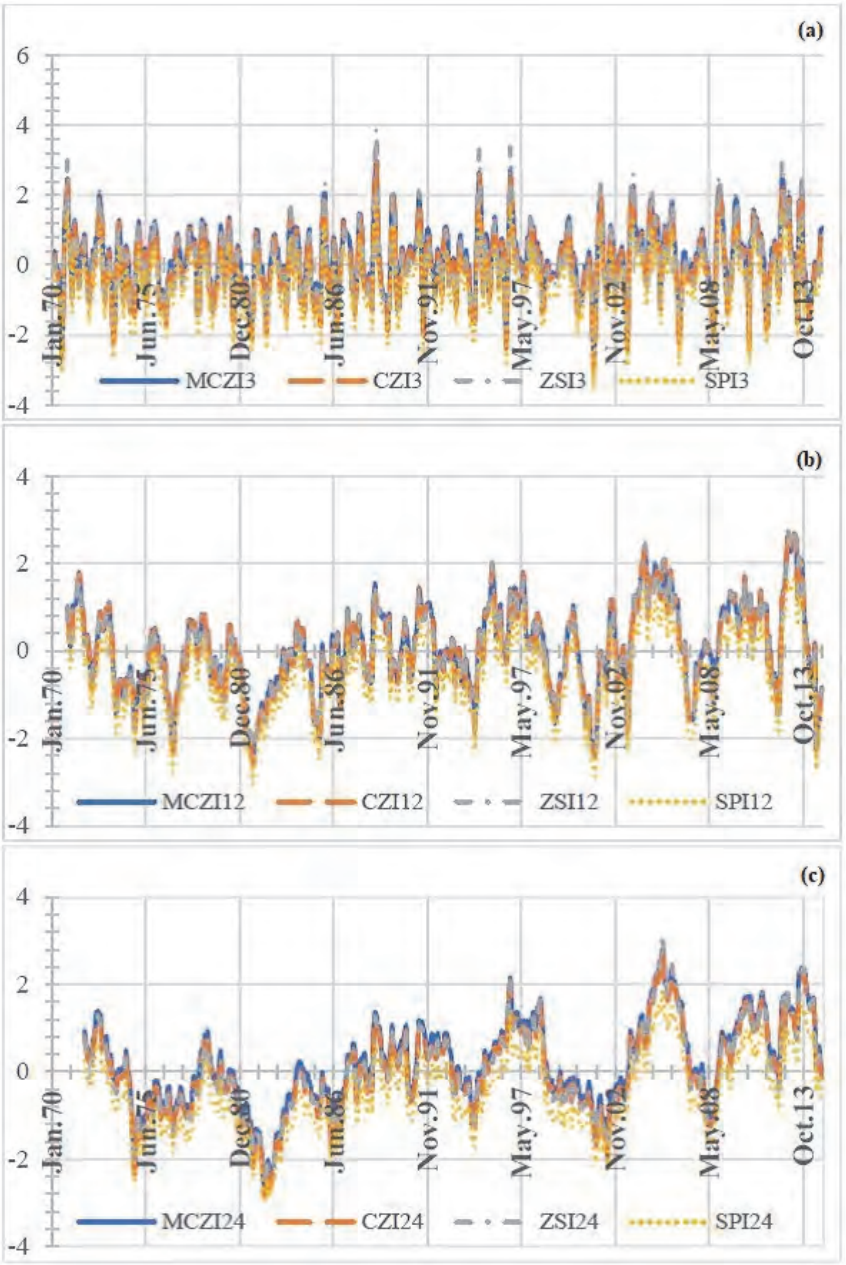

Fig. 4. Drought indices values of Samsun station for 3-, 12-, and 24-months periods.

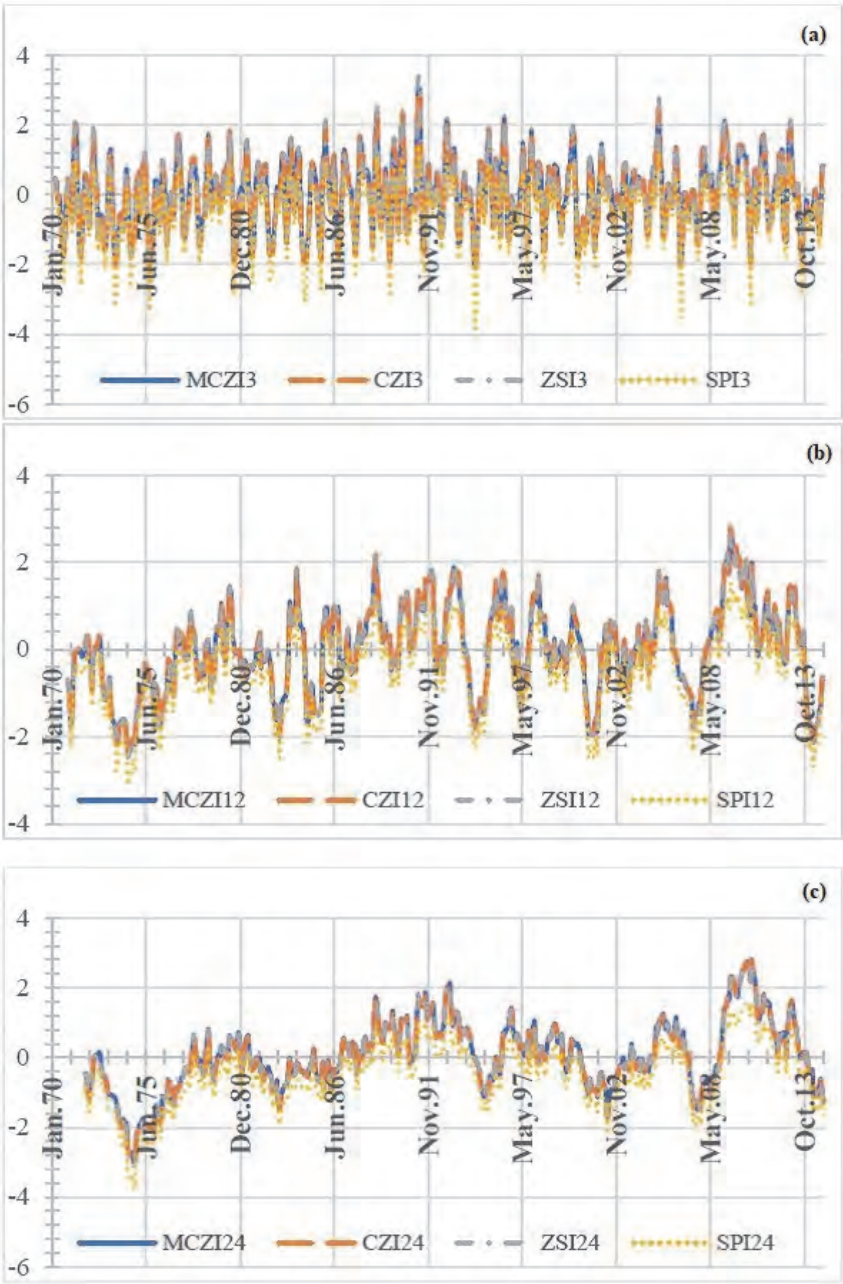

Fig. 5. Drought indices values of Tokat for 3-, 12-, and 24-month periods.

Table 3. The longest dry periods and the date of the most extreme dry period for Amasya station

Indices	The longest dry period	Duration (Month)	Value of the most extreme drought	Date
SPI-3	Jun 2013 - Feb2014	8	-4.54	Aug 2003
ZSI-3	Aug 2000-Jan 2001	6	-2.00	
CZI-3			-2.18	
MCZI-3			-2.18	
SPI-12	Jul 1973-Feb 1975	20	-3.17	Jun2001
ZSI-12	Dec 2013-Okt 2014	11	-2.45	
CZI-12			-2.79	
MCZI-12	Feb 2001-Nov 2001	10	-2.74	
SPI-24	Sep 1973-Feb 1978	54	-2.62	Nov 1974
ZSI-24	Nov 1991-Nov 1992	13	-2.06	
CZI-24			-3.54	
MCZI-24	May 1975-Dec 1975	8	-3.10	

Table 4. The longest dry periods and the date of the most extreme dry period for Corum station

Indices	The longest dry period	Duration (Month)	Value of the most extreme drought	Date
SPI-3	Jun 2013-Feb 2014	9	-3.54	Sep 1991
ZSI-3	Jul 2013-Feb 2014	8	-1.92	
CZI-3			-2.37	
MCZI-3			-2.27	
SPI-12	Jul 2013-Sep 2014	15	-3.97	Feb 2014
ZSI-12	Sep 1973-Jul 1974 Nov 1984-Sep 1985 May 1994-Mar 1995	11	-3.04	
CZI-12			-3.00	
MCZI-12	Oct 2013-Aug 2014		-3.01	
SPI-24	Jun 1994-Jun 1996	28	-2.75	Jul 2014
ZSI-24	Jun 1994-Mar 1996	22	-2.28	
CZI-24			-2.52	
MCZI-24			-2.47	

Table 5. The longest dry periods and the date of the most extreme dry period for Samsun station

Indices	The longest dry period	Duration (Month)	Value of the most extreme drought	Date
SPI-3	Apr 1976-Oct 1976 Mar 1985-Sep 1985	7	-3.58	Aug 2001
ZSI-3	Aug 1974-Nov 1974 Jul 1981-Oct 1981 Jun 1994-Sep 1994 Jan 2014-Apr 2014		-2.08	
CZI-3	Aug 1974-Nov 1974 Jul 1981-Oct 1981 Jun 1989-Sep 1989 Jun 1994-Sep 1994 Jul 2001-Oct 2001 Jan 2014-Apr 2014	4	-3.05	
MCZI-3	Aug 1974-Nov 1974 Jul 1981-Oct 1981 Jun 1994-Sep1994		-2.76	
SPI-12	Mar 1981-May 1983	27	-3.07	Oct 1981
ZSI-12			-2.44	
CZI-12	Apr 1981-Jul 1982	16	-2.59	
MCZI-12			-2.56	
SPI-24	Dec 1980-Mar 1984	40	-2.99	Jun 1982
ZSI-24	Jul 1981-Sep 1983	27	-2.45	
CZI-24			-2.87	
MCZI-24	Jul 1981-Jun 1983	24	-2.65	

Table 6: The longest dry periods and the date of the most extreme dry period for Tokat station

Indices	The longest dry period	Duration (Month)	Value of the most extreme drought	Date
SPI-3	Jul 1974-Nov 1974 Aug 1975-Dec 1975 Aug 1982-Dec 1982 Aug 1984-Dec 1984	5	-3.97	Sep 1994
ZSI-3			-1.96	
CZI-3	Aug 1984-Dec 1984		-2.13	
MCZI-3			-2.11	
SPI-12	Jun 1973-May 1975	24	-3.13	Jun 1974
ZSI-12			-2.49	
CZI-12	Jun 1973-Mar 1975	22	-2.40	
MCZI-12			-2.44	
SPI-24	Feb 1973-Aug 1977	55	-3.76	Oct 1974
ZSI-24			-3.11	
CZI-24	Apr 1973-Sep 1976	42	-3.04	
MCZI-24			-3.01	

As seen in *Figs. 2–5* and *Tables 3–6*, according to the results of 3-month indices for Amasya, the driest month was August 2003, while June 2001was the driest month for the 12-month indices, and November 1974 for the 24-month indices (*Table 3*). For Corum, September 1991, February 2014, and July 2014 were the driest months for the 3-, 12-, and 24-month indices, respectively (*Table 4*). For Samsun, August 2001, October 1981, and June 1982 were found to be the driest months according to the results of the 3-, 12-, and 24-month indices, respectively (*Table 5*). For Tokat, the driest month was September 1994 according to the 3-month indices, June 1974 for the 12-month indices, and October 1974 for 24-months indices (*Table 6*). The driest dates indicated by different drought indices in selected time periods for each station were parallel.

As seen in *Tables 3–6*, as the time periods examined in the indices increased, the duration of droughts increased. Also, among all indices, SPI results yielded the longest droughts in all time periods. The longest dry periods were 8 months, 9 months, 7 months, and 5 months, respectively, according to the SPI-3 results for Amasya, Corum, Samsun, and Tokat; 20 months, 15 months, 27 months, and 24 months for SPI-12; and 24 months, 28 months, 40 months, and 55 months for SPI-24.

It was seen that SPI determined drought earlier than other indices used. This was evident in Samsun and Tokat for the 12-month index values and at all stations for the 24-month index values. It was seen that the fact that the SPI determined the drought earlier was a remarkable feature of the index.

The correlation matrix and scatter diagrams of the stations were also prepared to examine the agreement between the better indices. The correlation (R) matrix is given in *Tables 7–9*, and the scatter diagrams are given in *Figs. 6–9*.

Table 7. Correlation matrix of drought indices (3 months scale)

Station	Indices	ZSI-3	CZI-3	MCZI-3
Amasya	SPI-3	0.9652	0.9766	0.9766
Corum		0.9635	0.9892	0.9889
Samsun		0.9764	0.9989	0.9985
Tokat		0.9585	0.9721	0.9721

Table 8. Correlation matrix of drought indices (12 months scale)

Station	Indices	ZSI-12	CZI-12	MCZI-12
Amasya	SPI-12	0.9935	0.9990	0.9990
Corum		0.9937	0.9931	0.9931
Samsun		0.9957	0.9983	0.9983
Tokat		0.9957	0.9935	0.9935

Table 9. Correlation matrix of drought indices (24 months scale)

Station	Indices	ZSI-24	CZI-24	MCZI-24
Amasya	SPI-24	0.9951	0.9914	0.9933
Corum		0.9977	0.9997	0.9997
Samsun		0.9972	0.9997	0.9997
Tokat		0.9961	0.9950	0.9950

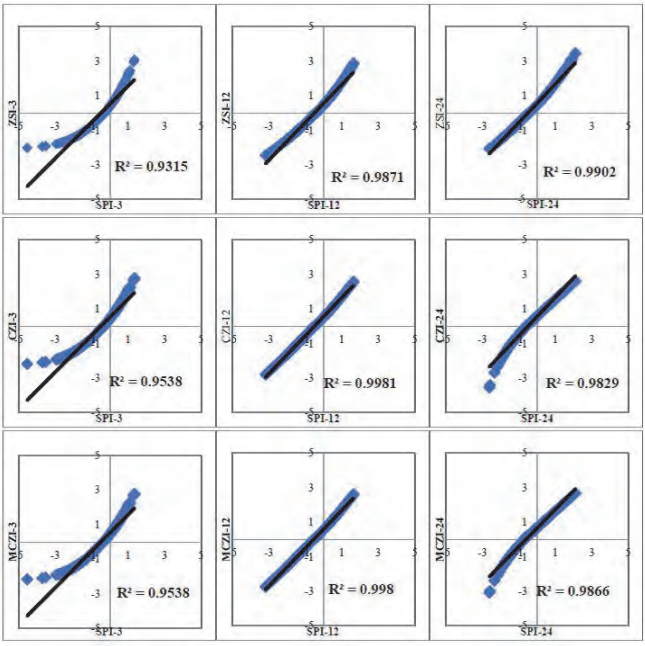

Fig. 6. Scatter diagram of Amasya station.

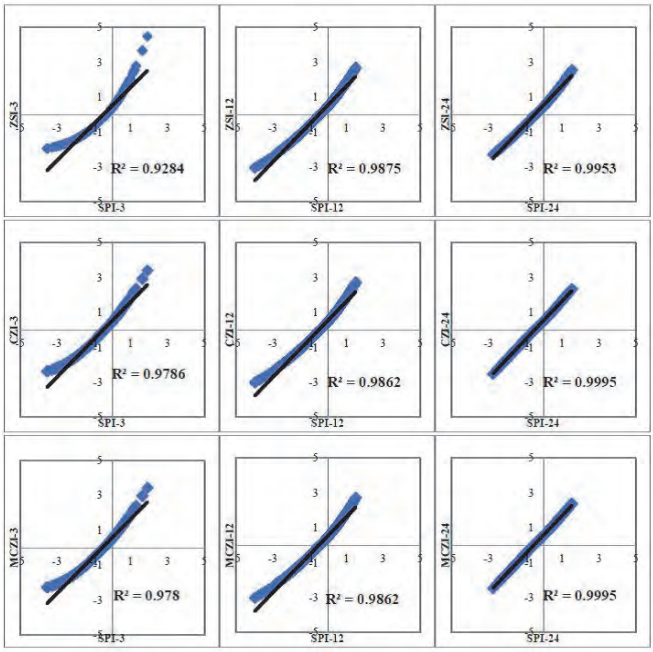

Fig. 7. Scatter diagram of Corum station.

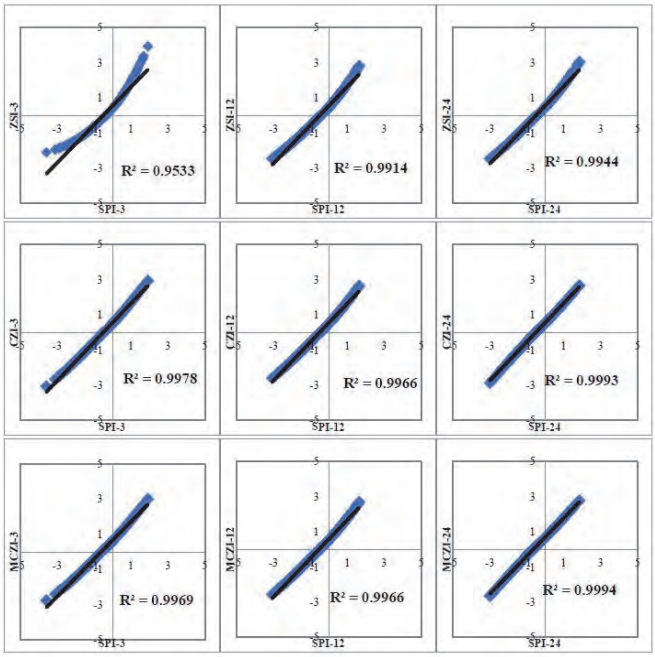

Fig. 8. Scatter diagram of Samsun station.

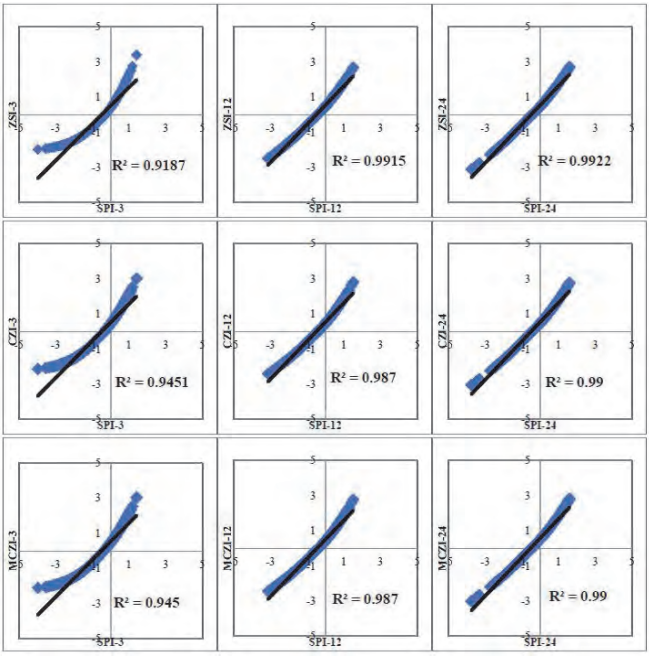

Fig. 9. Scatter diagram of Tokat station.

It was seen that the correlation values in *Tables 7–9* ranged from 0.9585-0.9997, and the indices in scatter diagrams of the stations in *Figs. 6–9* were in very good agreement with each other. The highest correlation value was found in Samsun (0.9989) between SPI-CZI for the 3-month index values, and SPI-CZI and the SPI-MCZI pairs for the 12- and 24-month index values. For the 12-month results, the correlation value of the indices for Amasya reached 0.9990; and the 24-month index values reached the highest correlation value of 0.9997 for the specified index pairs for Corum and Samsun. When the duration of the indices increased, it was found that the correlation values also increased, and the indices were more compatible with each other.

5. Conclusion

In the present study, drought analysis was made for the Yesilirmak Basin, which is one of the basins of Turkey with water potential and drought risk. The data for 4 meteorological stations selected from the basin between 1970 and 2014 were obtained from the Turkish State Meteorological Service. Four different meteorological drought indices (ZSI, CZI, MCZI, and SPI), which required precipitation data were calculated in three time scales (3-month, 12-month, and

24-month); and drought quantities (intensity, duration) were examined. Also, the relation of the indices with SPI, which was selected as the reference index, was investigated and evaluated.

As seen in time series tables and scatter diagrams, high correlation values were obtained between SPI and ZSI, and CZI and MCZI with graphs compatible with each other; and as the time intervals increased, the duration of droughts also increased in all indices. Droughts with similar intensities were detected at the same time periods for the stations included in the study. The dates of the most severe droughts were determined by four droughts indices to have a different but single date for each station and each period. Although all four indices showed similar time periods as dry periods, it was found that SPI indicated dry periods earlier than ZSI, CZI, and MCZI; and these periods lasted longer. In this way, it was concluded that SPI detected droughts earlier. These three indices, which were applied successfully to determine droughts in the Yesilirmak Basin, are recommended to be applied in detailed drought analyses that will be made in the basin as an alternative to SPI.

Drought analyses are very important for relevant ministries in basin action plans prepared separately for each basin by public institutions such as General Directorate of State Hydraulic Works (DSI) and local governments. Drought analysis will be made more realistically to show future water potentials in terms of sustainable integrated basin management.

Acknowledgements: The authors thank the reviewers for their constructive criticisms which have considerably improved this manuscript.

References

Abramowitz, M. and *Stegun, I.A.*, 1965: Handbook of Mathematical Formulas, Graphs and Mathematical Tables. Dover Publications Inc, New York.

Bacanli, U.G. and *Kargi, P.G.*, 2019: Drought analysis in long and short term periods: Bursa case. *J. Nat. Hazards Environ. 5*, 166–174. https://doi.org/10.21324/dacd.429391

Bacanli, U.G., 2017: Trend analysis of precipitation and drought in the Aegean region, Turkey. *Meteorol. Appl. 24*, 239–249. https://doi.org/10.1002/met.1622

Bacanli, U.G., Firat, M., and *Dikbas, F.*, 2009: Adaptive Neuro-Fuzzy Inference System for drought forecasting. *Stoch. Environ. Res. Risk Assess. 23*, 1143–1154. https://doi.org/10.1007/s00477-008-0288-5

Bushra, N., Rohli, R.V., Lam, N.S.N., Zou, L.L., Mostafiz, R.B., and *Mihunov, V.*, 2019: The relationship between the Normalized Difference Vegetation Index and drought indices in the South Central United States. *Nat. Hazards 96*, 791–808. https://doi.org/10.1007/s11069-019-03569-5

Deo, R.C. and *Sahin, M.*, 2015: Application of the extreme learning machine algorithm for the prediction of monthly Effective Drought Index in eastern Australia. *Atmos. Res. 153*, 512–525. https://doi.org/10.1016/j.atmosres.2014.10.016

Dikici, M. and *Aksel, M.*, 2021: Comparison of drought indices in the case of the Ceyhan Basin. *Int. J. Environ. Geoinform. 8(2)*, 113–125. https://doi.org/10.30897/ijegeo.792379

Dogan, S., Berktay, A., and *Singh, V.P.*, 2012: Comparison of multi-monthly rainfall-based drought severity indices, with application to semi-arid Konya closed basin, Turkey. *J. Hydrol.* 470–471, 255–268. https://doi.org/10.1016/j.jhydrol.2012.09.003

Downer, R.N., Siddiqui, M.M., and *Yevjevich, V.,* 1967: Applications of runs to hydrologic droughts, Int. Hydrology Symp., Colorado State University, Fort Collins, CO, 496–505.

Garcia-Leon, D., Contreras, S., and *Hunink, J.,* 2019: Comparison of meteorological and satellite-based drought indices as yield predictors of Spanish cereals. *Agricult. Water Manage. 213*, 388–396. https://doi.org/10.1016/j.agwat.2018.10.030

Gumus, V. and *Algin, H.M.,* 2017: Meteorological and hydrological drought analysis of the Seyhan−Ceyhan River Basins, Turkey. *Meteorol. Appl. 24*, 62–73. https://doi.org/10.1002/met.1605

Hejazizadeh, Z. and *Javizadeh, S.*, 2011: Introduction to Drought and Its Indices. Samt Publications, Iran.

Ionita, M., Scholz, P., and *Chelcea, S.*, 2016: Assessment of droughts in Romania using the Standardized Precipitation Index. *Nat. Hazards 81*, 1483–1498. https://doi.org/10.1007/s11069-015-2141-8

Jain, V.K., Pandey, R.P., Jain, M.K., and *Byun, H.R.*, 2015: Comparison of drought indices for appraisal of drought characteristics in the Ken River Basin. *Weather Climate Extr. 8*, 1–11. https://doi.org/10.1016/j.wace.2015.05.002

Katipoglu, O.M., Acar, R., and *Sengul, S.*, 2020: Comparison of meteorological indices for drought monitoring and evaluating: a case study from Euphrates basin, Turkey. *J. Water Climate Change 11*(S1), 29–43. https://doi.org/10.2166/wcc.2020.171

Kumanlioglu, A.A., 2020: Characterizing meteorological and hydrological droughts: A case study of the Gediz River Basin, Turkey. *Meteorol. Appl. 27*, 1–17. https://doi.org/10.1002/met.1857

Kutiel, H., Maheras, P., and *Guika, S.*, 1996: Circulation and extreme rainfall condition in The Eastern Mediterranean during the last century. *Int. J. Climatol. 16*, 73–92. https://doi.org/10.1002/(SICI)1097-0088(199601)16:1<73::AID-JOC997>3.0.CO;2-G

Lloyd-Hughes, B. and *Saunders, M.A.*, 2002: A drought climatology for Europe. *Int. J. Climatol. 22*, 1571–1592. https://doi.org/10.1002/joc.846

McKee, T.B., Doesken, N.J., and *Kleist, J.,* 1993: The relationship of drought frequency and duration to time scales. 8th Conference on Applied Climatology, Anaheim, CA, USA, January, 179–184.

McKee, T.B., Doesken, N.J., and *Kleist, J.,* 1995: Drought monitoring with multiple time scales. 9th Conference on Applied Climatology, Dallas, Texas, USA, January, 233–236.

Mishra, A.K. and *Singh, V.P.*, 2010: A review of drought concepts. *J. Hydrology 391*, 202–216. https://doi.org/10.1016/j.jhydrol.2010.07.012

Mishra, A.K. and *Singh, V.P.*, 2011: Drought modeling - A review. *J. Hydrology 403*, 157–175. https://doi.org/10.1016/j.jhydrol.2011.03.049

Morid, S., Smakhtin, V., and *Moghaddasi, M.*, 2006: Comparison of seven meteorological indices for drought monitoring in Iran. *Int. J. Climatol. 26*, 971–985. https://doi.org/10.1002/joc.1264

Myronidis, D., Fotakis, D., Ioannou, K., and *Sgouropoulou, K.*, 2018: Comparison of ten notable meteorological drought indices on tracking the effect of drought on streamflow. *Hydrol. Sci. J. 63*, 2005–2019. https://doi.org/10.1080/02626667.2018.1554285

Nedham, U.S. and *Hassan, A.S.*, 2019: Comparison of some drought indices in Iraq. *Al-Mustansiriyah J. Sci. 30*(4), 1–9. http://doi.org/10.23851/mjs.v30.i4.674

Oguzturk, G. and *Yildiz, O.*, 2014: Drought analysis for different time periods in the city of Kirikkale. *Int. J. Engin. Res. Develop. 6*(2), 19–25. https://doi.org/10.29137/umagd.346084

Oguzturk, G. and *Yildiz, O.*, 2015: Hydrologic drought investigation in The Kemer Dam basin using the Spi Method. *Int. J. Adv. Mech. Civil Engin. 2*(5), 35–40.

Oguzturk, G. and *Yildiz, O.*, 2016: Assessing hydrological responses to droughts in the Hirfanli Dam basin, Turkey. *Int. J. Adv. Mech. Civil Engin 3*(5), 116–123.

Osuch, M., Romanowicz, R.J., Lawrence, D., and Wong, W.K., 2016: Trends in projections of standardized precipitation indices in a future climate in Poland. Hydrology and Earth System Sciences 20, 1947–1969. https://doi.org/10.5194/hess-20-1947-2016

Pathak, A. and *Dodamani, B.M.*, 2019: Comparison of meteorological drought indices for different climatic regions of an Indian River Basin. *Asia-Pacific J. Atmos. Sci*. 56, 563–576. https://doi.org/10.1007/s13143-019-00162-5

Payab, H. and *Turker, U.*, 2019: Comparison of standardized meteorological indices for drought monitoring at northern part of Cyprus. *Environ. Earth Sci. 78*(10), 309–327. https://doi.org/10.1007/s12665-019-8309-x

Ramkar, P. and *Yadav, S.M.*, 2018: Spatiotemporal drought assessment of a semi-arid part of middle Tapi River Basin, India. *Int. J. Disaster Risk Reduct. 28*, 414–426. https://doi.org/10.1016/j.ijdrr.2018.03.025

Sirdas, S. and *Sen, Z.*, 2003: Spatio-temporal drought analysis in the Trakya Region, Turkey. *Hydrol. Sci. J. 48*, 809–820. https://doi.org/10.1623/hysj.48.5.809.51458

Soleimani, H., Ahmadi, H., and *Zehtabian, G.*, 2013: Comparison of temporal and spatial trend of SPI, DI and CZI as important drought indices to map using IDW method in Taleghan Watershed. *Ann. Biol. Res. 4*(6), 46–55.

Sridhara, S., Chaithra, G.M., and *Gopakkali, P.,* 2021: Assessment and monitoring of drought in Chitradurga district of Karnataka using different drought indices. *J. Agrometeorol. 23*, 221–227. https://doi.org/10.54386/jam.v23i2.72

TUBITAK, 2010: The Scientific and Technological Research Council of Turkey: Havza Koruma Eylem Planlarının Hazırlanması-Yesilirmak Havzası. (in Turkish)

Thom, H.C.S., 1958: A Note on the gamma distribution. *Mon. Weather Rev. 86*(4), 117–122. https://doi.org/10.1175/1520-0493(1958)086<0117:ANOTGD>2.0.CO;2

Wang, F.Q., Zheng, Z., Kang, P.P., and *Wang, L.*, 2017: Applicability evaluation on the indexes of typical drought in Henan province, China. *Appl. Ecol. Environ. Res. 15(3), 253–262.* http://dx.doi.org/10.15666/aeer/1503_253262

Vergni, L., Todisco, F., and *Di Lena, B.*, 2021: Evaluation of the similarity between drought indices by correlation analysis and Cohen's Kappa test in a Mediterranean area. *Nat. Hazards 108*(2), 2187–2209. https://doi.org/10.1007/s11069-021-04775-w

Wu, H., Hayes, M.J., Weiss, A., and *Hu, Q.*, 2001: An evaluation of the Standardized Precipitation Index, the China-Z Index and the statistical Z-Score. *Int. J. Climatol. 21*, 745–758. https://doi.org/10.1002/joc.658

Yacoub, E. and *Tayfur, G.,* 2017: Evaluation and assessment of meteorological drought by different methods in Trarza Region, Mauritania. *Water Res. Manage. 31*, 825–845. https://doi.org/10.1007/s11269-016-1510-8

Yacoub, E. and *Tayfur, G.*, 2020: Spatial and temporal of variation of meteorological drought and precipitation trend analysis over whole Mauritania. *J. African Earth Sci. 163*, 1–12. https://doi.org/10.1016/j.jafrearsci.2020.103761

Yenigun, K. and *Ibrahim, W.A.*, 2019: Investigation of drought in the northern Iraq region. *Meteorol. Appl. 26,* 490–499. https://doi.org/10.1002/met.1778

Yildiz, O., 2009: Assessing temporal and spatial characteristics of droughts in the Hirfanli Dam basin, Turkey. *Sci. Res. Essays 4*(4), 249–255. https://doi.org/10.5897/SRE.9000212

Yue, Q., Dawen, Y., Huimin, L., Kai, X., and *Xiangyu, X.,* 2015: Comparative analysis of drought based on precipitation and soil moisture indices in Haihe Basin of North China during the period of 1960–2010. *J. Hydrol. 526*, 55–67. https://doi.org/10.1016/j.jhydrol.2014.09.068

Zarei, A., Asadi, E., Ebrahimi, A., Jafary, M.M., Malekian, A., Tahmoures, M., and *Alizadeh, E.E.*, 2017: Comparison of meteorological indices for spatio-tem-poral analysis of drought in Chahrmahal-Bakhtiyari province in Iran. *Hrvatski Meteorološki Časopis 52*(52), 13–26.

INSTRUCTIONS TO AUTHORS OF *IDŐJÁRÁS*

The purpose of the journal is to publish papers in any field of meteorology and atmosphere related scientific areas. These may be

- research papers on new results of scientific investigations,
- critical review articles summarizing the current state of art of a certain topic,
- short contributions dealing with a particular question.

Some issues contain "News" and "Book review", therefore, such contributions are also welcome. The papers must be in American English and should be checked by a native speaker if necessary.

Authors are requested to send their manuscripts to

Editor-in Chief of IDŐJÁRÁS
P.O. Box 38, H-1525 Budapest, Hungary
E-mail: journal.idojaras@met.hu

including all illustrations. MS Word format is preferred in electronic submission. Papers will then be reviewed normally by two independent referees, who remain unidentified for the author(s). The Editor-in-Chief will inform the author(s) whether or not the paper is acceptable for publication, and what modifications, if any, are necessary.

Please, follow the order given below when typing manuscripts.

Title page should consist of the title, the name(s) of the author(s), their affiliation(s) including full postal and e-mail address(es). In case of more than one author, the corresponding author must be identified.

Abstract: should contain the purpose, the applied data and methods as well as the basic conclusion(s) of the paper.

Key-words: must be included (from 5 to 10) to help to classify the topic.

Text: has to be typed in single spacing on an A4 size paper using 14 pt Times New Roman font if possible. Use of S.I. units are expected, and the use of negative exponent is preferred to fractional sign. Mathematical formulae are expected to be as simple as possible and numbered in parentheses at the right margin.

All publications cited in the text should be presented in the *list of references*, arranged in alphabetical order. For an article: name(s) of author(s) in Italics, year, title of article, name of journal, volume, number (the latter two in Italics) and pages. E.g., *Nathan, K.K.,* 1986: A note on the relationship between photosynthetically active radiation and cloud amount. *Időjárás 90,* 10–13. For a book: name(s) of author(s), year, title of the book (all in Italics except the year), publisher and place of publication. E.g., *Junge, C.E.,* 1963: *Air Chemistry and Radioactivity.* Academic Press, New York and London. Reference in the text should contain the name(s) of the author(s) in Italics and year of publication. E.g., in the case of one author: *Miller* (1989); in the case of two authors: *Gamov* and *Cleveland* (1973); and if there are more than two authors: *Smith et al.* (1990). If the name of the author cannot be fitted into the text: *(Miller,* 1989); etc. When referring papers published in the same year by the same author, letters a, b, c, etc. should follow the year of publication. DOI numbers of references should be provided if applicable.

Tables should be marked by Arabic numbers and printed in separate sheets with their numbers and legends given below them. Avoid too lengthy or complicated tables, or tables duplicating results given in other form in the manuscript (e.g., graphs). *Figures* should also be marked with Arabic numbers and printed in black and white or color (under special arrangement) in separate sheets with their numbers and captions given below them. JPG, TIF, GIF, BMP or PNG formats should be used for electronic artwork submission.

More information for authors is available: journal.idojaras@met.hu

Published by the Hungarian Meteorological Service

Budapest, Hungary

ISSN 0324-6329 (Print)

ISSN 2677-187X (Online)